Doctor of Philosophy
Doctoral thesis in Electrical Engineering

DTU Space
Electromagnetic Systems Group

Fast Full-Wave Methods for Aperiodic Antenna Arrays for Space Applications

Magnus Brandt-Møller

Kongens Lyngby, 2024

DTU

Supervisors: Assoc. Prof. Michael Mattes (University) & Dr. Min Zhou (Company)
Co-supervisors: Dr. Olav Breinbjerg & Dr. Erik Jørgensen

DTU Space – National Space Institute
Division of Electromagnetic Systems
Technical University of Denmark
Ørsteds Plads
Building 348, 2nd floor
2800 Kongens Lyngby, Denmark

"To Valder, the light of my days, so dear,
in each challenge, you quelled my fear.
Your laughter, a beacon through night and day,
in your smile, my worries melt away.

To Julie, with a love so pure and true,
your unwavering support saw me through.
In every step, every hurdle we've crossed,
without you, my path would be lost."
*— **Magnus Brandt-Møller***

This page is intentionally not used for content

Abstract

English

This dissertation presents the Higher-Order Array Decomposition Method (HO-ADM), a fast, accurate yet versatile full-wave analysis technique applicable for electrically large arrays of antennas or scatterers, as they are typical for space applications, including sparse, connected, and non-identical-element arrays. The HO-ADM exploits the multi-level block-Toeplitz (MBT) property of the Method of Moments (MoM) matrix in case of regular arrays, permitting an FFT-accelerated matrix-vector product (MVP) to achieve asymptotic computational and memory complexities of $\mathcal{O}(N \log N)$ and $\mathcal{O}(N)$, respectively, where N is the number of unknowns.

The combination of ADM with higher-order (HO) hierarchical Legendre basis functions (BFs) generally yields an order of magnitude reduction in both computation time and memory consumption as compared to using first-order BFs. For example, a 40 times reduction in total computation time and a ten times reduction in memory consumption is achieved for a 100-element Direct Radiating Array (DRA) of conical horns on a laptop, resulting in a computation time of five minutes compared to over three hours with first-order BFs.

Several extensions of the HO-ADM are presented including capabilities for analyzing sparse array antennas, arrays with electric conduction currents between elements, arrays with non-identical elements, and arrays with dielectric substrates. The analysis of sparse array antennas is achieved by using a technique to implicitly keep the MoM matrix for a fully populated array, thus preserving the FFT-accelerated MVP, and by employing a constrained Krylov subspace in the iterative solver.

The extension to arrays with electric conduction currents between elements is accomplished by introducing half-doublet BFs at connected boundaries, using the Discontinuous Galerkin Method (DGM) to enforce current continuity, and by introducing auxiliary unknowns to retain the MBT property of the MoM matrix. The analysis of arrays with non-identical elements is realized by introducing the concept of a Super Unit Cell (SUC) from which individual mesh-regions can be excluded from the iterative solution process.

Finally, the analysis of connected and simultaneously closed structures, including dielectric substrates, is made possible by introducing a method of internal walls and internal equivalent currents, and by employing the Poggio-Miller-Chang-Harrington-Wu-Tsai (PMCHWT) integral equation formulation.

Numerous numerical tests have confirmed the efficacy and accuracy of the presented extensions, from which it is evident that the HO-ADM, generally, is more than an order of magnitude faster than a state-of-the-art Higher-Order Multi-level Fast Multipole Method (HO-MLFMM) implementation. This performance is achieved with a memory consumption of HO-ADM which is reduced or comparable to HO-MLFMM. For example, a $32 \times 32 = 1024$-element connected all-metal antenna array designed for the Europa Lander mission is analyzed on a laptop within six minutes with one million unknowns with HO-ADM, compared to approximately one hour for HO-MLFMM. Another example is a $8 \times 128 = 1024$-element patch array with non-identical elements which is solved with HO-ADM in three minutes compared to half an hour for HO-MLFMM. Additionally, results demonstrate efficient and accurate analysis of a $20 \times 20 = 400$-element array of PEC cylinders embedded in a dielectric substrate. Moreover, a finite thickness PEC plate with 2500 holes, analyzed as a 50×50-element array of identical elements with the HO-ADM is solved with a total computation time of four minutes, compared to 68 minutes with HO-MLFMM.

The developed method represents a significant advancement in the field of computational electromagnetics applied to the simulation of electrically large arrays of antennas or scatterers. Through a rigorous application of an FFT-accelerated MVP, the computation times compared to an existing fast method based on the MLFMM are reduced by at least a factor of ten, while at the same time maintaining a comparable memory consumption or even less. The tremendous acceleration in computation speed makes the design and optimization of state-of-the-art antenna arrays more efficient and reduces significantly the time to market.

Danish

Denne afhandling præsenterer den såkaldte Higher-Order Array Decomposition Metode (HO-ADM), en hurtig, præcis og samtidigt alsidig fuldbølgeanalyseteknik, der kan anvendes til elektrisk store grupper af antenner eller spredere, hvilke typisk anvendes indenfor applikationer til brug i rummet, herunder antennegrupper der er sparsomt besatte, antennegrupper med elektrisk forbundne elementer samt grupper bestående af uens elementer. HO-ADM udnytter multi-niveau block-Toeplitz (MBT) egenskaben for momentmetode (MoM)-matricen i tilfælde af regulære antennegrupper, hvilket muliggør et FFT-accelereret matrix-vektor produkt (MVP) for at opnå asymptotiske beregnings- og hukommelseskompleksiteter på henholdsvis $\mathcal{O}(N \log N)$ og $\mathcal{O}(N)$, hvor N er antallet af ubekendte.

Kombinationen af ADM med højere-ordens (HO) hierarkiske Legendre basisfunktioner (BF'er) medfører generelt en tifold reduktion i både beregningstid og hukommelsesforbrug sammenlignet med brugen af første-ordens basisfunktioner. For eksempel opnås en 40 ganges reduktion i samlet beregningstid og en tifold reduktion i hukommelsesforbrug for en 100-elementers antennegruppe af koniske horn, vel at

mærke på en bærbar computer med en samlet beregningstid på fem minutter, i modsætning til over tre timer med første-ordens BF'er.

Der præsenteres adskillige udvidelser af HO-ADM, herunder muligheden for at analysere sparsomt besatte antennegrupper, grupper med elektriske ledningsstrømme mellem elementerne, grupper bestående af uens elementer samt grupper med dielektriske substrater. Analysen af sparsomt besatte antennegrupper er opnået ved at benytte en teknik til implicit at bevare MoM-matricen for en fuldt besat gruppe, og således bevare det FFT-accelererede MVP, samt ved at benytte et begrænset Krylov-underrum i den iterative løsningsproces.

Udvidelsen til grupper med elektriske ledningsstrømme mellem elementer er opnået ved at introducere halve BF'er ved elementernes forbundne grænser, ved at benytte den såkaldte Discontinuous Galerkin Method (DGM) til at sikre strømkontinuitet, samt ved at introducere hjælpe-ubekendte for at bevare MBT-egenskaben af MoM-matricen. Analysen af grupper med uens elementer er realiseret ved at introducere den såkaldte Super Unit Cell (SUC), hvorfra individuelle diskretiseringsregioner kan ekskluderes fra den iterative løsningsproces. Yderligere er analysen af forbundne og samtidigt lukkede strukturer, inklusive dielektriske substrater, gjort mulig ved at introducere en metode for interne vægge og interne ækvivalente strømme, samt ved at bruge Poggio-Miller-Chang-Harrington-Wu-Tsai (PMCHWT) integralligningsformuleringen.

Adskillige numeriske eksperimenter har bekræftet effektiviteten og nøjagtigheden af de præsenterede udvidelser, hvorfra det er tydeligt, at HO-ADM generelt er mere end ti gange hurtigere end en moderne såkaldt Higher-Order Multi-level Fast Multipole Method (HO-MLFMM) implementering. Denne ydeevne opnås med et hukommelsesforbrug som er reduceret eller sammenligneligt med HO-MLFMM. For eksempel analyseres en $32 \times 32 = 1024$-elementers antennegruppe med forbundne elementer, designet til den såkaldte Europa Lander mission, på en bærbar computer inden for seks minutter med en million ubekendte, sammenlignet med cirka en time for HO-MLFMM. Et andet eksempel, er en $8 \times 128 = 1024$-elementers patch antennegruppe bestående af uens elementer, hvilket løses med HO-ADM på tre minutter sammenlignet med en halv time for HO-MLFMM. Desuden demonstrerer resultaterne effektiv og nøjagtig analyse af en $20 \times 20 = 400$-elementers gruppe af PEC-cylindre indlejret i et dielektrisk substrat. Slutteligt løses en perfekt elektrisk ledende (PEC) plade med endelig tykkelse med 2500 huller, analyseret som en 50×50-elementers gruppe af ens elementer med HO-ADM på fire minutter, sammenlignet med 68 minutter for HO-MLFMM.

Den udviklede metode repræsenterer betydelige fremskridt indenfor numerisk felteori anvendt til analysen af elektrisk store grupper af antenner eller spredere. Via et nøjagtigt FFT-accelereret MVP reduceres simuleringstiderne med mindst en faktor ti sammenlignet med en eksisterende hurtig metode baseret på MLFMM, medens der samtidigt opretholdes sammenligneligt, eller endda mindre, hukommelsesforbrug. Denne markant forøgede acceleration i simuleringshastighed gør design og optimering af moderne antennegrupper mere effektiv og reducerer signifikant tiden fra konceptudvikling til fremstilling af fremtidens antenner.

This page is intentionally not used for content

Preface

The research and findings described in the present work were conducted collaboratively at DTU Elektro, which during the project became part of DTU's National Space Institute, and TICRA over a span of three years, starting in August 2020 and culminating in December 2023. This endeavor was undertaken as part of the necessary criteria and in partial fulfillment of the Industrial Ph.D. Degree, which is conferred by the Technical University of Denmark. The study was funded by TICRA with the support of the Innovation Fund Denmark.

Kongens Lyngby, 30th April 2024

Magnus Brandt-Møller

Magnus Brandt-Møller

This page is intentionally not used for content

Acknowledgements

"Significant accomplishments are invariably dependent upon the acknowledgment that the dissemination of knowledge ought to be a communal endeavor."

In that regard, I wish to extend my profound appreciation and gratitude to an array of individuals who have been instrumental in the fruition of this work. Their invaluable support, whether scientific or emotional, has guided me through the most challenging junctures of this journey.

I am deeply indebted to my dedicated supervisors. Their belief in me provided an open gateway not just to the intricate world of advanced electromagnetics, but also to a comprehensive understanding and exposure to the multi-faceted dimensions of a research career. Their guidance, patience, and unwavering commitment to my academic growth have been pivotal in molding me into the researcher I am today.

I reserve special words of praise for my family and dear friends. Their relentless faith in my capabilities, coupled with their enduring understanding and support, has been the backbone of my perseverance. To Julie, your encouragement has been a constant source of inspiration. Your resolute solicitude, combined with the boundless love you have shown me, and our son, over the past three years, has been a pillar of strength. I am forever grateful for having you and Valder by my side, especially during this transformative phase of my life.

This page is intentionally not used for content

Abbreviations, Symbols & Operators

ADM	**A**rray **D**ecomposition **M**ethod
AP-S	**A**ntennas and **P**ropagation **S**ociety
AWPL	**A**ntennas and **W**ireless **P**ropagation **L**etters
CAD	**C**omputer **A**ided **D**esign
BF	**B**asis **F**unction
BT or **BC**	**B**lock-**T**oeplitz or **B**lock-**C**irculant
CEM	**C**omputational **E**lectro**M**agnetics
CFIE	**C**ombined **F**ield **I**ntegral **E**quation
Co-pol	The **pol**arization the antenna is intended (**co**) to radiate
Cross-pol	The **pol**arization orthogonal (**cross**) to a specified reference polarization
DDM	**D**omain **D**ecomposition **M**ethod
DGIE	**D**iscontinuous **G**alerkin **I**ntegral **E**quation
DGM	**D**iscontinuous **G**alerking **M**ethod
DRA	**D**irect **R**adiating **A**rray
DTE	**D**irect-**T**o-**E**arth
DTU	**T**echnical **U**niversity of **D**enmark
EFIE	**E**lectric **F**ield **I**ntegral **E**quation
EMS	**E**lectro**M**agnetic **S**ystems Group
ESA	**E**uropean **S**pace **A**gency
FFT	**F**ast **F**ourier **T**ransform
FSLL	**F**irst **S**ide**L**obe **L**evel
GEO	**GE**ostationary **O**rbit
GMRES	**G**eneralized **M**inimum **RES**idual Method
HO	**H**igher-**O**rder
IE	**I**ntegral **E**quation
ICEAA	**I**nternational **C**onference on **E**lectromagnetics in **A**dvanced **A**pplications
IEEE	The **I**nstitute of **E**lectrical and **E**lectronics **E**ngineers
LEO	**L**ow **E**arth **O**rbit
FEM	**F**inite **E**lement **M**ethod

MBF	**M**acro**B**asis **F**unction
MBT	**M**ulti-level **B**lock-**T**oeplitz
MEO	**M**edium **E**arth **O**rbit
MFIE	**M**agnetic **F**ield **I**ntegral **E**quation
MLFMM	**M**ulti-**L**evel **F**ast **M**ultipole **M**ethod
MoM	**M**ethod **o**f **M**oments
MVP	**M**atrix-**V**ector **P**roduct
NF	**N**ear **F**ield
OTM	**O**n-**T**he-**M**ove
PEC	**P**erfect **E**lectrical **C**onductor
PIM	**P**assive **I**nter**M**odulation
PMCHWT	**P**oggio-**M**iller-**C**hang-**H**arrington-**W**u-**T**sai
RHCP	**R**ight-**H**and **C**ircularly **P**olarized
RWG	**R**ao-**W**ilton-**G**lisson
SI	Le **S**ystème **I**nternational d'Unités (The International System of Units)
SUC	**S**uper **U**nit **C**ell
TAP	**T**ransactions on **A**ntennas and **P**ropagation

$\mathbf{A}$	The Method of Moments Matrix.	
β	Regularization parameter in the DGIE.	
$\vec{b}$	Right-hand side vector for a linear system of equations.	
$\mathbf{C}$	Circulant generator tensor.	
d	Number of dimensions in a regular array lattice.	
ε	Permittivity of a given medium.	
ε_0	Permittivity of free-space.	
$\varepsilon_{\mathrm{ERE}}$	Equivalent relative error measure.	
f	Frequency.	[Hz]
h	The maximum allowable mesh length.	[m]
h_λ	Discretization density: Total number of unknowns N normalised by the total surface area in square wavelengths.	
$\mathcal{J}_s$	Surface Jacobian determinant.	
$\vec{J}$	Surface current density vector.	
j	The imaginary unit defined as $j^2 = 1$.	
n_i	Number of elements in the i^{th} lattice dimension.	
k	General complex wave number.	[rad/m]
λ_0	Free-space wavelength.	[m]
$\mathcal{M}$	Generic block-diagonal preconditioning matrix.	
μ_0	Permeability of free-space.	
N	Total number of unknowns $N = sT$.	
N_{ext}	Total number of unknowns in a circulantly extended MBT MoM matrix $\mathbf{A}$.	
ω	Angular frequency $\omega = 2\pi f$.	

ϕ	Azimuthal angle of observation in a standard spherical coordinate system, with $\phi = 0$, in the x-y plane coinciding with the positive x-axis. [deg] or [rad]
P_n	The Legendre polynomial of degree n.
$\tilde{P}_n$	Modified Legendre polynomials of degree n.
ρ	Maximum basis function order used on a quadrilateral.
r	Radial distance from the origin in a standard spherical coordinate system. [m]
s	Total number of basis functions on a single array element.
θ	Polar angle of observation in a standard spherical coordinate system, with $\theta = 0°$ coinciding with the positive z-axis. [deg] or [rad]
T	Total number of array elements.
T_{ex}	Number of excluded/removed elements from an array of T elements.
T_{NI}	Number of distinctly different elements of a non-identical array.
$\vec{x}$	Vector of unknowns for a linear system of equations.
$\circledast$	Discrete circular convolution.
$\mathcal{C}^{\uparrow}$ or $\mathcal{C}^{\downarrow}$	Specialized copy operator for the realization of thinned array in HO-ADM.
$\mathcal{F}_d$	d-dimensional discrete Fourier transformation.
$\odot$	Hadamard multiplication operator (i.e. element-wise multiplication).
$\oslash$	Hadamard division operator (i.e. element-wise division).
$\mathcal{L}$	EFIE operator.
∇	Gradient operator.
$\nabla\cdot$	Divergence operator.
$\mathcal{P}$	Single-layer vector potential.
$\mathcal{Q}$	Single-layer scalar potential.
$\mathcal{Z}_{a,b}(\vec{x})$	Zeroing operator placing zeros at those positions in the vector $\vec{x}$ which pertains to array elements at the position (a, b).

This page is intentionally not used for content

Contents

This page is intentionally not used for content

List of publications

The following publications have been prepared and published during the project period and are listed in chronological order for journal and conference contributions, respectively. A concise summary is provided beneath each publication along with its current status. The author of this dissertation has written and is the main author of the journal papers [J1, J2] and conference papers [C1-C3] which are included after the conclusions under Publications on pages 65 – 93.

Journal Publications

J1 M. Brandt-Møller, M. Mattes, O. Breinbjerg, M. Zhou, and O. Borries, "Array Decomposition Method for Arbitrary-Element Regular Arrays Using Higher-Order Basis Functions," IEEE Antennas Wireless Propag. Lett. (AWPL), vol. 22, no. 1, pp. 24–28, 2022.

The boundary integral part of the Array Decomposition Method is combined with hierarchical higher-order basis functions and presented in an implementation-friendly matrix-algebraic form. Higher-order polynomial convergence is demonstrated on an array of spheres and results show that substantial memory savings and considerable computational speed-ups are possible by this combination while, at the same time, maintaining, or even improving, the accuracy.

Status: Published

J2 M. Brandt-Møller, M. Mattes, O. Breinbjerg, M. Zhou, and E. Jørgensen, "Extended Higher-Order Array Decomposition Method for Fully Populated or Thinned Array Antennas and Scatterers with Connected Elements," IEEE Trans. Antennas Propag. (TAP), to be published, 2023.

The HO-ADM is extended to handle sparse/thinned arrays as well as conduction currents between array elements. The Discontinuous Galerkin Method, together with appropriately chosen auxiliary unknowns, is used to retain the multi-level block-Toeplitz Method of Moment matrix retaining an FFT-accelerated method. An effective yet necessary constant-memory coupling preconditioner applicable for connected and thinned arrays is presented.

Status: Published 27/03-2024

Conference Publications

C1 M. Brandt-Møller, M. Mattes, O. Breinbjerg, M. Zhou, and O. Borries, "Performance of Array Decomposition Method with Higher-Order Basis Functions," in *2022 IEEE International Symposium on Antennas and Propagation and USNC-URSI Radio Science Meeting* (*AP-S/URSI*), pp. 1830-1831, July 2022.

We evaluate the performance of the Array Decomposition Method combined with higher-order basis functions compared to using traditional first-order basis functions. The results show that using higher-order basis functions instead of traditional first-order basis functions, memory and computation time savings in the order of 9 and 44 times, respectively, can be achieved for a conical horn array.

Status: Published

C2 M. Brandt-Møller, M. Mattes, O. Breinbjerg, M. Zhou, and E. Jørgensen, "Higher-Order Array Decomposition Method for Array Antennas with Connected Elements," in *2023 IEEE International Symposium on Antennas and Propagation and USNC-URSI Radio Science Meeting* (*AP-S/URSI*), pp. 585-586, July 2023.

The extended Higher-Order Array Decomposition Method capable of analyzing connected antenna arrays is applied to a 8×8 sub-array designed for the Europa Lander mission. The results show a substantial computational speed-up by a factor of 35 compared to a state-of-the-art higher-order implementation of MLFMM.

Status: Published

C3 M. Brandt-Møller, M. Mattes, O. Breinbjerg, M. Zhou, and E. Jørgensen, "Extension of the Higher-Order Array Decomposition Method for Arrays with Non-identical Elements," in *2023 International Conference on Electromagnetics in Advanced Applications* (*ICEAA*), pp. 277-279, July 2023.

The Higher-Order Array Decomposition Method is extended to arrays with non-identical elements. The extension is made possible by an appropriate manipulation of the FFT-accelerated matrix-vector product, special super-unit-cell meshing, and by excluding a selected subset of unknowns from the Krylov subspace in the iterative solution process. Results show that the computation time for a non-identical 1024-element patch array can be reduced by an order of magnitude by employing HO-ADM compared to a state-of-the-art higher-order MLFMM implementation.

Status: Published

CHAPTER 1

Introduction

Since the launch of the world's first satellite (Sputnik 1) in 1957, profound scientific developments have facilitated the realization of near real-time global television broadcasts and phone calls, deep-space exploration as well as remote-sensing of our earth. Such developments have necessitated increased capabilities and physical complexity of antennas for space applications. Traditionally, reflector antennas have been the predominant choice for both satellite-based communication, deep-space exploration, and earth observation missions as they provide the highest gain and impedance bandwidth while maintaining excellent ground coverage at the lowest cost [1]. Nevertheless, an on-going shift from large spacecrafts in geo-stationary orbit to constellations of smaller spacecrafts in low-earth-orbit (LEO) or medium-earth-orbit (MEO) and a huge demand for flexible in-orbit antenna reconfiguration is identified as two major trends which will change the antenna technology used in future satellite payloads [2].

The demand for in-orbit flexibility and the shift towards MEO and LEO spacecrafts drive the development of payloads which incorporate direct radiating antenna arrays with electronic steering and beam-shaping capabilities [3, 4]. Thus far, the adaptation of array technology for space applications has been impeded by a variety of factors. One of the central impediments of existing array-based payloads is the limited number of beams which can be produced [5]. Where state-of-the-art reflector-based telecom payloads produce thousands of simultaneous beams [6, 7], state-of-the-art array-based payloads (Eutelsat Quantum) only produce 8 [8]. In addition, next-generation ground terminals must be able to concurrently track numerous LEO satellites, which is not possible with existing reflector-based technology [4, 9]. Consequently, a gradual change from reflector-based technology to active array antennas is highly anticipated for future deployed space payloads [10].

For this transition, future array-based payloads need to produce a considerably greater amount of beams, requiring the synthesis of electrically large antenna arrays. Their performance is nevertheless contingent upon the ability to accurately predict antenna array performance through rigorous methods based on computational electromagnetics (CEM). Existing methods used to synthesize large arrays are based on the embedded element pattern method [11], where a single array element is analyzed assuming identical neighbors in a regular grid. These methods are inaccurate close to the array edges and electromagnetic mutual coupling between array elements is generally considered a parasitic effect [12]. This increases the possibility of favoring

one type of array element over another merely because mutual coupling is disregarded. Moreover, arrays for space applications are expected to be implemented as sparse or aperiodic arrays [13, 14], in which the existing embedded element pattern approach can no longer be employed. Consequently, mutual coupling is neglected already during the design phase, which implies that subsequent physical implementation must evade mutual coupling effects, e.g. by larger element spacings and/or added shielding structures, which in turn leads to added mass and volume.

If a more accurate analysis approach existed one could instead regard mutual coupling as an inherent property of the array, which can be exploited instead of being avoided. This would permit accurate designs of dense aperiodic antenna arrays, in which array elements can be placed closer and can be cast in any shape, providing both mass, volume and monetary savings while maintaining excellent antenna performance. Presently available algorithms for analyzing aperiodic antennas are, however, too limited to support the rapid development of new space-technology (see Section 1.3), either because they require a tremendous amount of computer resources or because they employ approximations that are not error-controllable[†] and typically assume insignificant electromagnetic coupling between array elements.

1.1 Research Objective

To address the above-mentioned challenges, the objective of this dissertation is to develop a **fast**, **accurate** yet **versatile** analysis method for aperiodic antenna arrays for space applications. Please note that in this work, we generally adopt and adhere to the IEEE definition [15] of terms for antennas. As an example, the term "aperiodic array" is understood as "an array with non-uniformly spaced elements" which include sparse, thinned and space-tapered arrays.

By the term **fast**, we mean that the asymptotic computational complexity shall be, at least, better than that of the conventional Method of Moments $\mathcal{O}(N^3)$, but preferably of the order of $\mathcal{O}(N \log N)$, in which N is the total number of unknowns. Moreover, the total computation time of the new analysis method should be faster than existing state-of-the-art methods when run on comparable hardware.

By the term **accurate**, we mean that the method should not resort to any approximations other than those inherent to the discretization of the problem (meshing), representation of the fields and currents as a finite linear combination of basis functions (BFs) and the iterative solution procedure. In case approximations are unavoidable, it is paramount that they are error-controllable in the sense that one can specify the desired accuracy a priori to a simulation run.

By the term **versatile**, we mean that the method is capable of analyzing general arrays comprising both planar and volumetric array elements. It should efficiently

[†]An error-controllable method is in this dissertation understood as a method for which the user can specify a priori to a simulation run, the number of significant digits which is desired in the solution vector.

handle sparse or thinned arrays and accommodate interconnecting geometry that permit conduction currents to flow between elements. Non-identical elements and dielectric substrates should be handled as well.

Beyond speed and accuracy, the method's versatility is what truly makes it effective in real-world applications. As depicted in Figure 1.1, this versatility is presented as the four main requirements for the developed method.

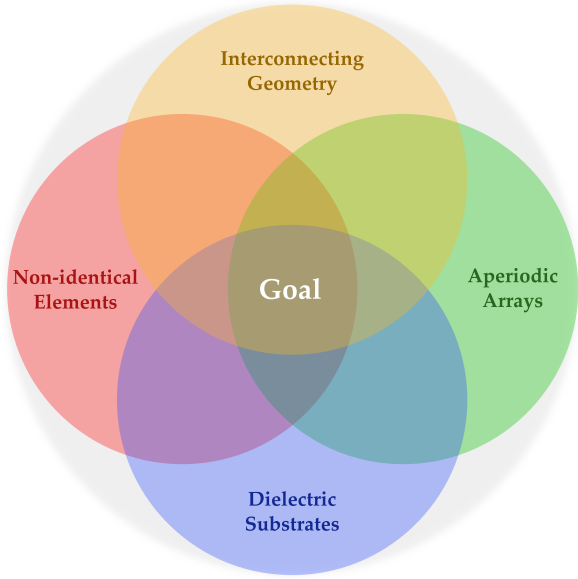

Figure 1.1: Versatility requirements for the developed computational method, showing the overlapping regions of applicability.

1.2 Framework of the Dissertation

It is important to highlight that the findings presented in this dissertation are built upon the extensive groundwork laid by colleagues at TICRA prior to the start of the PhD study. The developed method, therefore, is an extension of the already advanced capabilities of TICRA's established software package, ESTEAM [16]. More specifically, the code developed in this PhD study relies on the following already existing components:

- A Higher-Order Method of Moments (HO-MoM) implementation [17], encompassing scatterer geometrical discretization and meshing, basis function creation, and surface integration routines for the Electric (EFIE) and Magnetic (MFIE) Field Integral operators [18].
- A preconditioned Generalized Minimum RESidual (GMRES) implementation.

As a result, both the developed method and the ensuing discussion on state-of-the-art techniques have been limited to surface integral equation (IE)-based methods utilizing an iterative solution approach. Note also, that some parts pertaining to the existing code cannot be disclosed.

1.3 State-of-the-Art

While the Method of Moments [19] (MoM) can be regarded as accurate in the sense that it rigorously takes into account all mutual coupling and edge effects, and versatile in handling complex structures with intricate details, it is not fast. For the conventional MoM for surface integral equations, the memory consumption and computational complexity scales as[†] $\mathcal{O}(N^2)$ and $\mathcal{O}(N^2) - \mathcal{O}(N^3)$, respectively, where N is the number of unknowns. This asymptotic scaling is prohibitively large for the design of future phased array antennas for space applications.

Traditional methods used to analyze and design electrically large arrays are primarily based on approximate methods. Herein, the predominant approach has been the embedded element (or active element) pattern method [11, 21], in which a single (or few) array elements are analyzed assuming identical neighbors in a regular grid [22]. Other not as widely adopted approximate but very efficient methods for electrically large arrays are the so-called Floquet-mode-based methods [23]. Nevertheless, these methods assume infinite array dimensions and array periodicity to achieve their efficiency. We note that methods based on the Domain Decomposition Method (DDM) allow for computationally efficient array analysis by dividing the full array domain into subproblems in which local solutions are solved first and then coupled together [24–26]. The DDM method performs particularly well when combined with the Finite Element Method (FEM) in case of arrays with complicated stack-ups. Nevertheless, integral-equation-based methods still possess the distinct advantage in inherently satisfying the open boundary radiation condition, eliminating the need for absorbing boundary conditions. In addition, IE methods do not suffer from numerical dispersion and stability issues as is the case for FEM [27].

In the subsequent paragraphs, we seek to categorize existing fast IE-based methods based on their primary characteristics to provide the reader with a clear overview. Note that this is a rough classification, as the different methods may overlap on multiple key parameters.

Green's Function Methods In literature, several mature techniques based on closed-form Green's functions have been employed for the specific class of microstrip patch arrays [28–30]. In principle, these methods could successfully be exploited to yield very efficient algorithms for aperiodic antenna arrays, provided that the specific Green function for that particular array is determined. This is a major drawback

[†]In this dissertation, *Big-O* notation $\mathcal{O}(f(x))$ is employed to denote that the true scaling $g(x)$ of an algorithm as $x \to \infty$ satisfies $|g(x)| \leq C|f(x)|$ for a fixed positive $C \in \mathbb{R}$ for all $x > x_0,\ x_0 \in \mathbb{R}$ [20].

especially in a commercial context in which versatility is key, i.e. the method should be applicable to as many different problems as possible.

MacroBasis Function Methods More versatile and efficient array analysis of general arrays has been made possible by introducing various methods based on MacroBasis Functions [31–33] (MBFs) such as characteristic basis functions (CBF) [34,35], synthetic basis functions (SBF) [36] and accurate subentire-domain (ASED) [37] basis functions. These methods are all quite similar, in the sense that they obtain a compressed version of the MoM matrix by computing a set of problem-matched large-domain basis functions. Nevertheless, the generation and number of MBFs to include is in general problem specific, making the asymptotic scaling difficult to predict. In addition, the basis functions must be chosen to conform with the particular antenna or scatterer in question. Therefore, it seems cumbersome to employ this method especially for general electrically large structures. These methods may, however, be tailored to array problems and/or combined with e.g. the Adaptive Cross Approximation or Multipole expansion technique [38–40]. In any case, one of the biggest impediments of the MBF-based-methods are their inherent partial error-controllability. This stems from the fact that the number of characteristic/macro functions cannot directly be related to the desired number of correct digits in the solution.

Algebraic-Compression-based Methods Whereas MBF-methods obtain compression through aggregating many elementary BFs into fewer groups, other methods focus on algebraic matrix compression. Examples of such include the fast Integral Equation Solver (IES^3) [41], Integral Equation QR algorithm (IE-QR) [42] and Adaptive Cross Approximation (ACA) [43]. These methods can be regarded as algebraic in nature, in that they work by clever grouping and/or by factorization of smaller interaction matrices with the aim of improving the compressibility of the system matrix and thereby accelerating the computation time. Nevertheless, for electrically large problems and highly oscillatory kernels (e.g. the Helmholtz kernel), these algorithms unfortunately suffer from worse than $\mathcal{O}(N^2)$ complexity for both memory and matrix-vector multiplication [44]. Similar methods denoted as fast direct solvers are also based on lossy compression, but focus strictly on efficient factorization and direct solution of the linear system [45–47]. In recent literature [48], these methods have been reported to obtain close to $\mathcal{O}(N \log N)$ computational complexity, but generally suffer from a high setup-time.

Multipole-based Methods Alternatively, the MoM solution can be accelerated by means of the multi-level fast multi-pole method (MLFMM) [49,50], which is a widely used error-controllable full-wave method for electrically large structures [51–53]. The MLFMM can be thought of as an acceleration of the MoM, based on the splitting of the impedance matrix into a near-field part and a far-field part. The near-field interactions are not touched upon by the MLFMM algorithm and are calculated in the usual MoM way. The far-field interactions are calculated by employing a multi-level

space partitioning scheme in which numerous basis functions are grouped on multiple levels. The speed-up is achieved by letting basis functions in the largest feasible groups interact with each other. MLFMM achieves a computational and memory complexity of $\mathcal{O}(N \log N)$. A hybrid MoM/MLFMM for combined array analysis and platform scattering has also been proposed [52], but the full MoM matrix used to characterize the array will quickly exhaust memory resources and this method is only applicable when antenna and platform regions are loosely coupled. Moreover, in conventional MLFMM, sub-wavelength array element sizes and spacings pose a challenge because it does not exploit the typical periodic nature of arrays [54]. By exploiting the Toeplitz property and multi-pole methods simultaneously and assuming that the number of k-space directions are less than the number of unknowns per array element, very efficient array analysis is possible [55, 56], however all elements must be identical.

Grid-based FFT-Methods Another class of fast integral equation methods exploits the circular convolution theorem which allows the use of a Fast Fourier Transform (FFT) to accelerate the solution process. Examples are the precorrected-FFT method (pFFT) [57–59] and the Adaptive Integral Method (AIM) [60, 61] and the Integral Equation Fast Fourier Transform method (IE-FFT) [44]. Common to these methods is the mapping of basis functions (or Green's function) onto a rectangular grid, where the translational invariance of Green's function results in a Toeplitz matrix structure, which in turn enables the calculation of the matrix-vector multiplication by the Fast Fourier Transform (FFT). Besides the obvious approximation when forcing basis functions onto a regular grid, the computational complexity of pFFT and AIM is typically around $\mathcal{O}(N^{1.5} \log N)$ [44, 62] and at best $\mathcal{O}(N \log N)$ [57] for 3D surface problems. Though, it should be noted that the memory requirement for AIM is $\mathcal{O}(N^{1.5})$ for surface problems. In addition, the optimal choice of various algorithm parameters in the AIM can unfortunately not be determined a priori as described in [63]. Lastly, the AIM method seems to be mostly applicable for planar structures [64–67], although successful volumetric implementations do exist [63, 68].

Towards New State-of-the-Art Although most of the methods discussed above are based on analytical and/or physical approximations, they are well-suited to accelerate the analysis of general electrically large antenna arrays because they are fast (computational complexity of $\mathcal{O}(N \log N)$) and some even error-controllable. Nevertheless, when array elements are placed on a regular[‡] lattice, a computational complexity close to $\mathcal{O}(N \log N)$ can be achieved with an accuracy equal to the full MoM solution by employing the Array Decomposition Method (ADM) [56, 69]. This is possible by exploiting the translational invariance of the 3D free-space Green function in connection with the regular geometrical lattice (e.g. rectangular, hexagonal or circular) of the array elements and consecutively ordered basis functions, allowing an FFT-accelerated matrix-vector product (MVP) in an iterative solution process [70, 71].

[‡]In this dissertation, the term *regular array* refers to an arrangement of array elements which are placed equidistantly along each lattice dimension, including non-orthogonal and circular lattices.

The ADM stands out as an accurate full-wave solver for antenna arrays for space application because it does not resort to any approximations other than those inherent to surface discretization and the iterative solution process. Nonetheless, its inability to cope with arrays with interconnecting geometry, sparse or aperiodic arrays and non-identical elements presents notable impediments. Overcoming these, and other shortcomings of the ADM will be the fulcrum of the remainder of this dissertation.

1.4 Original Contributions

This dissertation presents the following original contributions to the field of computational electromagnetics in the framework of array analysis:

- **Development of HO-ADM for Regular Arrays:** The existing boundary integral part of the Array Decomposition Method (ADM) has, for the first time, been combined with higher-order basis functions. Numerical tests have verified that this combination, denoted HO-ADM, leads to more than an order of magnitude lower memory consumption and faster computation times compared to ADM employing traditional first-order basis functions. Furthermore, for the first time, higher-order convergence has been demonstrated for ADM in combination with hierarchical higher-order basis functions.

- **Arrays with Interconnecting Geometry:** The HO-ADM has been extended to allow for the flow of electric conduction currents between array elements. This advancement was realized using a unique application of the established Discontinuous Galerkin Method. As a result, the corresponding Method of Moments (MoM) matrix maintains its block-Toeplitz property which more importantly ensures that the HO-ADM continues to benefit from its FFT-accelerated matrix-vector product. The effective solution is made possible by realizing an asymptotically constant-memory preconditioner applicable for HO-ADM.

- **Aperiodic Arrays with Non-identical Elements**: The functionality of HO-ADM has been expanded to accommodate non-uniform arrays, such as sparse or thinned arrays, through selective truncation of the Krylov subspace in the iterative solution process. Furthermore, with the introduction of a super unit-cell (SUC) strategy, the method can handle non-identical elements while maintaining computational efficiency across various element configurations.

- **Integration with Dielectric Substrates**: The constrained Krylov subspace idea is used together with special geometrical meshing to allow the HO-ADM to handle arrays with a dielectric substrate, broadening the solver's applicability across a myriad of array designs.

1.5 Organization of the Dissertation

The dissertation is organized as follows:

- **Chapter 1** introduces the scope of the present study (Section 1.1) and provides a thorough review, discussion, and classification of existing computational electromagnetic surface-integral-equation methods (Section 1.3) for the analysis of antenna arrays.
- **Chapter 2** presents common array configurations which have been designed for space applications (Section 2.1) and seek to provide the reader with a concise but sufficient understanding of the computational method (ADM) which lays the foundation of the present study (Section 2.2). The importance and implications of extending ADM with HO BFs (HO-ADM) are discussed in detail in Section 2.3, and its performance is assessed through several numerical test cases.
- **Chapter 3** examines the extensions necessary for the analysis of thinned array antennas (Section 3.1), as well as extensions allowing electrically connected elements, i.e. where conduction currents are allowed to flow between array elements (Section 3.2). The chapter concludes with numerical validation examples, demonstrating the efficiency and real-world applicability of the HO-ADM by comparisons with a state-of-the-art HO-MLFMM implementation.
- **Chapter 4** provides additional extensions to the HO-ADM, allowing for array antennas with non-identical elements (Section 4.1), as well as finite thickness structures which can be modeled as array antennas, such as arrays with dielectric substrates (Section 4.2).
- **Chapter 5** gives a comprehensive overview of the key findings and conclusions from the research conducted and presented in this dissertation.

To allow for consistent interpretation of key terms and phrases, Appendix D provides their definitions as used throughout this dissertation. An $e^{j\omega t}$ time-dependence, with $\omega = 2\pi f$ the angular frequency, is assumed and suppressed throughout the dissertation.

CHAPTER 2

ADM with Higher-order Basis Functions

This chapter begins with an overview of both traditional and contemporary state-of-the-art antenna arrays for space applications, establishing the context for the applications of the developed method (Section 2.1). Next, the standard Array Decomposition Method (ADM) is briefly described (Section 2.2), after which the importance and implications of its extension with higher-order basis functions is discussed (Section 2.3). The performance of the extended method is assessed through numerical validation examples, including comparisons with a state-of-the-art MLFMM implementation [16].

We note that the term "standard ADM" refers to the boundary integral (BI) part of the method described in [69], which is neither applicable to connected, aperiodic nor to non-identical-element antenna arrays. The term "extended method" is henceforth referred to as the Higher-Order Array Decomposition Method (HO-ADM). While this dissertation discusses each extension to the developed method separately for clearer comprehension, the label HO-ADM is used to denote any number of these extensions, without distinguishing which ones are incorporated in each instance of its use. The most significant parts of the work in this chapter are presented in papers [J1], [C1] which are found under Publications.

2.1 Array Antennas for Space Applications

Antennas deployed in space must ensure reliable data transmission and reception through electromagnetic waves while being resistant to extreme temperature variations, cosmic radiation, and potential micrometeoroid impacts, which necessitate robust designs and the use of durable materials [72]. As discussed in Chapter 1, reflector antennas have been the traditional choice for space payloads due to their ability to provide a high gain at low cost. Nevertheless, both array fed reflectors and direct radiating array antennas have gained considerable attention for space applications due to their flexibility in beam shaping, electronic steering, and modular design [73].

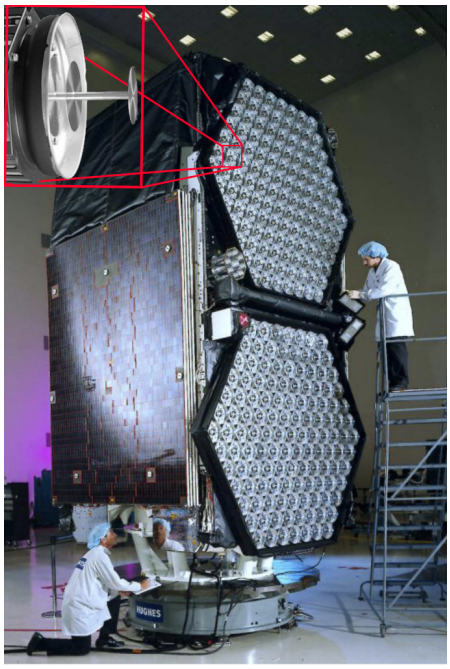

(a) Two All-Metal 127-element direct radiating array for MEO communication at S-band [74].

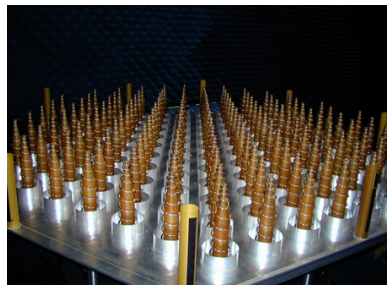

(b) L-band 120-element feed array for the Inmarsat-4 satellite for GEO communication [75].

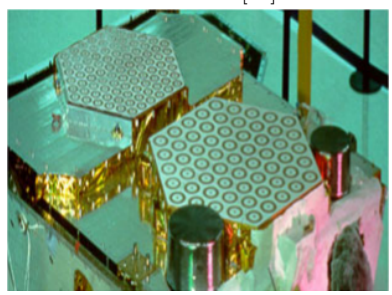

(c) L- and S-band phased array antenna structures for the Globalstar-1 satellite for LEO communication [76].

Figure 2.1: Examples of array antennas used for space applications

Examples of such array antennas designed for space, operating in different orbits with diverse applications and for various frequency bands are shown in Figure 2.1. Herein, we observe that antennas intended for space typically comprise metal-only radiating elements. The primary reason is that dielectric materials accumulate charged particles, which can result in electrostatic discharges that disrupt communications. Moreover, all-metal designs offer superior radiation efficiency and are more resilient to high temperature fluctuations. Therefore, antenna elements constructed entirely of metal remain the preferred choice for in-orbit space applications even today [74,77–79].

Figure 2.1 (a) showcases two all-metal Direct Radiating Arrays (DRAs), which have been designed by Hughes for ICO Global Communications Ltd. for satellite mobile communication in the Medium Earth Orbit (MEO) in the S-frequency band. It features an all-metal patch excited cup as a radiating element, specifically designed to reduce passive intermodulation (PIM) products. For both arrays, the 127 elements are placed on a regular grid and the array is hexagonally thinned. Another example is the

(d) All-metal X-band phased array antenna for the extreme environments of a potential Europa Lander [77].

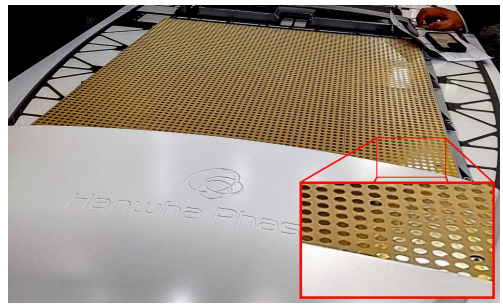

(e) The Hanwha Phasor A7700 Ku-band phased array antenna for OTM satellite communication [80].

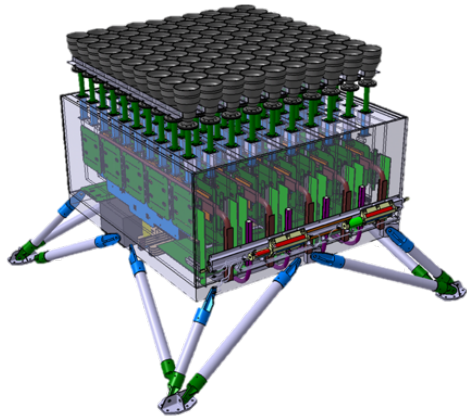

(f) CAD illustration of the Electronically Steerable Antenna (ELSA+) up-link direct radiating array for the Eutelsat Quantum satellite [8].

Figure 2.1: Examples of array antennas used for space applications (cont.)

L-band Feed Array for the Inmarsat-4 Satellite shown in Figure 2.1 (b). It is designed to support the Broadband Global Area Network (B-GAN) from the Geostationary Earth Orbit (GEO). The array features 120 helical radiating elements arranged inside an 8-sided polygon, i.e. a thinned regular triangular lattice. Figure 2.1 (c) shows the L- and S-band Phased Array Antenna structures designed for the Globalstar-1 mission to support mobile satellite voice and data. The L-band and S-band arrays comprise 61 and 91 patch-in-cavity elements, respectively. The elements are placed on a regular grid and the array is hexagonally thinned, as is the case for the ICO DRA.

A state-of-the-art all-metal X-band phased array antenna for space is shown in Figure 2.1 (d), which is proposed as a potential candidate for an Europa[†] Lander. It

[†]Europa is the smallest of the four Galilean moons orbiting the planet Jupiter.

comprises $32 \times 32 = 1024$-elements in a regular rectangular grid, and achieves dual-band right-hand circularly-polarized (RHCP) radiation for Direct-To-Earth (DTE) communication with a single feed-pin per element. A modern user-terminal is the Hanwha Phasor A7700 antenna as seen in Figure 2.1 (e). This Ku-band phased array antenna is specifically developed for On-The-Move (OTM) scenarios, with dual simultaneous receive channels and a single transmit channel. It consists of 4096 circular patch radiating elements arranged as 4×4 sub-arrays each with 16×16 elements.

Last but not least, Figure 2.1 (f) provides a detailed CAD illustration of the Electronically Steerable Antenna (ELSA+), which is the central up-link DRA for the Eutelsat Quantum Satellite which was launched in July 2021 [8, 81]. It consists of $10 \times 10 = 100$ spline-profile horn antennas operating in the Ku frequency band [10], achieving a dual linearly polarized radiation pattern.

In summary, both traditional and state-of-the-art array antennas employ elements placed on a regular but not necessarily orthogonal lattice which may be thinned to reduce weight, cost and power requirements. In subsequent paragraphs we will explore how to do fast analyses of these common array configurations using the full-wave and rigorous Array Decomposition Method.

2.2 The Array Decomposition Method

In the context of integral equation methods for computational electromagnetics, any arrangement of elements (antennas or scatterers) on a lattice for which the interaction[†] between the elements depends on their relative rather than their absolute positions (i.e. translational invariance) will allow for a Toeplitz [82, 83] structure in the resulting system matrix. This special matrix structure is what facilitates an FFT-accelerated MVP in the Array Decomposition Method [69] without using approximations.

Figure 2.2 illustrates two common arrangements of elements (rectangular and circular) which are compatible with the ADM, i.e. they both lead to translationally invariant interactions. The elements are placed in a lattice defined by the lattice vectors $\vec{i}_1, \vec{i}_2, \vec{i}_3$ with inter-element distances defined by $||\vec{i}_1||, ||\vec{i}_2||, ||\vec{i}_3||$. The resulting MoM matrices for both configurations have been depicted to provide a clear understanding of the connection between the physical arrangement of elements and the block-Toeplitz (BT) structure.

For reasons that will soon be apparent, we define the total number of unknowns for a given array in a slightly unconventional manner as

$$N = s \prod_{i=1}^{d} n_i = sT, \tag{2.1}$$

[†]In this dissertation, the term *interaction* is used to denote the result of calculating the *Moments* (inner products between basis functions and the Green function) in the MoM-matrix, corresponding to the interaction between two (or more) elements.

where s is the number of unknowns on each array element, T is the total number of array elements, d is the number of lattice dimensions, and n_i is the number of elements in the i^{th} lattice dimension. Next, we consider an array with $T = 2 \times 3 \times 2 = 12$ identical elements placed on a $(d = 3)$-dimensional cubic lattice as shown in Figure 2.2 (a). Provided that the basis functions for each element are generated consecutively in the order of each lattice dimension, as indicated with numbers on each array element, we get the Multi-level Block-Toeplitz (MBT) MoM matrix as depicted in Figure 2.2 (b), in which colors indicate the $d = 3$ levels. That is, the MoM matrix consists of $n_d \times n_d$ BT matrices which themselves consist of $n_{d-1} \times n_{d-1}$ BT sub-blocks, and so forth for the number of array lattice dimensions d. At the inner-most level we have $n_1 \times n_1$ blocks of size $s \times s$ which do not, in general, possess any special structure.

Notably, an MBT structure also arises if elements are placed regularly in a cylindrical coordinate system as depicted in Figure 2.2 (c)[†]. It is important to note that for the interactions to be translational invariant in the cylindrical coordinate system, each element must be sequentially rotated around the axis defined by $\vec{i}_3$ (z-axis) such that the sum of rotations going around in azimuthal direction equals 2π rad. This is a consequence of the finite extent of the array elements when placed on the perimeter of a circle. As shown in the example in Figure 2.2 (c), we have $T = 1 \times 7 \times 2 = 14$ element array which gives rise to 2×2 BT matrices which themselves consist of 7×7 already block-circulant (BC) matrices, see Figure 2.2 (d). As is the case for the cubic lattice, the inner-most level also consists of arbitrary matrices without any special structure.

For both cases, an MVP computational complexity close to $\mathcal{O}(N \log N)$ can be achieved by rearranging the sub-blocks at each level $i \in \{1, \ldots, d\}$ from Toeplitz to circulant [84, sec. 4.7.7] stored in a 5 (or 4)-dimensional tensor $\mathbf{C}(m, n, j, k, l)$ on a cubic (or rectangular) lattice, which will henceforth be denoted the circulant generator. Herein, $j \in \{1, \ldots, 2n_1 - 1\}$, $k \in \{1, \ldots, 2n_2 - 1\}$ and $l \in \{1, \ldots, 2n_3 - 1\}$ enumerate the rearranged blocks at the first $(i = 1)$, second $(i = 2)$ and third $(i = 3)$ block-circulant level, respectively. The indices $m = \{1, \ldots, s\}$ and $n = \{1, \ldots, s\}$ enumerate MoM matrix entries at the lowest level. With the circulant generator at hand the MVP becomes a discrete circular block convolution operation over the indices (j, k, l), which can be accelerated via the FFT. For more implementation specific details, the reader is referred to [J1]. We note that an FFT-accelerated direct solution would be possible[‡] provided that the arbitrary blocks at the inner-most level had Toeplitz property as well. Nevertheless, since the arbitrary blocks are inevitable at the inner-most level, a quadratic computational complexity scaling arises in the number of basis functions per element (s^2). This holds true both for computing the

[†]Note that only one layer (ring) of elements is placed in the $\vec{i}_1$-dimension for illustrative simplicity.

[‡]The solution to a linear system $\mathbf{C}\vec{x} = \vec{b}$ in case $\mathbf{C}$ is (block-)circulant matrix can be found directly via three d-dimensional discrete Fourier transforms $(\mathcal{F}_d)$ as $\vec{x} = \mathcal{F}_d^{-1}\left\{\frac{\mathcal{F}_d\{\vec{b}\}}{\mathcal{F}_d\{\vec{c}\}}\right\}$, in which $\vec{c}$ is the first row or column of $\mathbf{C}$. This would allow an $\mathcal{O}(N \log N)$ direct solution.

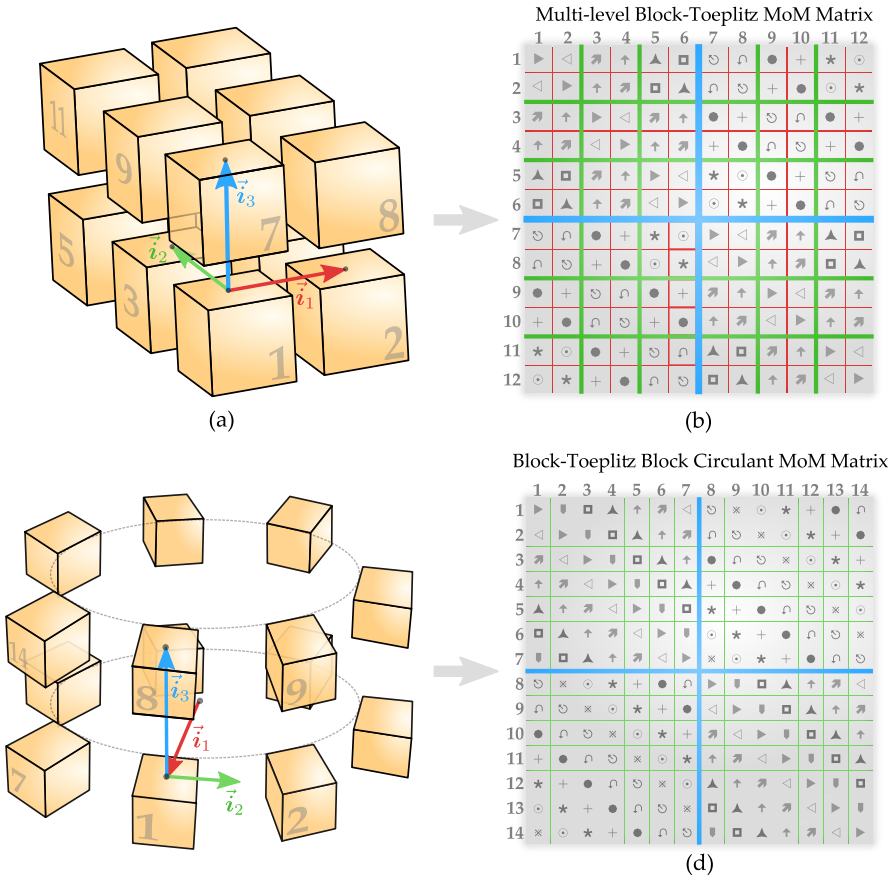

Figure 2.2: Illustration of lattice arrangements which give rise to a multi-level block-Toeplitz (MBT) matrix structure. (a) $T = 2 \times 3 \times 2 = 12$ elements on a rectangular (cuboidal) lattice, and (b) the associated MoM matrix. (c) $T = 1 \times 7 \times 2 = 14$ elements on a cylindrical lattice with (d) the associated MoM matrix. – Colors simultaneously indicate lattice dimensions and the multi-levels of the resulting MoM matrix. Symbols are used to indicate similar matrix blocks at the inner-most level. Note that the illustration does not represent a discretized structure and that the cube represents any volumetric scatterer described by a surface mesh.

FFT-accelerated matrix-vector product and for computing the unique blocks of the MoM matrix during the setup phase.

The quadratic scaling may not be immediately apparent if the computational complexity of ADM is expressed in the standard form $\mathcal{O}(sN \log \frac{N}{s})$. Therefore, by using (2.1), the MVP computational complexity can be reformulated in a more comprehen-

sible manner as $\mathcal{O}(s^2 T \log T)$. On the one hand, this scaling is favorable in terms of number of array elements T, making it well suited for electrically large arrays. On the other hand, the number of basis functions on each array element must not be too large due to the quadratic scaling in s. The same conclusions can be made for the memory complexity of ADM, which is dominated by the storage of the circulant generator $\mathbf{C}$, which amounts to an asymptotic memory complexity of $\mathcal{O}(s^2 T)$ (or $\mathcal{O}(sN)$). For reference, this is a factor of $\frac{T}{2^d}$ less memory than that of full MoM. For a more thorough explanation and analysis of the computational and memory complexities of the setup-phase, MVP and iterative solution process of ADM, the reader is directed to Appendix B. It is important to acknowledge that, although the memory scaling of ADM is linear with respect to the number of array elements, the inherent quadratic scaling with number of unknowns per element, s, may quickly deplete available resources. Nevertheless, as we shall see shortly, by employing HO-hierarchical BFs, s can be kept low (compared to ordinary first-order BFs) without impacting the solution accuracy, leading to both reduced memory consumption and computation time. See definitions of memory consumption and computation time in Appendix D.

2.3 Higher-Order Basis Functions in ADM

In this section the implications and importance of combining higher-order basis functions with the Array Decomposition Method (HO-ADM) is discussed. First, the efficacy of employed basis functions is shown via a higher-order convergence study on an array of spheres as well as on an array of cubes. Next, the efficiency of HO-ADM is shown for a practical case of a 10×10-element conical horn array. Lastly, we discuss the implications of using HO basis functions with respect to the scaling of HO-ADM and an existing fast method.

The use of higher-order basis functions is well-known to provide accurate approximations of the induced currents with fewer unknowns compared to lower-order basis functions [85, 86]. In the HO-ADM, curved quadrilaterals (i.e. mesh cells), also referred to as quads, with parametrization $\vec{r}(u, v)$ are used to discretize the geometry [87], using the HO-hierarchical Legendre BFs from [88] to expand the surface current density. For more details, the reader is referred to [17] and [J2]. The primary advantage of these BFs lies in the application of the modified Legendre polynomials $\tilde{P}_m(u)$ defined as

$$\tilde{P}_m(u) = \begin{cases} 1-u, & m=0 \\ 1+u, & m=1 \\ P_m(u) - P_{m-2}(u), & m \geq 2 \end{cases} \begin{matrix} \} \\ \} \\ \} \end{matrix} \begin{matrix} \textbf{Doublets} \\ \\ \textbf{Singletons} \end{matrix} , \tag{2.2}$$

where $m = \{0, \ldots, \rho\}$ enumerates the different orders for a given quad and ρ is the maximum BF order used in that quad. The modified Legendre polynomials inherently satisfy current continuity between quads for orders $m = 0, 1$ and they correspond to the usual roof-top BFs having support over two quads. In addition,

local surface current density variations are modeled by a summation of ordinary Legendre polynomials for orders $m \geq 2$ which have support only within a single quad.

Other BF-formulations, e.g. Rao-Wilton-Glisson [89] BFs on triangular cells can be used as well. Nevertheless, by using quads (instead of triangular cells) only two vectors (instead of three) are needed to represent the current, which, combined with the choice of the HO BFs, enables better accuracy for the same number of unknowns. Furthermore, it is worth noting that while the extension of ADM with interpolatory HO BFs is possible, hierarchical BFs are generally favored due to the following reasons:

- Hierarchical bases allow for different expansion orders on different elements in the same mesh. This allows for adaptive refinement, where the maximum polynomial order ρ is chosen independently for each quad based on its electrical size.

- Compared to interpolatory bases, hierarchical bases often lead to lower condition numbers, which can improve the efficiency of the iterative solution process, [17].

2.3.1 Higher-Order Convergence

Besides the advantages already discussed, the use of higher-order basis functions is also driven by the desire to achieve higher-order convergence, that is, the numerical approximation error should theoretically behave as $O(h^\rho)$ for $h < 1$, where h denotes the mesh size [90]. This means that increasing the maximum polynomial order ρ, as opposed to decreasing the mesh size, should always yield a lower error for the same number of unknowns. This property has been verified for a single sphere for MoM [17] and MLFMM [91]. In this dissertation, HO-convergence is verified also for an array of scatterers using HO-ADM [J1].

The subsequent numerical tests of this chapter have been carried out on a laptop and a computational server with specifications as outlined in Table E.1. The Generalized Minimal Residual (GMRES) iterative solver is used with a relative residual error tolerance of 10^{-3}. We note that for the remainder of this dissertation, the term "computation time" refers to the total wall-clock time it takes for a given algorithm to retrieve the desired solution. For HO-ADM, this means the creation of BFs, computation of the circulant generator and its d-dimensional FFT, the preconditioner generation and associated factorization as well as the iterative solution time. The term "memory consumption" refers to the peak memory used during the execution of a given algorithm. For HO-ADM, this implies storage of the circulant generator, the Krylov subspace, and the entire preconditioner. The preconditioner used throughout this chapter is the block-diagonal preconditioner $\mathcal{M}_{NC}$ described in Section 3.3.

In Figure 2.3 two 5×5 arrays of PEC spheres and cubes are shown. The arrays are illuminated by an $\vec{x}$-polarized plane wave propagating along the z-axis, and the resulting normalized induced surface current densities of the center elements are shown

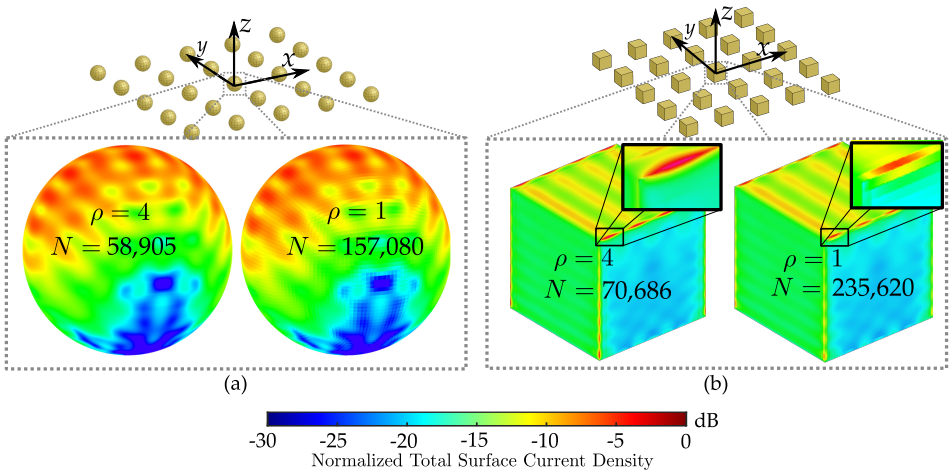

Figure 2.3: Two 5×5 arrays illuminated by a plane wave propagating in the negative z-direction. Zoom-in shows the induced normalized surface current density calculated with HO-ADM for different polynomial orders $\rho = \{1, 4\}$. The corresponding number of unknowns to achieve an equivalent relative error of 1 % in the scattered far field is also shown. (a) PEC sphere array with $D = 5\lambda$ diameter (b) PEC cube array with $L = 3.61\lambda$ side length.

for BF orders $\rho = 1$ (normal roof-top basis functions) and $\rho = 4$. The spheres in Figure 2.3 (a) have a diameter of $D = 5\lambda$ while each cube in Figure 2.3 (b) has a total surface area equal to that of a sphere resulting in a side length of $L = \frac{D}{2}\sqrt{\frac{2}{3}\pi} = 3.61\lambda$. For both the spheres and cubes, h-refinement has been applied until reaching an Equivalent Relative Error, Eq. (10) in [J2], in the scattered far-field which is less than 1 %. It is immediately apparent that using fourth-order BFs ($\rho = 4$) qualitatively yields a smoother approximation of the true induced current densities, and more importantly, that less unknowns are needed when using fourth-order BFs compared to ordinary roof-top BFs for both the sphere ($N_{\text{sphere},\rho=4} = 58,905 < N_{\text{sphere},\rho=1} = 157,080$) and the cube ($N_{\text{cube},\rho=4} = 70,686 < N_{\text{cube},\rho=1} = 235,620$).

A more quantitative analysis has been conducted with results shown in Figure 2.4 in which the relative far-field error ϵ_{ERE}[†] is plotted versus the discretization density h_λ (i.e. the number of unknowns normalized by total surface area in square wavelengths), for four different fixed polynomial orders $\rho = \{1, 2, 3, 4\}$. For the purpose of showing HO-convergence, the polynomial order has been fixed on all mesh cells[‡].

For a discretization density $h_\lambda < 20$, the use of polynomial orders greater than 1 ($\rho > 1$) does not lead to significantly improved accuracy for neither the array of

[†]The reference is a direct solution of the full HO-MoM matrix with high integration precision and as fine a discretization as possible within memory limits of the available laptop (see Appendix E).
[‡]In practice, a heuristic adaptive approach based on electrical size is employed.

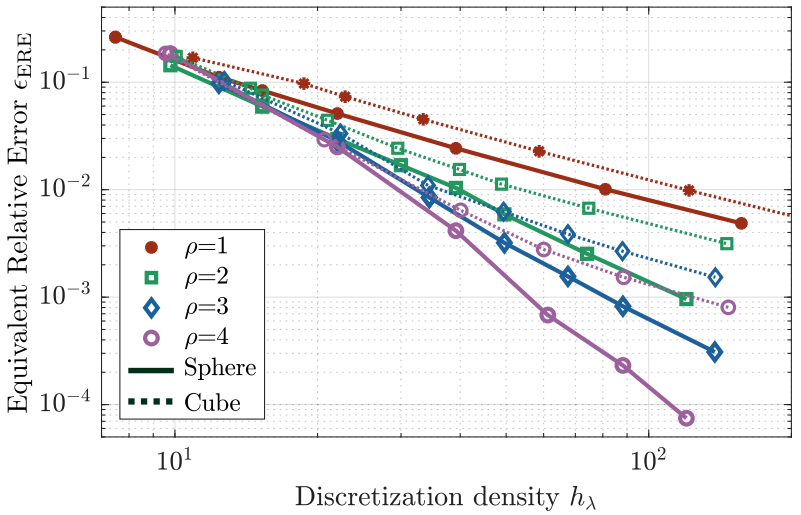

Figure 2.4: Equivalent Relative Error ϵ_{ERE} [J2] as a function of the discretization density h_λ for a 5×5 array of spheres and cubes with the same surface area, i.e. $L = 3.61\lambda$, $D = 5\lambda$.

spheres nor the array of cubes. However, once the discretization density exceeds $h_\lambda > 20$, we start to observe a noticeable difference between results for various polynomial orders. Particularly, when the discretization density is $h_\lambda > 100$ in case of the sphere array, the accuracy of the far-field for a polynomial order of $\rho = 4$ is about two orders of magnitude better than that for a polynomial order of $\rho = 1$ for the same number of unknowns. In addition, for higher polynomial orders, the slopes of the error curves increase according to the theoretical prediction of $\mathcal{O}(h^\rho)$.

Interestingly, the array of cubes exhibits the expected HO-convergence behavior only to a limited extent when the discretization density is moderately low, specifically within the $10 < h_\lambda < 40$ range. Beyond this, particularly for $h_\lambda > 40$, the HO-convergence behavior is not observed. Although the use of higher orders $\rho > 1$ do seem to decrease the relative error for a given number of unknowns, the slope of the error curves for the cube array eventually follows that of the first-order BFs. A major reason for this discrepancy could be that the singular current density near the edges of the cubes (see Figure 2.3 (b)) is not readily captured by the employed non-singular BFs.

In summary, higher-order convergence has been shown using the HO-ADM for an array of spheres, but not for an array of cubes. It is, nevertheless beneficial to employ HO BFs because they in any case provide higher accuracy than first-order BFs for the same number of unknowns. Furthermore, as we shall see shortly, the use of HO BFs provides significantly faster computation time and lower memory consumption compared to the use of first-order BFs in the HO-ADM.

2.3.2 Lower Computation Time & Memory Consumption

Inspired by the 100-element Eutelsat Quantum horn array in Figure 2.1 (f), we consider the DRA with dimensions as depicted in Figure 2.5, which consists of 10×10 conical horn antennas fed by circular waveguides excited uniformly with the fundamental mode TE_{11}. The induced surface current density has been calculated using the HO-ADM on a laptop and the radiated far-field pattern has been compared to a reference using the equivalent relative error $\varepsilon_{\mathrm{ERE}}$. The reference solution has been generated by using the smallest mesh cells possible (h-refinement) with a maximum BF order of $\rho = 5$, on the available server with specifications defined in Appendix E.

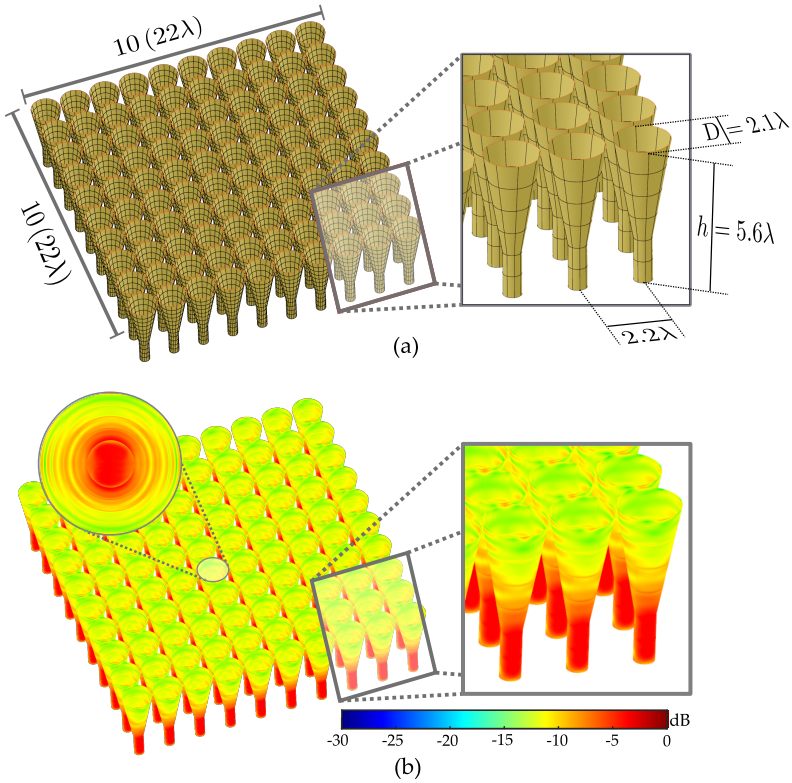

Figure 2.5: 10×10-element conical horn array inspired by the Eutelsat Quantum array in Figure 2.1 (f). (a) Primary dimensions of the array and radiating elements are shown in wavelengths. (b) The normalized surface current density of the array.

Figure 2.6 shows the total computation time (left axis) and memory consumption (right axis) in the HO-ADM using fixed BF orders from $\rho = 1$ to $\rho = 4$. The graph distinguishes between the computation time spent during the initialization of HO-

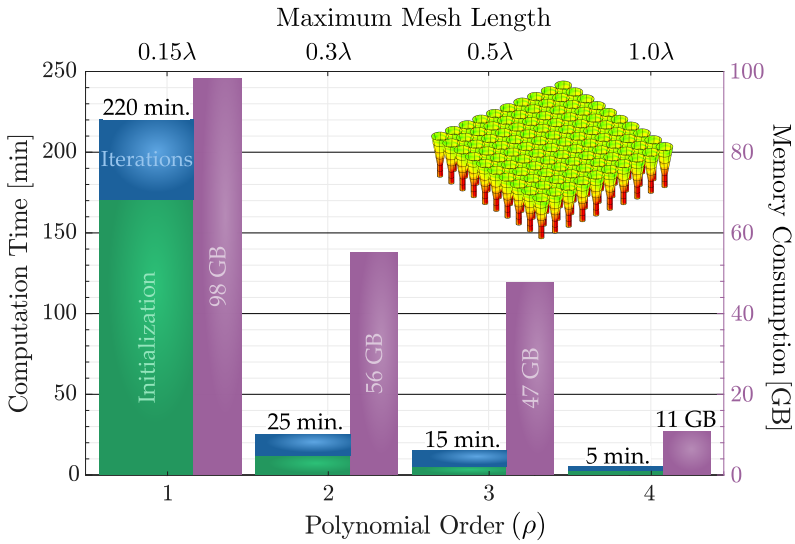

Figure 2.6: Computation time and memory consumption versus a fixed BF polynomial order, using HO-ADM for the DRA of Figure 2.5. The maximum mesh length required to reach a far-field relative error below 1 % for a given polynomial order is shown on the top horizontal axis.

ADM (setup-phase) and the time spent in the iterative solution process. For each fixed order ρ, the mesh length l has been varied between $l = 0.15\lambda$ and $l = 1.0\lambda$ to ensure an ϵ_{ERE} in the radiated far-field forward hemisphere that is less than 1 %. Key simulation data is tabulated in Table 2.1, including the number of mesh cells used, total number of unknowns and the achieved equivalent relative error.

Polynomial Order ρ	Mesh Cells	Total Unknowns N	Setup Time	Relative Error ϵ_{ERE}
1	288,400	574,000	77 %	0.97 %
2	54,000	429,600	48 %	0.49 %
3	22,400	400,000	35 %	0.25 %
4	6,000	190,400	38 %	0.92 %

Table 2.1: HO-ADM simulation data for the 10×10 conical horn array of Figure 2.5.

For a fixed BF order of $\rho = 1$ (roof-top BFs), the mesh length had to be decreased to $l = 0.15\lambda$[†] resulting in 288,400 mesh cells, corresponding to $N = 574{,}000$ unknowns, to reach a relative far-field error of 0.97 %. Remarkably, in this case, the HO-ADM uses 77 % of the total solution time (220 min) in the setup-phase, in which the unique blocks of the circulant generator is calculated.

By increasing the polynomial order to $\rho = 2$, significantly less mesh cells (54,000) are needed at the expense of more unknowns per mesh cell, resulting in a total of $N = 429{,}600$ unknowns. This modest decrease in total number of unknowns from $\rho = 1$ to $\rho = 2$ suggests that the nine times higher computation time 220 min for $\rho = 1$ compared to 25 min for $\rho = 2$ is caused by the large number of integrals (and Green function evaluations) to be computed for $\rho = 1$ and not to the same extent the quadratic scaling in s.

The mesh is more refined for $\rho = 2$ and $\rho = 3$, resulting in a two and four times lower error, respectively, than the solution for $\rho = 1$ and $\rho = 4$. This increased accuracy is the primary reason for the relatively small decrease in total number of unknowns, memory consumption and computation time from $\rho = 2$ to $\rho = 3$[†].

A significant fourfold reduction in memory consumption, going from 47 GB to 11 GB, as well as a threefold reduction in computation time from 15 min. to 5 min. is evident going from $\rho = 3$ with 22,400 mesh cells to $\rho = 4$ with 6,000 mesh cells. We note that increasing the polynomial order above four for the present example does not provide any additional benefits as higher orders $\rho > 4$ do not provide increased accuracy.

In summary, the results clearly demonstrate the power of using HO BFs in combination with ADM yielding an efficient solver which can be used in practice. This is most clearly demonstrated going from BF order $\rho = 1$ to $\rho = 4$, where the total computation time decreases by a factor of circa 40 and the memory consumption decreases by a factor of about 10, making it possible to analyze a 100-element conical horn array on a laptop in five minutes.

2.3.3 Computational Complexity in Higher-Order Schemes

While computational complexity, the asymptotic scaling of an algorithm, is a theoretical measure which offers a good basis of comparison between methods, it abstracts away the constants and practical considerations that affect the actual computation time. In this section, we take a closer look at the actual computation time and memory consumption of HO-ADM and compare it to the state-of-the-art HO-MLFMM. When looking at the actual scaling of algorithms, it is customary to plot computation time and/or memory consumption as a function of increasing total number of

[†]This mesh size is in line with the widely recognized $l = \lambda/10$ rule-of-thumb for a good compromise between computational efficiency and solution accuracy for first-order BFs [92].

[†]It should be noted that since only the desired max mesh length can be specified for the meshing-routine, the actual mesh sizes can only be varied in discrete steps. Consequently, the relative error might end up lower than 1 %.

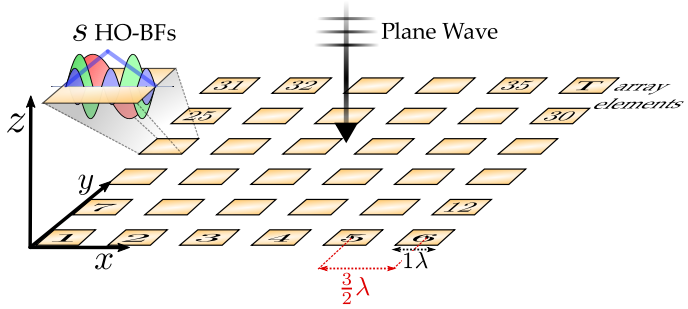

Figure 2.7: Plane wave normally incident on an array of T PEC plates of size $1\lambda \times 1\lambda$ with inter-element distance of 1.5λ. There are s HO BFs on each array element.

unknowns, N. There are, however, several approaches to increase the number of unknowns for array antennas in higher-order schemes:

- Varying the mesh length h (h-refinement)
- Varying the polynomial order ρ (ρ-refinement)
- Varying the total number of array elements T

The first approach, h-refinement, is the only way to increase the number of unknowns for a fixed array size T in traditional first-order schemes. For higher-order schemes, increasing the polynomial order, ρ, offers an additional degree of freedom. This means that the number of BFs per element, s, can be varied both through h- and ρ-refinement. Finally, for arrays in general, the total number of array elements T can be increased for fixed mesh size h and polynomial order ρ. Each of these approaches can have significantly different influence on the practical scaling behavior of a given algorithm as we shall see in the following.

The HO-MLFMM has a theoretical computational and memory complexity of $sT\log(sT)$, whereas HO-ADM has a theoretical computational and memory complexity of $s^2T\log(T)$ and s^2T, respectively. Consequently, HO-MLFMM and HO-ADM should scale equally in computation time when increasing the number of array elements (T) for a fixed number of BFs on each array element (s) and fixed polynomial order. In the same case, the memory complexity of HO-ADM should theoretically scale better than HO-MLFMM. Nevertheless, as we shall see shortly, the quadratic scaling in s quickly makes the actual memory consumption of HO-ADM exhaust available resources.

To assess the scaling of HO-ADM and HO-MLFMM we consider as example an array of T PEC plates of size $1\lambda\times1\lambda$ with inter-element distance of 1.5λ as in Figure 2.7, which is illuminated by a normally incident plane-wave. In the first study, the total number of unknowns, N, is varied by increasing the total number of array elements T for three different constant numbers of BFs per array element $s = \{60, 496, 992\}$

and for a fixed polynomial order of $\rho = 2$. Figure 2.8 shows the resulting computation time and memory consumption for HO-ADM and HO-MLFMM when run on the compute server with specifications given in Appendix E.

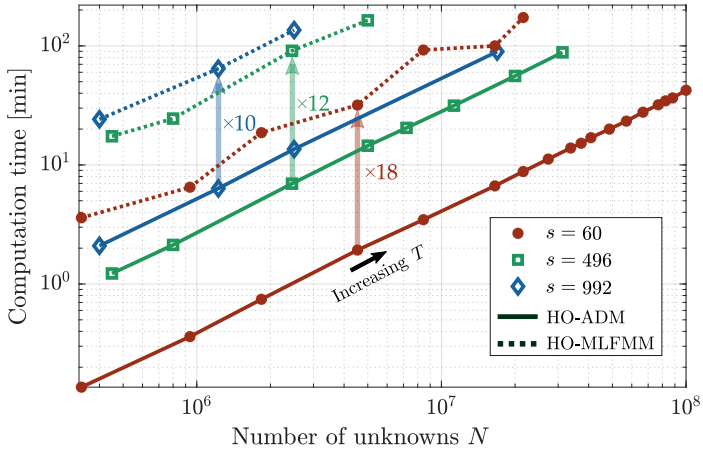

(a)

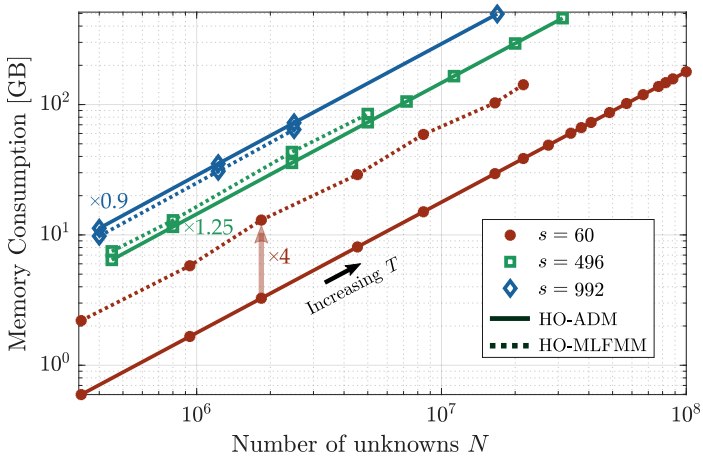

(b)

Figure 2.8: Computation time and memory consumption for HO-ADM and HO-MLFMM applied to the array of plates as seen in Figure 2.7 for constant number of basis functions per array element $s = \{60, 496, 992\}$ and a constant polynomial order of $\rho = 2$. h-refinement is used to increase the number of unknowns per array element, s.

In Figure 2.8, we observe that in HO-ADM for $s = 60$ and 100 million unknowns, the simulation takes 44 min with a memory consumption of 179 GB. Nevertheless, for the same memory consumption but with $s = 992$, the HO-ADM can handle 17 times less unknowns (circa six million unknowns) for which the simulation takes 32 min. With almost the same memory consumption (155 GB), the HO-MLFMM is able to solve a system of approximately 20 million unknowns in 170 min for $s = 60$, and four times less unknowns (5 million unknowns) in 150 min for $s = 992$. As a result, for the same total memory consumption, the HO-ADM can simulate arrays with more elements, T, given that the same element discretization, s, is used. At the same time, for the same T and s, the HO-ADM is faster than HO-MLFMM.

Another key observation is that the computation time for HO-ADM is 18 times faster than HO-MLFMM for $s = 60$, whereas for $s = 992$ it is 10 times faster than HO-MLFMM, which suggests that a break-even point in terms of computation time exists. Here, it should be mentioned that the break-even value for s is strongly problem-dependent; that is, it varies significantly with the complexity of the individual elements and how many array elements are considered. From our investigations, we found that in terms of computation time the asymptotic break-even point, s_∞ for $T \to \infty$ (infinite number of array elements) is on average in the order of 4,000 BFs per element but can vary from 1,000 to 10,000 and even higher.

The break-even point between HO-ADM and HO-MLFMM in terms of memory consumption is for the plate array around a thousand BFs per array element as seen in Figure 2.9 (b). Keep in mind that for a fixed array element discretization, s can be considered constant, hence the memory consumption of HO-ADM ($\mathcal{O}(s^2T)$) will eventually become smaller than that of HO-MLFMM ($\mathcal{O}(sT \log sT)$). Unfortunately, this happens beyond the problem sizes which are possible to simulate on the hardware at hand. It is, however, worth noting that the MVP accuracy of the HO-ADM is equivalent to that achieved by employing the full Method of Moments.

As a partial conclusion, because the computational complexity of HO-ADM and HO-MLFMM remains the same for electrically large arrays (larger T), the key advantage of HO-ADM lies in a lower computational complexity constant, offering a more time efficient performance in practice, with a solution accuracy identical to that of full MoM.

Figure 2.9 shows the results of the second and third studies in which we fix the total number of array elements to $T = 50 \times 50 = 2500$ and vary the total number of unknowns by both h- and ρ-refinement. In Figure 2.9 (a), we see that regardless of using h- or ρ-refinement in HO-ADM, it uses the same memory and computation time for a fixed number of unknowns, N. This is, however, for HO-MLFMM only the case for a total number of unknowns less than 1 million, above which the computation time between h- and ρ-refinement starts to diverge. We observe that with a polynomial order above four the MLFMM computation time curve tends towards a quadratic scaling. The main reason is that in case of finer mesh-discretization, the MLFMM algorithm in general is able to do better spatial subdivisions (refine the Octree) which is not possible with a fixed discretization and increasing BF polynomial order. Nevertheless, as it is seldom necessary to use $\rho > 4$ on all mesh cells, this scal-

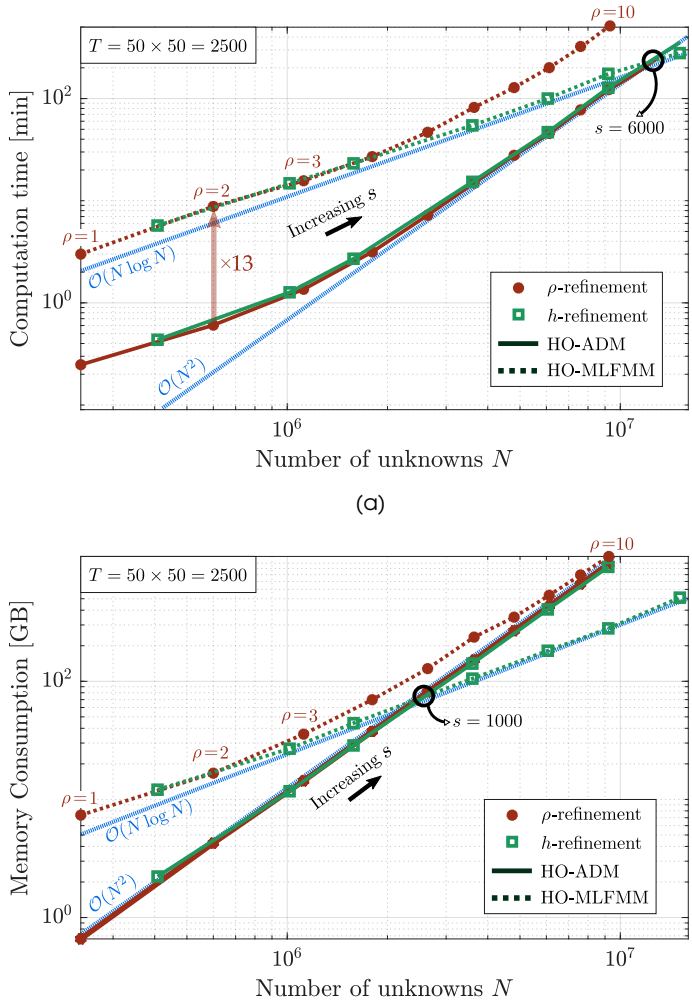

Figure 2.9: Computation time and memory consumption for HO-ADM and HO-MLFMM applied to the array of plates as seen in Figure 2.7 for varying polynomial orders $\rho = \{1, \ldots, 10\}$ and constant mesh as well as for varying mesh sizes with a constant polynomial order of $\rho = 2$. The number of basis functions per array elements, s, is increased by h-refinement (green boxes) or ρ-refinement (red dots).

ing is not critical in practice. Here it should be mentioned that h- and ρ-refinement in the HO-ADM results in a quadratic scaling in both cases, whereas this only happens for HO-MLFMM in case of ρ-refinement for high BF orders.

Focusing on ρ-refinement, we see that for $N < 1$ million the slope of the computation time curves for both HO-ADM and HO-MLFMM are close to the $\mathcal{O}(N \log N)$ asymptote which is expected for MLFMM but not for HO-ADM. This indicates that the quadratic scaling of HO-ADM is not dominating the computation time for smaller problems ($N < 1$ million). In terms of memory consumption, only the HO-MLFMM follows the $\mathcal{O}(N \log N)$ asymptote, whereas HO-ADM scales quadratically. If we focus solely on h-refinement, we see that HO-ADM is around 13 times faster than HO-MLFMM for a total number of unknowns less than 1 million. However, a break-even point can be observed between HO-ADM and HO-MLFMM, both in terms of computation time and memory consumption. In the first case, the break-even point between HO-ADM and MLFMM is around $s = 6000$ BFs on each array element, whereas the break-even point is around $s = 1000$ in terms of memory consumption.

In summary, numerical tests have verified that the combination of HO BFs with the ADM, denoted HO-ADM, leads to more than an order of magnitude lower memory consumption and faster computation times compared to ADM employing traditional first-order basis functions. Furthermore, higher-order convergence has been demonstrated for ADM in combination with hierarchical higher-order basis functions. Lastly, the computation time of HO-ADM is shown to be more than an order of magnitude shorter than HO-MLFMM using practical array element sizes. Lastly, the memory consumption of HO-ADM is four times lower than that of HO-MLFMM for small array elements $s < 100$, and on a par with HO-MLFMM for common array element sizes, i.e. $s \approx 1000$.

2.4 Summary

By combining HO BFs with the ADM, more than an order of magnitude lower memory consumption and shorter computation times can be achieved compared to ADM employing traditional first-order basis functions. As an example, a 40 times reduction in total computation time and a ten times reduction in memory consumption has been shown for a 100-element DRA of conical horns on a laptop resulting in a computation time of five minutes.

HO-convergence has been verified using the HO-ADM for an array of spheres and the use of HO BFs has been shown to provide higher accuracy than first-order BFs for the same number of unknowns. For the same accuracy, it has been shown that employing HO BFs in the HO-ADM reduces the total number of unknowns by a factor of nearly three compared to first-order BFs.

In terms of computation time, the HO-ADM is over 10 times faster than the HO-MLFMM for practical array sizes, with many BFs per element ($s = 1000$). The memory consumption of HO-ADM is four times lower than that of HO-MLFMM for small array elements with $s < 100$ HO BFs per element, and on a par with HO-MLFMM for common array element sizes, comprising $s \approx 1000$ HO BFs per element.

CHAPTER 3

Connected & Sparse Array Antennas

The HO-ADM, presented thus far, is not able to handle conduction currents flowing between array elements. This is a significant limitation since it effectively excludes arrays with a ground plane or other interconnecting features. Moreover, as the HO-ADM requires the d-dimensional array lattice to be fully populated with identical elements, thinned array antennas cannot be analyzed either. In this chapter, we present extensions to the HO-ADM to expand its applicability to connected and/or sparse array antennas.

The first part of this chapter (Section 3.1) briefly discusses the motivation for using thinned array antennas, followed by a presentation of the essential extensions required for their analysis. Hereafter, the performance of the extension to sparse arrays is compared to HO-MLFMM. The second part of this chapter (Section 3.2) presents the necessary extensions to allow for electrically connected elements, emphasizing key preconditioner considerations essential for the practical functionality of HO-ADM. The chapter concludes with various numerical validation examples, demonstrating the practicality and efficiency of these extensions within the HO-ADM framework. The most significant parts of the work in this chapter are presented in papers [J2], [C2] which are found under Publications.

3.1 Extension to Sparse Arrays

Thinned array antennas are sparse arrays obtained by either terminating or removing a substantial number of elements from uniformly spaced arrays [93]. The primary motivation behind array thinning is to reduce cost and weight while maintaining key far-field performance metrics like gain, beamwidth, and side lobe level [94–98]. Moreover, thinning can be driven by spatial constraints, especially in situations where the outer elements of a regular array must be removed to fit within a specific boundary [99–101]. For the remainder of this dissertation, the term “thinning” will specifically

refer to the removal of any number of identical array elements from an array. Here we note that the limitation of identical elements is addressed in Chapter 4.

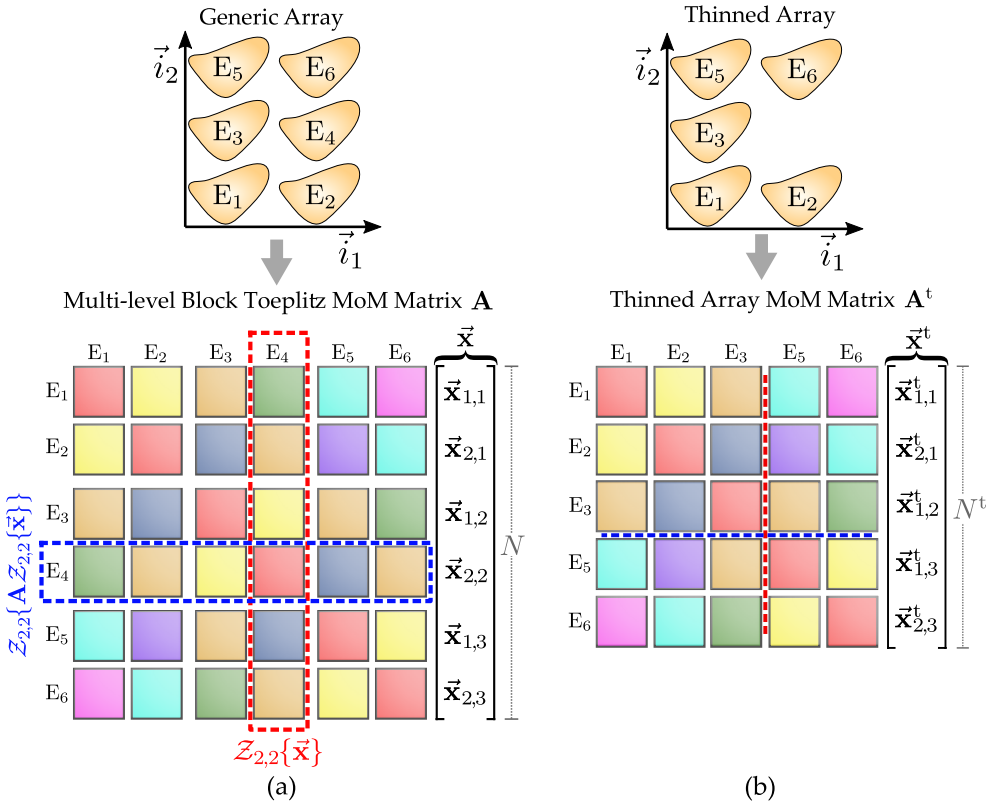

Figure 3.1: Illustration of (a) $T = 2 \times 3 = 6$-element generic array, and the resulting multi-level block Toeplitz MoM matrix $\mathbf{A}$ with $N = sT$ unknowns, (b) $T = 2 \times 3 = 6$-element thinned array and with the corresponding MoM matrix $\mathbf{A}^{\mathrm{t}}$ after removing element four (E_4). The colored blocks indicate similar interaction matrices and the varying padding between blocks is used to indicate the multi-level structure. The dashed rectangles and lines indicate the block-rows and columns removed by thinning.

We take outset in the linear system of equations arising after applying the MoM to the generic $T = 2 \times 3 = 6$-element regular array shown in Figure 3.1 (a)

$$\mathbf{A}\vec{x} = \vec{b}, \tag{3.1}$$

where $\mathbf{A} \in \mathbb{C}^{N \times N}$ is the MoM matrix, $\vec{x} \in \mathbb{C}^{N \times 1}$ is the unknown current coefficients vector, $\vec{b} \in \mathbb{C}^{N \times 1}$ is the excitation vector, and N is the total number of unknowns. As already shown in Section 2.2, the FFT-acceleration of $\mathbf{A}\vec{x}$ is possible iff $\mathbf{A}$ has a

multi-level block-Toeplitz structure, which is only the case for a fully populated array lattice. In case we remove an element from the array, e.g. E_4, we end up with a smaller system of equations

$$\mathbf{A}^{\mathrm{t}}\vec{x}^{\,\mathrm{t}} = \vec{b}^{\,\mathrm{t}}, \tag{3.2}$$

where $\mathbf{A}^{\mathrm{t}} \in \mathbb{C}^{N^{\mathrm{t}}\times N^{\mathrm{t}}}$ is the MoM matrix of the thinned array, $\vec{x}^{\,\mathrm{t}} \in \mathbb{C}^{N^{\mathrm{t}}\times 1}$ is the resulting thinned unknown vector, $\vec{b}^{\,\mathrm{t}} \in \mathbb{C}^{N^{\mathrm{t}}\times 1}$ is the thinned excitation vector, and N^{t} is the total number of unknowns after thinning the array. But, more importantly, the thinned MoM matrix $\mathbf{A}^{\mathrm{t}}$ does not, anymore, possess the MBT property (see Figure 3.1 (b)). In the following, we will explore how to retain an FFT-accelerated MVP, even in the case of thinned arrays.

First, we note that the MoM matrix $\mathbf{A}^{\mathrm{t}}$ of the thinned system is naturally a subset of $\mathbf{A}$, which in turn means that $\mathbf{A}^{\mathrm{t}}$ can be obtained by removing block-rows and block-columns from the original matrix $\mathbf{A}$. Since we would like to keep the MBT property, we cannot explicitly remove rows and columns from $\mathbf{A}$. Thus, we instead zero the unknown vector $\vec{x}$ and the MVP result $\vec{v}$ at appropriate positions to obtain the same effect. Mathematically, imitating the removal of block-columns and block-rows can be conceptualized with the following two steps

$$\begin{aligned} &(1)\ \vec{v} = \mathbf{A}\overbrace{\mathcal{Z}_{a,b}\{\vec{x}\}}^{\vec{u}} && \text{Removes block-column pertaining to element at (a,b)} \\ &(2)\ \vec{y} = \mathcal{Z}_{a,b}\{\vec{v}\} && \text{Removes block-row pertaining to element at (a,b)} \end{aligned}, \tag{3.3}$$

for which $\vec{u} = \mathcal{Z}_{a,b}\{\vec{x}\}$ is a zeroing operator placing zeros at indices in the vector $\vec{x}$ pertaining to the removed array element at position (a, b) in the array lattice[†]. The key point in this first step is that because $\vec{u}$ is of full length N, it can be multiplied on the full MoM matrix $\mathbf{A}$ possessing the MBT property, effectively preserving the FFT-acceleration. As an example, the consequence of multiplying $\mathbf{A}$ with $\mathcal{Z}_{2,2}\{\vec{x}\}$ is that the matrix blocks in column number four is effectively removed as illustrated with the vertical red dashed rectangle in Figure 3.1 (a). From an electromagnetic perspective, this can be interpreted as enforcing zero current-flow on E_4. In addition, the influence caused by the coupling fields from adjacent elements should be removed. Consequently, the second step is to zero the MVP result as well, i.e. $\mathcal{Z}_{2,2}\{\vec{v}\}$. This effectively removes block-row number four as depicted with the horizontal blue dashed rectangle in Figure 3.1 (a). To summarize, the idea is to formulate the MVP for the thinned system in terms of an MVP involving the full system as

$$\mathbf{A}^{\mathrm{t}}\vec{x}^{\,\mathrm{t}} \overset{\text{def.}}{=} \mathcal{Z}_{a,b}\{\mathbf{A}\mathcal{Z}_{a,b}\{\vec{x}\}\}, \tag{3.4}$$

where it is implied that the resulting zero-entries are disregarded. Note that the zero operator $\mathcal{Z}$ is used here for illustrative purposes. In practice, we provide only a

[†]Note that the operator $\mathcal{Z}_{a,b}$ does not require repeated application for each element removal e.g. $\mathcal{Z}_{1,2}\mathcal{Z}_{2,2}\ldots$, as the $\vec{u}$ vector can be pre-configured once with zeros for all elements which should be removed.

selected subset of unknowns to the iterative solver as illustrated in Figure 3.2. The critical aspect is here to ensure that the iterative solver correctly calculates the residual vectors used to build the Krylov subspace for the thinned system. To this end, the residual vectors $\vec{r}^{\,\mathrm{t}}$ are formulated as

$$\vec{r}^{\,\mathrm{t}} = \underbrace{\mathcal{C}^{\downarrow}\{\vec{b}\}}_{\vec{b}^{\,\mathrm{t}}} - \underbrace{\mathcal{C}^{\downarrow}\{\mathbf{A}\mathcal{C}^{\uparrow}\{\vec{x}^{\,\mathrm{t}}\}\}}_{\mathbf{A}^{\mathrm{t}}\vec{x}^{\,\mathrm{t}}}, \tag{3.5}$$

where $\mathcal{C}$ is a specialized copy operator taking the thinned system unknowns $\vec{x}^{\,t}$ and placing them ($\mathcal{C}^{\uparrow}$) at appropriate positions in the full vector, or removing them ($\mathcal{C}^{\downarrow}$).

As seen in Figure 3.2, in each iteration the relevant unknowns are copied from the thinned vector $\vec{x}^{\,\mathrm{t}}$ to the full vector $\vec{u}$ via the $\mathcal{C}^{\uparrow}$ operator. Remark that zeros have already been placed at the positions of the thinned elements prior to the iterative solution phase. Next, the FFT-accelerated MVP $\vec{v} = \mathbf{A}\mathcal{C}^{\uparrow}\{\vec{x}^{\,\mathrm{t}}\}$ is performed, and the result is copied back via $\mathcal{C}^{\downarrow}$ into $\vec{v}^{\,\mathrm{t}}$. In this way, the unknowns pertaining to the removed elements can be thought of as hidden from the iterative solvers perspective, and as a result the iterative solver will converge to the same solution as if the ordinary MVP $\mathbf{A}^{\mathrm{t}}\vec{x}^{\,\mathrm{t}}$ was applied. We note that this concept of hiding unknowns from the iterative solver is not only useful for the analysis of thinned arrays but is also important in allowing electrically connected arrays, which will be evident in the following Section 3.2. Moreover, as discussed in more detail in Chapter 4, since hidden unknowns allow for the removal of selected features of the array element at any desired position in the array lattice, non-identical array elements can be analyzed as well.

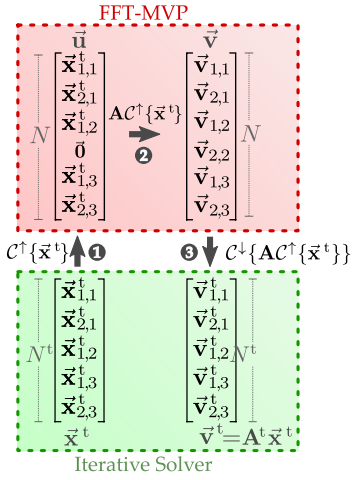

Figure 3.2: Illustration of how the iterative solver performs an FFT-accelerated MVP in each iteration in case of the thinned array in Figure 3.1 (b) by hiding the unknowns pertaining to the removed element number four from the iterative solvers perspective.

An important implication of the outlined approach is that no matter how many elements are removed from a given array, the HO-ADM needs to calculate the circulant generator $\mathbf{C}$ (see Section 2.2) as if it was a fully populated array. In the limiting case where all but one element is removed this incurs a large overhead in terms of both computation time and memory consumption. This suggests that break-even points between HO-ADM and HO-MLFMM exist for given thinning ratios $\frac{T_{\text{ex}}}{T}$ of excluded elements, T_{ex}, to total number of elements, T.

In Figure 3.3, the computation time for HO-ADM and HO-MLFMM as applied to the array configuration in Figure 2.7 is shown for varying levels of thinning as well as for different number of basis functions per array element $s = \{612, 1104, 2112\}$, for an array comprising $T = 20 \times 20 = 400$ elements.

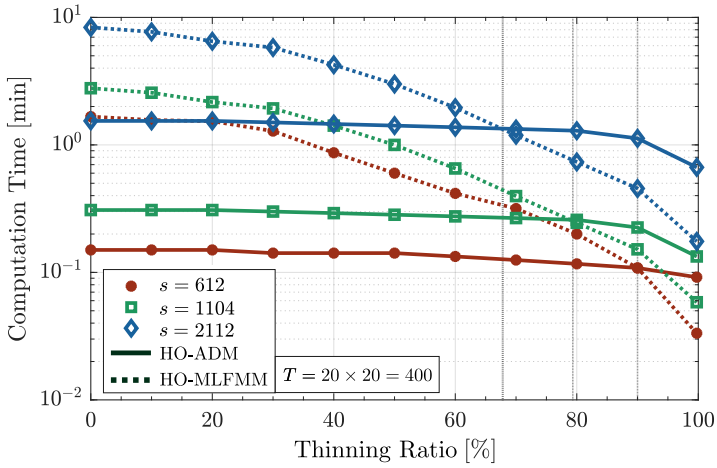

Figure 3.3: Computation time for HO-ADM and HO-MLFMM as applied to the array of plates as seen in Figure 2.7 for varying levels of thinning of the $T = 20 \times 20 = 400$ elements.

For no thinning at all, that is $\frac{T_{\text{ex}}}{T} = 0\,\%$, HO-ADM is 10 times faster than HO-MLFMM with $s = 612$ basis functions per array element, and 6 times faster for $s = 2112$, which is expected based on the results from Section 2.3.3.

As the array is increasingly thinned, the computation time for HO-MLFMM is seen to steadily decrease and eventually converge to the time it takes to do a full MoM of a single element. This is not the case for HO-ADM which has almost constant computation time regardless of the amount of thinning for $\frac{T_{\text{ex}}}{T} < 80\,\%$. For thinning levels above $\frac{T_{\text{ex}}}{T} > 80\,\%$, the computation time of HO-ADM is, however, seen to decrease because the preconditioner gets more effective as an increasingly smaller system is solved. In fact, eventually the employed block-diagonal preconditioner solves the system in a single step. As a result, all HO-ADM curves eventually converge to

the time it takes to do the setup-phase only, i.e. the calculation of the circulant generator.

For $s = 612$ BFs per array element, using HO-ADM is not advantageous compared to HO-MLFMM for thinning levels above $\frac{T_{ex}}{T} > 90\,\%$, beyond which HO-MLFMM is faster than HO-ADM. The threshold at which HO-MLFMM becomes faster than HO-ADM shifts to $\frac{T_{ex}}{T} = 80\,\%$ thinning for $s = 1104$ and further decreases to $\frac{T_{ex}}{T} = 70\,\%$ for $s = 2112$. Following this trend, a first-order extrapolation indicates that for no thinning at all $\frac{T_{ex}}{T} = 0\,\%$, the break-even point would occur for $s \approx 5500$ which corresponds to the break-even point found in Figure 2.9.

The memory consumption is around 4 GB for both HO-ADM and HO-MLFMM for $s = 612$. As such, the break-even point in terms of memory happens already at around $s = 612$ BFs per array element. The main reason is that the memory scaling of HO-ADM scales quadratically in number of basis functions per element, and only linearly in terms of number of array elements T. With an increased number of BFs per element $s = 1104$, the memory consumption for HO-ADM is 13 GB, compared to just 9 GB for HO-MLFMM. Furthermore, for $s = 2112$, the memory consumption for HO-ADM increases to 50 GB, while HO-MLFMM only requires 36 GB.

In summary, by hiding unknowns from the iterative solver, array elements can be excluded from the iterative solution process, thus enabling one to obtain the exact same MoM solution as if those elements did not exist to begin with, while keeping the FFT-accelerated MVP. For a typical number of basis functions per array element ($s \approx 1000$) and thinning no more than 80 % of the array elements, the HO-ADM offers one order of magnitude faster computation time, albeit with a penalty of increased memory consumption compared to HO-MLFMM. Note, however, that arrays are typically thinned between 20 % and 50 % [94,95,102], which means that the HO-ADM is faster than HO-MLFMM for most practical purposes.

3.2 Extension to Electrically Connected Arrays

When array elements become electrically connected, meaning that conduction currents can flow between them, the MoM matrix $\mathbf{A}$ loses its MBT property. This is due to the necessity of associating doublet BF-coefficients on connected edges with either one or the other array element. To address this issue, we have employed the Discontinuous Galerkin Method (DGM) for surface integral equations [103].

3.2.1 Applying Discontinuous Galerkin in HO-ADM

The DGM is widely acknowledged for its efficiency in handling complex structures comprising non-conformal discretizations with mesh elements of a wide range of electrical sizes. This capability leads to a substantial reduction in both memory consumption and computation time as evidenced by several studies such as [104–106]. This dissertation introduces another application of DGM on conformal discretizations, fo-

cusing on preserving the MBT property of the MoM matrix $\mathbf{A}$. We refer the reader to Appendix A.3 for a short introduction to DGM and [103] for more details.

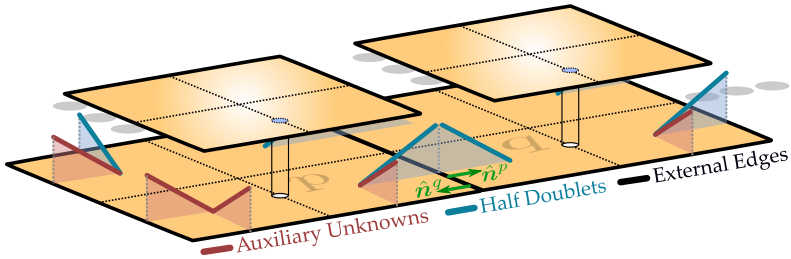

Figure 3.4: Two patch elements at the corner of a larger ground-plane-connected array. Half-doublet BFs are introduced on either side of the boundaries between adjacent elements. Auxiliary unknowns, which are appropriately placed half-doublets, are added on external edges to retain the MoM matrix MBT property.

In essence, the DGM is able to enforce current continuity, in a weak sense[†], between both conformal and non-conformal mesh cells via the addition of an extra surface integral penalty term to the ordinary MoM. This is, however, at the cost of an increased condition number of $\mathbf{A}$. Therefore, the authors of [103] proposed to lower the condition number of the resulting DGM MoM matrix to provide practical iterative convergence, by introducing an extra boundary interior penalty stabilization function $\mathcal{I}_{\mathrm{IP}}(\beta)$

$$\mathcal{I}_{\mathrm{IP}}(\beta) = \frac{\beta}{k^2} \int_{\mathcal{C}_{pq}} [\hat{\boldsymbol{n}}^p \cdot \vec{f}_t^{\,m}(\vec{r})][\hat{\boldsymbol{n}}^q \cdot \vec{f}_b^{\,n}(\vec{r})] d\vec{r}, \tag{3.6}$$

in which $\beta = \frac{1}{10h}$ is a scalar depending on the average electrical mesh size h, $k = \omega\sqrt{\mu_0 \varepsilon_0}$ is the wavenumber with angular frequency ω, and μ_0 and ε_0 are the free space magnetic permeability and electric permittivity, respectively. $\vec{f}_t^{\,m}$ is the m^{th} test function, $\vec{f}_b^{\,n}$ is the n^{th} basis function, and $\vec{r}$ is a position vector along the common edge $\mathcal{C}_{pq}$ between mesh cell p and q with in-plane outward normal unit vectors denoted as $\hat{\boldsymbol{n}}^p$ and $\hat{\boldsymbol{n}}^q$, respectively (see Figure 3.4).

In the HO-ADM, it is crucial to remove this interior boundary penalty term from the formulation because of the opposite directions of the two normal vectors $\hat{\boldsymbol{n}}^{\{p,q\}}$, when evaluated along the common edge $\mathcal{C}_{pq}$. As a result, the BF-coefficients associated with each side are assigned opposite signs and the MBT property of $\mathbf{A}$ is lost. Here, we note that since $\mathcal{I}_{\mathrm{IP}}$ is merely responsible for lowering the condition number, excluding it does not affect current continuity. Moreover, it has recently been shown that its exclusion is feasible, and sometimes optimal, provided that proper

[†]"Weak" continuity means that the basis functions do not inherently (by construction) satisfy current continuity.

preconditioning is employed [105,107,108]. In Section 3.3, a suitable preconditioning strategy is discussed and shown to ensure system stability even for electrically large and connected arrays using HO-ADM.

As an example of how DGM is applied in the HO-ADM, Figure 3.4 shows two patch array elements at the corner of a larger ground-plane-connected array. The usual doublet BFs (full roof-tops) are split into half-doublets (marked with teal color), but only at the edges shared by two quadrilaterals which are located on different array elements. In this way, current continuity is strongly enforced on all edges except those connecting two neighboring elements. Note that the introduction of half-doublets involves some overhead as they increase the total number of unknowns. This is, however, in practice not an issue as described in more detail in [J2, Sec. III.B.3].

The main point of introducing half-doublets and employing the DGM in HO-ADM is that it allows us to distribute the BF-coefficients evenly between array elements. Nevertheless, the described approach introduces a new challenge: the amount and enumeration of BFs will now vary between elements, such as elements at the corners of the array compared to those in the middle. Consequently, the DGM alone is not sufficient to obtain an MBT MoM matrix, hence impeding an FFT-accelerated MVP.

3.2.2 Auxiliary Unknowns

To restore the MBT property of $\mathbf{A}$, we need to make the self-interaction matrices of all array elements equal. To this end, a number N_{aux} of auxiliary BFs must be added to the array elements that are located along the edges of the array, effectively treating them as if they were fully surrounded by neighboring elements. A naïve approach would be to add half-doublets on all edges which are not electrically connected to neighboring elements and therefore are associated with only one mesh cell. This would make self-interaction blocks for all array elements equal and restore the MBT property of $\mathbf{A}$, as discussed in more detail in [J2, Sec. III.B.2]. Nevertheless, minimizing the number of auxiliary BFs is crucial, as the additional unknowns N_{aux} introduce overhead due to the necessity of computing and storing their interactions. Therefore, a better approach has been devised which involves the identification of only strictly necessary edges on which to place auxiliary unknowns (see details in Appendix C.1).

An important implication of adding auxiliary unknowns is that they alter the Krylov subspace and therefore we end up solving a slightly different problem than the intended. It is therefore crucial to omit the auxiliary BF-coefficients from the solution space. To do so, the technique presented in Section 3.1 is applied to hide the auxiliary unknowns from the iterative solvers perspective. As a result, the auxiliary unknowns merely serve to preserve the MBT structure and are never solved for.

In summary, by introducing half-doublets at connected boundaries between array elements (i.e. only on the ground plane for the patch array of Figure 3.4), using the DGM to enforce current continuity and by introducing auxiliary unknowns which are hidden from the iterative solver, electric conduction currents are allowed to flow

between array elements while retaining the MBT property of the MoM matrix, permitting an FFT-accelerated MVP.

3.3 Iterative Solution & Preconditioning

In the HO-ADM, an iterative solution procedure is inevitable because of the inaccessibility of the full MoM matrix $\mathbf{A}$. While a variety of iterative solvers exist, in the following, we focus mainly on the Krylov-subspace-based Generalized Minimum RESidual (GMRES) [109, 110] method which is most frequently selected for its reliable convergence pattern [111]. We note that other solvers such as the BiConjugate Gradient Stabilized (BiCG-STAB) [112] method, Induced Dimension Reduction (IDR(s)) [113] method, and the Symmetric Quasi-Minimal Orthogonal Residual (SQMOR) [114] method have also been considered for HO-ADM. These methods have been implemented and compared to GMRES with the following conclusions:

- BiCG-STAB is more sensitive to high condition numbers than a non-restarted GMRES. The convergence pattern of BiCG-STAB can be erratic, making it difficult to assess whether a solution can be obtained in reasonable time. Nevertheless, when BiCG-STAB converges, it does so at a rate similar to the GMRES.
- IDR(s) can offer as fast a convergence as non-restarted GMRES, but only for small problems $N < 10,000$ and with a proper choice of s. IDR(s) has a much more unstable convergence pattern than BiCG-STAB and the optimal subspace dimension size s cannot be determined a priori.
- SQMOR has a more stable convergence pattern than BiCG-STAB, but less stable than GMRES. It uses only a single MVP per iteration (disregarding the preconditioner), which generally makes it twice as fast as BiCG-STAB. Nonetheless, it only works for complex symmetric matrices and therefore only with the EFIE operator.

BiCG-STAB and SQMOR, as short-recurrence solvers, use constant memory without storing the full Krylov subspace history. However, GMRES was chosen for its more stable convergence characteristics. More specifically, the restarted version of GMRES was chosen for HO-ADM to balance effective memory consumption. This choice, however, necessitates minimizing the number of iterations, which in turn demands a highly effective preconditioning strategy.

The importance of the selected preconditioning method for HO-ADM is further highlighted by its extension with the DGM, which results in a MoM matrix $\mathbf{A}_\mathrm{D} \in \mathbb{C}^{N_\mathrm{D} \times N_\mathrm{D}}$ which has more unknowns N_D than the original matrix $\mathbf{A} \in \mathbb{C}^{N \times N}$. In addition to a larger system, combining HO-ADM with DGM as described in Section 3.2.1 is accompanied by a rise in the condition number. This is mainly due to the now closely coupled half-doublet BFs but also due to the excluded interior stabilization term $\mathcal{I}_\mathrm{IP}$. As an example, an array of $T = 5 \times 5 = 25$ connected PEC-plates with side

length of 1λ, as illustrated in Figure 2.7, is created with an center-to-center distance of 1λ such that conduction currents can flow between the elements. Doing so effectively forms a $(5\lambda)^2$ PEC-plate, which can be simulated as an array using HO-ADM and as a normal plate in the full MoM.

Due to the DGM and auxiliary unknowns in HO-ADM, a total of $N_\mathrm{D} = 5500$ unknowns are needed, whereas $N = 4900$ unknowns are needed in the original MoM matrix $\mathbf{A}$. The resulting eigenvalue distributions of $\mathbf{A}$ and $\mathbf{A}_\mathrm{D}$, as shown in Figure 3.5, are seen to be fairly similar except for a band of near-zero eigenvalues which are introduced in $\mathbf{A}_\mathrm{D}$ by the application of DGM. With normally incident plane-wave excitation, solving the system with and without DGM unknowns requires 253 and 138 iterations, respectively, without using a preconditioner. This is also reflected in the condition number which nearly doubles going from $\mathrm{cond}(\mathbf{A}) = 1050$ to $\mathrm{cond}(\mathbf{A}_\mathrm{D}) = 2050$.

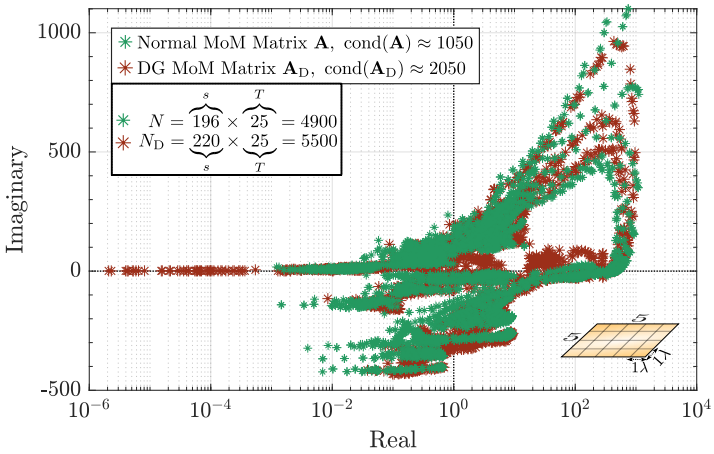

Figure 3.5: Complex eigenvalue distributions for the MoM matrices for HO-ADM ($\mathbf{A}_\mathrm{D}$) and full MoM ($\mathbf{A}$), resulting from the analysis of a $T = 5\lambda \times 5\lambda$ PEC-plate.

To tackle the increased condition number introduced by the extension of HO-ADM with DGM, two different block-diagonal preconditioners have been examined in the following. A left-preconditioned linear system of equations is assumed[†]

$$\mathcal{M}^{-1}\mathbf{A}\vec{x} = \mathcal{M}^{-1}\vec{b} \tag{3.7}$$

in which $\mathcal{M}$ represents a block-diagonal preconditioning matrix, with ($\mathcal{M}_\mathrm{C}$) or without ($\mathcal{M}_\mathrm{NC}$) coupling terms from nearby elements. Note that $\mathcal{M}$ is never formed explicitly, except for illustrative purposes in Figure 3.6 (a), nor applied to $\mathbf{A}$ directly.

[†]Note that the spectra of left, right and split preconditioning is identical, however since different residuals are minimized for the three cases, different convergence is to be expected in practice [115].

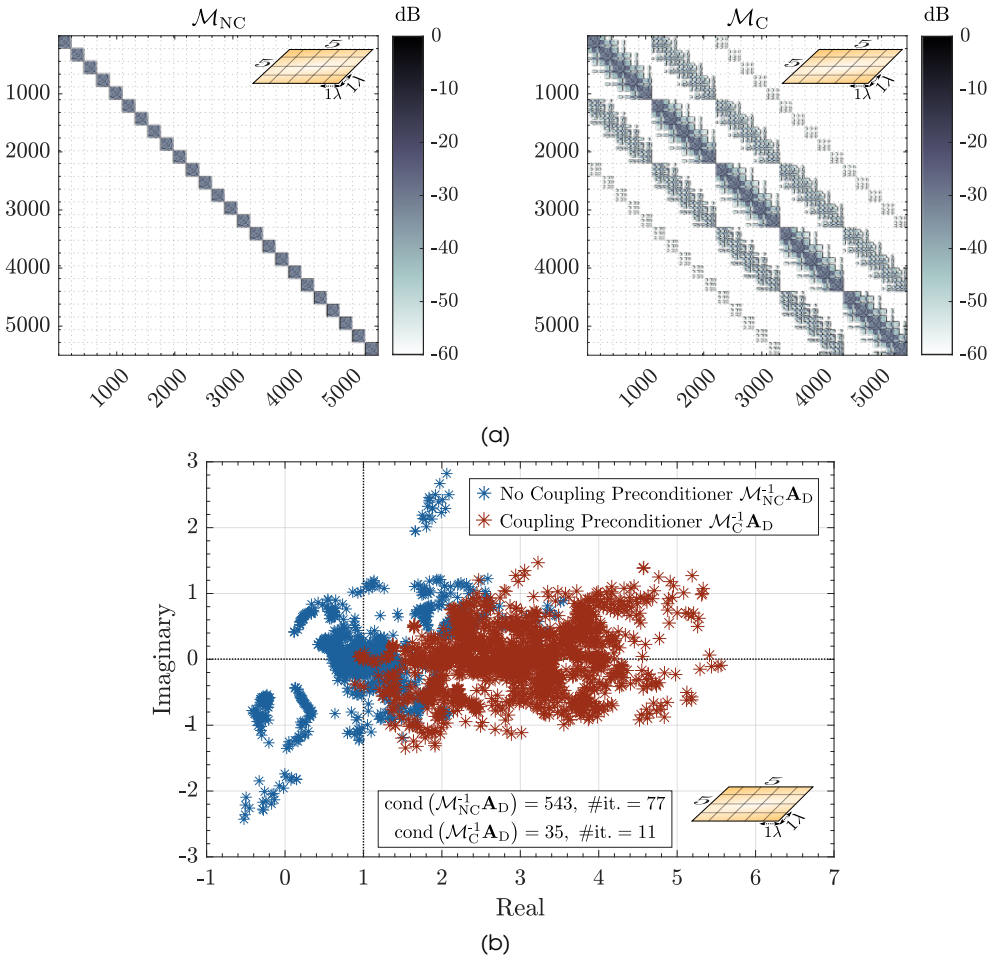

Figure 3.6: (a) Illustration of two block-diagonal preconditioners without ($\mathcal{M}_{\mathrm{NC}}$) or with ($\mathcal{M}_{\mathrm{C}}$) coupling from nearby elements resulting from the analysis of a $T = 5\lambda \times 5\lambda$ PEC-plate. (b) The resulting eigenvalue distributions after applying them to the HO-ADM MoM matrix $\mathbf{A}_{\mathrm{D}}$.

Due to the inherent MBT structure of $\mathbf{A}$ for a regular array, a constant-memory block-diagonal preconditioner without coupling ($\mathcal{M}_{\mathrm{NC}}$), as illustrated in Figure 3.6 (a), has been shown to be highly effective for the ADM [69]. It is most efficiently constructed via an LU-factorization of the interaction matrix for a single array element and applied to a vector via backward/forward substitutions.

However, in the case of connected arrays in the HO-ADM, a preconditioner without near-field (NF) coupling no longer suffices. This is evident from Figure 3.6 (b) in which the eigenvalue distributions are shown after applying both $\mathcal{M}_{\mathrm{NC}}$ and $\mathcal{M}_{\mathrm{C}}$ to

the HO-ADM DGM MoM matrix $\mathbf{A}_{\mathrm{D}}$. We see, that although $\mathcal{M}_{\mathrm{NC}}$ effectively lowers the condition number by a factor of four, going from 2050 to 543, there are still eigenvalues with real part close to zero, and even eigenvalues in the left-half plane. By, instead, applying $\mathcal{M}_{\mathrm{C}}$, the eigenvalues are seen to be strictly away from zero. Notably, $\mathcal{M}_{\mathrm{C}}$ is able to lower the condition number by almost a factor of 60, making it possible to solve the $(5\lambda)^2$ PEC-plate problem using GMRES in 11 iterations for a normally incident plane-wave excitation[†].

The efficacy of $\mathcal{M}_{\mathrm{C}}$ using the HO-ADM for larger PEC-plates is exemplified in Figure 3.7, where the relative residual error ϵ, as defined in [J2, Sec.III.C], is plotted versus the number of iterations for square plates with electrical sizes ranging from $(10\lambda)^2$ to $(400\lambda)^2$.

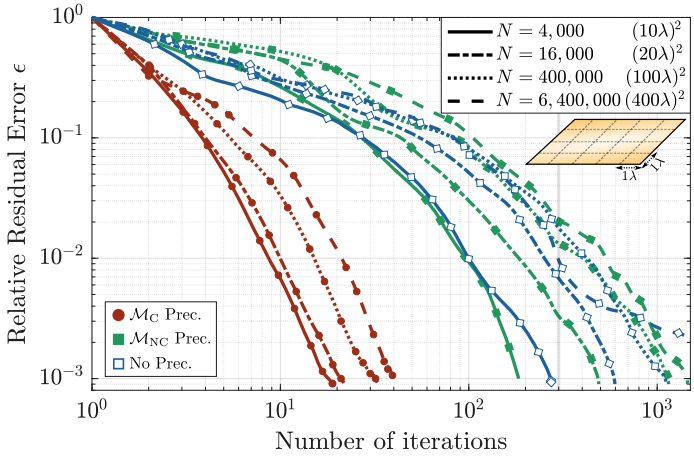

Figure 3.7: Performance of the constant memory near-field (CNF) preconditioner $\mathcal{M}_{\mathrm{C}}$ compared to the common block-diagonal preconditioner $\mathcal{M}_{\mathrm{NC}}$. Both are applied to the case of a normally incident plane wave on variously sized PEC square plates which are constructed by electrically connecting $(1\lambda)^2$ quadrilateral mesh cells using HO-ADM.

The key takeaway from the data presented in Figure 3.7 is the comparative efficiency of the two preconditioners for a $(400\lambda)^2$-PEC plate with 6.4 million unknowns. Whereas the $\mathcal{M}_{\mathrm{NC}}$ achieves a residual error of 10^{-3} after 1448 iterations, the NF-coupling preconditioner $\mathcal{M}_{\mathrm{C}}$ reaches the same level of accuracy in just 41 iterations. We note that the efficacy of $\mathcal{M}_{\mathrm{C}}$ extends beyond the presented examples. For an in-depth analysis of these results, readers are directed to [J2, Sec.III.C.1].

In terms of memory usage, a general challenge with NF-coupling preconditioners is that each block (including coupling terms) along the main diagonal has to be stored.

[†]We note that the effectiveness of the preconditioner $\mathcal{M}_{\mathrm{C}}$, depends on the range of coupling terms considered for each array element. For the HO-ADM, extending the inclusion beyond immediate neighboring quads shows little improvement in convergence, hence only BFs on mesh cells with a shared edge with neighboring elements are included in $\mathcal{M}_{\mathrm{C}}$.

For the HO-ADM, doing so would mean that the preconditioner memory consumption would become proportional to the number of array elements T and even comparable to the storage of the circulant generator $\mathbf{C}$ (see Section 2.2). Therefore, in order to avoid almost doubling the required memory usage of HO-ADM, a constant-memory NF (CNF) coupling preconditioner has been devised, based on the fact that many of the preconditioner groups become redundant for connected regular arrays as depicted in Fig. 4 of [J2]. As a result, for a non-thinned array, we have only nine unique preconditioner groups to calculate and store, whereas we have a finite but slightly larger set of 16 unique preconditioner groups for thinned arrays. The important point is here that it is possible to construct a CNF preconditioner $\mathcal{M}_C$ for simultaneously connected and thinned arrays, by only building and storing at most 16 unique interaction matrices. Remark, in addition, that building the preconditioner groups does not require additional computation of matrix blocks, since this information is already contained within the Toeplitz storage format (the circulant generator $\mathbf{C}$). In order to take advantage of this, we provide in Appendix C.2 the formulas for the required mapping $\mathbf{A}(p,q) \rightarrow \mathbf{C}(m,n,k,l)$ from global MoM matrix row p and column q to circulant generator indices (m,n,k,l).

In summary, by introducing half-doublets at connected boundaries between array elements, using the DGM to enforce current continuity and by introducing auxiliary unknowns which are hidden from the iterative solver, electric conduction currents are allowed to flow between array elements while retaining the MBT property of the MoM matrix, permitting an FFT-accelerated MVP. Although this DGM strategy enables an FFT-accelerated MVP, the iterative solution does not converge in a reasonable number of iterations without introducing the NF-coupling preconditioner $\mathcal{M}_{\mathrm{C}}$. Last but not least, the identification of a constant memory construction of $\mathcal{M}_{\mathrm{C}}$ makes the extension to connected and sparse arrays feasible in practice.

3.4 Numerical Test Cases for Connected Sparse Arrays

To validate the efficiency of the extended HO-ADM, we first revisit the scattering from a PEC plate and compare the scattered field to that of a full MoM. Next, we examine the optimal mesh-size in HO-ADM when applied to a plate of fixed size but with a varying number of array elements. Lastly, we consider a high-gain 32×32 all-metal antenna array based on the design from [77] and showcase the achieved temporal efficiency of using the HO-ADM compared to HO-MLFMM. In this section an equivalent relative error measure, ϵ_{ERE}, as defined in [J2, Sec. IV], is used to compare the fields calculated using HO-ADM and HO-MLFMM.

3.4.1 Plane Wave Incidence on Square PEC Plate

To validate the accuracy of HO-ADM, we have considered a plane wave obliquely incident ($\theta_i = 30°, \phi_i = 0°$) on a square $(40\lambda)^2$-sized PEC plate, as depicted in Fig. 6

of [J2]. Therein, the scattered far field calculated with HO-ADM is also plotted, and it is seen to coincide with the results of the HO full MoM solution within the full dynamic range of 50 dB with an equivalent relative error of $\epsilon_{\mathrm{ERE}} = 0.01\,\%$. We note that even better accuracy could have been obtained by choosing a stricter relative error tolerance than 10^{-3} for the iterative solver.

To validate the computational efficiency of HO-ADM, the total computation time and memory consumption have been recorded and plotted in Fig. 7 of [J2], comparing HO-MLFMM and the HO-ADM for increasingly larger plates[†] ranging from $(10\lambda)^2$ to $(620\lambda)^2$. The main conclusion from these simulations is that for a $(620\lambda)^2$ PEC-plate, the HO-ADM solves for the induced currents using $N = 15,376,000$ unknowns in 6 min with a memory consumption of 18 GB, whereas HO-MLFMM uses $N = 12,300,800$ unknowns, 177 min and 90 GB of memory. Consequently, the HO-ADM achieves almost a factor of 30 faster computation time and 5 times less memory consumption, even though it uses more than three million (25 %) more unknowns than HO-MLFMM. The reader is referred to [J2, Sec. IV.A.] for more details.

The above mentioned results were obtained by modeling the plates using multiple array elements, each with size $(1\lambda)^2$. This choice of a side length $L = 1\lambda$ is based on the findings presented in Figure 3.8. Herein, the computation time for the HO-ADM is illustrated for a normally incident plane wave impinging on a PEC plate of a constant size $(320\lambda)^2$, but where the array element side lengths range from $L = 0.1\lambda$ to $L = 5\lambda$. From the perspective of HO-MLFMM, which uses around 45 min to solve this problem, there is no notable difference in terms of computation time whether a side length of $L = 5\lambda$ or $L = 0.1\lambda$ is used to model the $(320\lambda)^2$-plate. However, because

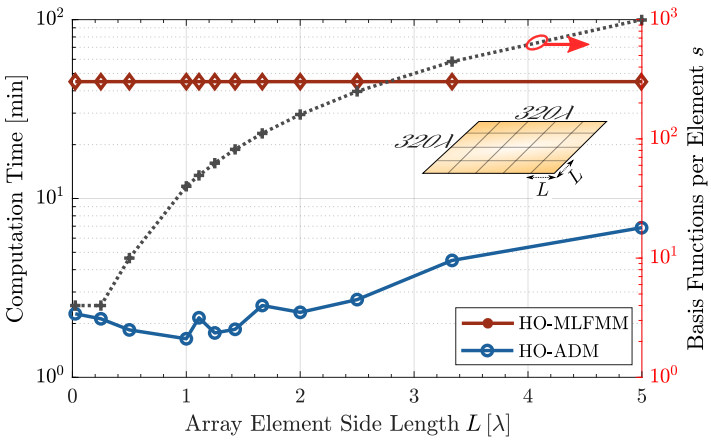

Figure 3.8: Computation time used in HO-ADM for a normally incident plane-wave on a PEC-plate of fixed size $320\lambda \times 320\lambda$ but varying array element sizes with side lengths between $L = 0.1\lambda$ and $L = 5\lambda$.

[†]Note that the frequency is fixed, and the physical size is varied.

of the computational complexity ($\mathcal{O}(s^2 T \log T)$) of HO-ADM, the computation time is expected to vary as variously sized array elements require different number of BFs per array element, s, as well as a varying number of array elements T.

For HO-ADM, in the scenario of array elements of decreasing electrical sizes, it suffices to use less BFs per array element (s becomes small) to represent the surface current density. However, to keep the fixed size of the plate at 320λ, more array elements are needed (T becomes large). In this scenario, it is expected that HO-ADM will perform better the smaller the array elements become, which is seen to be the case for array element side lengths going from $L = 5\lambda$ down to $L = 1\lambda$. Nevertheless, as the array elements become smaller than $L = 1\lambda$, the computation time is seen to increase, although the number of BFs per element, s, decreases. The primary reason for this increase is the need for more Green's function evaluations, which arises from the growing number of mesh cells incorporating BFs of progressively lower orders. In the HO-ADM, it is therefore of interest to keep the mesh cell size as small as possible (due to s^2 scaling), but preferably not smaller than $L = 1\lambda$. This holds true also for cases other than that of a PEC plate.

3.4.2 All-Metal Dual-Band Phased Patch Antenna Array

In this section, we examine a 32×32-element dual-frequency RHCP high-gain antenna array based on the design in [77]. The real-world fabricated array is shown in Figure 2.1 (d). To showcase the thinning extension of HO-ADM, we also examine the same array but thinned to conform to a circular rim as depicted in Figure 3.9 (b), resulting in 793 array elements corresponding to a thinning percentage of 22.6 %. The array elements are excited by wires, as indicated with light blue color in Figure 3.9 (a). The meshing of the full 32×32 array consists of 122,880 mesh cells, leading to around $N = 975{,}000$ unknowns in the HO-MLFMM method and around 1 M unknowns in the HO-ADM due to the inclusion of DGM and auxiliary unknowns, as detailed in Section 3.2.1. For the thinned array, the HO-MLFMM uses $N = 755{,}370$ unknowns, whereas 18,312 (2.4 %) additional unknowns are needed in the HO-ADM.

The far-field radiation patterns for both arrays are evaluated at 8.425 GHz as depicted in Figure 3.10. The peak directivity for the full array is calculated to be 38.44 dBi for both HO-ADM and HO-MLFMM, which is similar to the 38.5 dBi directivity reported in [77]. Moreover, the calculated co- and cross-polarization patterns for both HO-ADM and HO-MLFMM are seen to be nearly identical, with relative errors of 0.03 % and 0.05 % for co-pol and cross-pol, respectively. The radiated far-field pattern for the thinned array in Figure 3.10 (b) shows a relative error of 0.05 % and 0.07 % for co-pol and cross-pol, respectively. The peak-directivity is 1.1 dB smaller at 37.3 dB for the thinned array, and the first side-lobe level at 19.9 dB is close to what would be expected from a uniformly excited circular aperture. The 3 dB-beamwidth is only 0.2° larger for the thinned array compared to the full 32×32 array. A comparison of computation time and memory consumption for HO-ADM and HO-MLFMM is presented in Table 3.1 for both the thinned and full 32×32 array. For the full

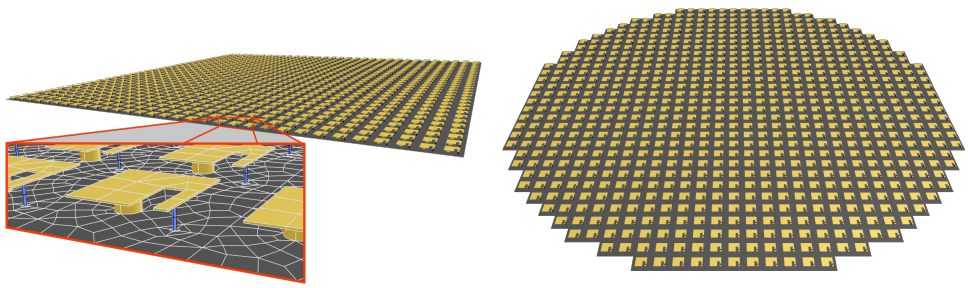

(a) (b)

Figure 3.9: (a) 32×32-element dual-band right-hand circularly polarized all-metal antenna array, including employed meshing of the element cell. (b) Thinned 793-element all-metal array conforming to a circular rim.

array, the HO-MLFMM takes about 1 hour and uses 25.1 GB of memory, whereas the HO-ADM reduces the computation time to approximately 6 minutes at the cost of a slight increase in memory consumption. Notably, both methods use about half of the total computation time in their respective setup-phases and both use roughly the same number of iterations to reach a relative error of 10^{-3}. Consequently, the ten-fold reduction in computation time for HO-ADM stems not only from a 10 times faster setup-phase, but also a 10 times faster MVP evaluation.

Method	Total Simulation Time	Memory Consumption	Number of Iterations	Time per Iteration
HO-MoM	N/A	3540 GB	N/A	N/A
HO-MLFMM	**1 h 2 min**	25.1 GB	540	3.9 s
	(57 min)	(22.5 GB)	(567)	(3.8 s)
HO-ADM	**6 min 18 s**	28.2 GB	481	0.4 s
	(6 min 18 s)	(28.2 GB)	(506)	(0.38 s)

Table 3.1: Total computation time and memory consumption for the 32×32 array in Figure 3.9 (a) and the corresponding circular-thinned array in Figure 3.9 (b), comparing HO-MLFMM and HO-ADM. Results in parentheses are for the thinned array.

In case of the thinned array the HO-MLFMM uses slightly less time 57 min, whereas the total computation time for the HO-ADM in case of the thinned array is unaltered at 6 min and 18 s. It is worth noting that the HO-ADM use the same memory for thinned arrays as if they were fully populated (as discussed in Section 3.1), whereas HO-MLFMM uses nearly 6 GB less memory in the thinned case.

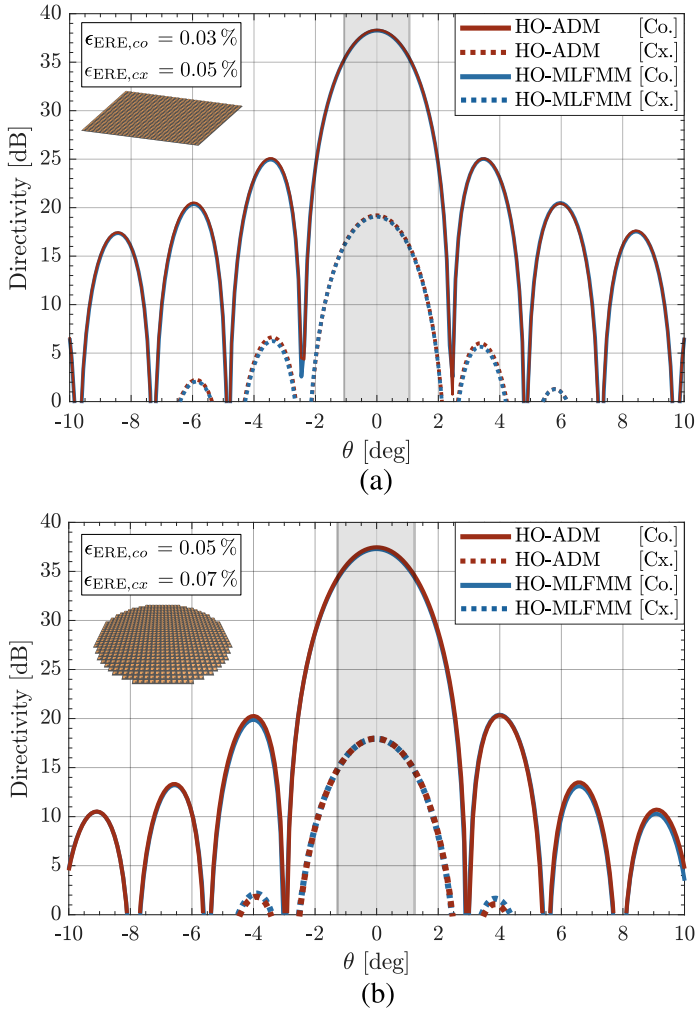

Figure 3.10: Far-field directivity patterns ($\phi = 0°$-cut) at 8.425 GHz comparing the HO-ADM to the HO-MLFMM for (a) the antenna of Figure 3.9 (a) and (b) the thinned array of Figure 3.9 (b). Co-polarization is RHCP whereas the cross-polarization is LHCP. 3 dB-beamwidths are marked with dark-gray bands. The thinned array is 22.6 % thinned. The same correspondence is seen for $\phi = 45°$ and $\phi = 90°$ cuts.

3.5 Summary

The HO-ADM has been extended to allow for the analysis of sparse array antennas by using a technique to implicitly keep the MoM matrix for the fully populated array

and by using a constrained Krylov subspace in the iterative solver. For a typical number of HO BFs per array element ($s \approx 1000$) and a typical thinning ratio of 40 %, the HO-ADM offers one order of magnitude faster computation time albeit with a modest penalty of increased memory consumption, compared to HO-MLFMM.

In addition, the HO-ADM has been extended to analyze arrays with electric conduction currents between elements by introducing half-doublets at connected boundaries, using the Discontinuous Galerkin Method (DGM) to enforce current continuity and by introducing auxiliary unknowns to retain the MBT property of the MoM matrix, permitting an FFT-accelerated MVP. This approach significantly increases the condition number of the MoM matrix, rendering the conventional block-diagonal preconditioner $\mathcal{M}_{NC}$ ineffective. Instead, a near-field coupling preconditioner $\mathcal{M}_C$ has been constructed and applied in the HO-ADM, which for a numerical test case with six million unknowns reduced the number of iterations from 1448 to 41. More importantly, the identification of a constant-memory construction of the near-field preconditioner $\mathcal{M}_C$ is what makes the extension to connected and sparse arrays feasible in practice.

Numerical tests confirmed the efficacy and accuracy of the proposed extensions for a $32 \times 32 = 1024$-element all-metal antenna array designed for the Europa Lander mission, which has been analyzed on a laptop within six minutes with one million unknowns. For this case, the HO-ADM showcased a tenfold reduction in computation time and a comparable memory consumption in comparison with HO-MLFMM.

CHAPTER 4

Non-Identical & Non-All-Metal Arrays

Up to this point, we have demonstrated that the combination of HO BFs with the ADM (HO-ADM) enables fast and accurate analysis of both fully populated regular (Chapter 2), connected, and sparse arrays (Chapter 3). In this chapter, we extend the versatility of HO-ADM by enabling the analysis of arrays with non-identical elements and arrays which are not made entirely of metal.

The first part of this chapter (Section 4.1) begins with a concise overview of the applications of arrays comprising non-identical elements. Subsequently, it details the required modifications to the HO-ADM, facilitating their analysis. With these extensions at hand, the efficiency and accuracy is verified via a selection of numerical examples. The second part of this chapter (Section 4.2) examines how the HO-ADM is adapted to arrays with structures of finite thickness and non-metallic boundaries, outlining the required modifications and exploring their implications on the method's performance and applicability.

4.1 Extension to Non-Identical Elements

In electromagnetics, arrays utilizing non-identical elements have practical applications across various domains. Examples include transmitarrays [116–119], reflectarrays [120,121], meta-surfaces [122,123], and even non-identical frequency selective surfaces [124]. In addition, amplitude-tapering has been achieved using non-identical elements [125, 126], and sequentially-rotated-element arrays [127–130] can also be considered as arrays with non-identical elements. These diverse applications of non-identical elements in electromagnetic array design emphasizes the need to extend the HO-ADM to accommodate such arrays.

The primary reason that HO-ADM is not able to handle non-identical elements stems from the requirement of the MoM matrix to be block-Toeplitz, which in turn necessitates identical self-interaction matrices for all elements. Moreover, because the calculation of these interactions is inherently based on the relative local coordinate

systems of the involved mesh cells, all array elements must be of the same size, shape, and orientation.

4.1.1 The Super Unit Cell

To address this challenge, a strategy must be devised that maintains the appearance of identical elements from the vantage point of the MoM matrix in HO-ADM, while simultaneously yielding the solution of a non-identical array. The key concept introduced to achieve this, as published in [C3], is the "Super Unit Cell" (SUC) which is illustrated for two different examples of non-identical arrays in Figure 4.1. In the following, we outline the steps required to develop and apply the SUC to simulate non-identical arrays within the HO-ADM framework.

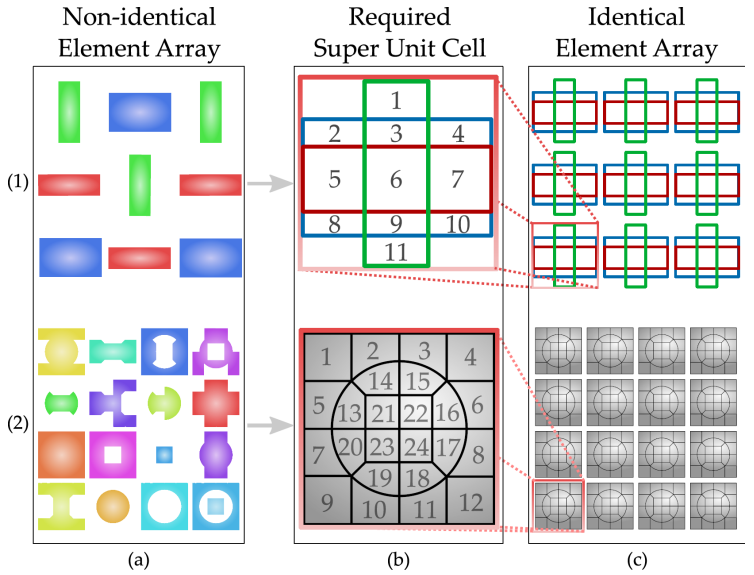

Figure 4.1: (a) Illustration of (1) a 3×3 array of rectangular patches of different sizes and orientations and (2) a 4×4 array of arbitrary elements. (b) The required super unit cells in the HO-ADM for the two non-identical arrays. (c) The corresponding arrays of identical elements with mesh regions which can be removed to transform each element to that of the original non-identical element arrays.

First, we take outset in the array of $3 \times 3 = 9$ non-identical rectangular elements, as depicted in Figure 4.1 (1a) which comprises $T_{\mathrm{NI}} = 3$ distinctly different elements[†], each differentiated by color. The first step is now to superimpose the outlines of the

[†]Note that it can also be viewed as an array with only two distinct elements, because one type of elements can be seen as a rotated version of the other.

three distinct array elements on top of each other[‡] as illustrated in Figure 4.1 (1c), yielding in this case 11 individual regions which together form what will be denoted the SUC. The fundamental idea is now to replace the original elements in the array with the SUC, thereby converting it into an array of $3 \times 3 = 9$ identical elements suitable for analysis using the HO-ADM.

For the array in Figure 4.1 (1a), a SUC with 11 distinct meshing-regions can be constructed as shown in Figure 4.1 (1b), and if we assume, for now, that we can selectively omit various regions from this SUC, we can effectively model non-identical elements. For instance, the green central element of the array can be realized by removing regions $\{2, 4, 5, 7, 8, 10\}$ from the SUC. Similarly, its red rotated counterpart can be realized by excluding regions $\{1, 2, 3, 4, 8, 9, 10, 11\}$. We note that the $4\times4 = 16$ element non-identical array in Figure 4.1 (2a) demonstrates that SUCs, only slightly more advanced than that for the array in Figure 4.1 (1a), are capable of simulating a broad range of diverse array elements.

The second step involves determining whether the initial regions of the SUC should be further discretized according to their respective electrical sizes and/or based on the maximum permissible mesh length. It also involves adapting the mesh to accommodate any excitation structures. Consequently, the initial regions constitute the coarsest possible meshing of the SUC. We note here, that if the non-identical elements in a given array are rather similar in size (as is often the case with reflectarrays), even the coarsest SUC configuration will encompass numerous regions with small electrical sizes. This scenario unavoidably leads to an increased number of unknowns as the similarity between array elements increases. Consequently, the extension of HO-ADM to non-identical elements will be more efficient the larger the dissimilarity between the non-identical elements is[†]. Nevertheless, as will be discussed in the subsequent section, for practical array cases with not too many distinct elements, HO-ADM demonstrates superior computation times compared to HO-MLFMM.

Up to this point, we have assumed that any desired number of regions can be excluded from the SUC at any position in the array lattice. In practice, this exclusion is achieved via manipulation of the MVP by hiding unknowns from the perspective of the iterative solver, using the technique of Section 3.1. More specifically, to remove a SUC-region we need to hide all the singletons and all the doublets (roof-top BFs) that have support in the removed region. An example array element is shown in Figure 4.2 (a), which is generated from the SUC in Figure 4.1 (1b). To remove SUC-regions $\{2, 4, 8, 10\}$, the singleton BFs which have support only within the removed region need to be hidden. Moreover, the full roof-tops which is connected to these regions should be hidden, effectively enforcing no current to flow across the associated edges. Note that this technique allows to exclude any number of regions from each

[‡]Superimposing outlines of elements is equivalent to performing a mathematical union operation on the boundaries of the unique elements in the array.

[†]It should be noted that there is the possibility that some of the regions become so small that dense discretization break-down occurs [131], giving rise to a high condition number in the associated MoM matrix, which could make the problem unsolvable with HO-ADM.

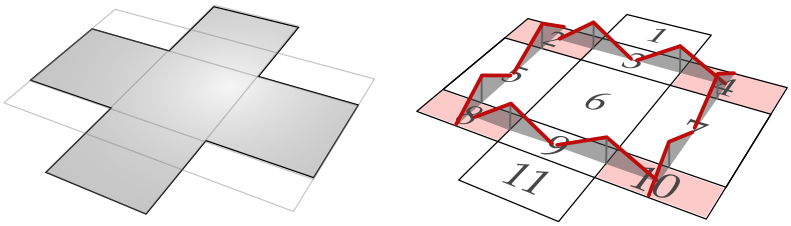

(a) Array Element (b) Doublets to be excluded

Figure 4.2: (a) Illustration of a possible realizable array element from Figure 4.1 (1b) with its corresponding SUC (in light-gray). (b) The edges on which doublet BFs (full roof-top BFs) need to be removed from the SUC to realize that element.

array element, regardless of its position in the array, effectively allowing non-identical elements to be analyzed as if it was an identical-element array in the HO-ADM.

In summary, non-identical elements are in the HO-ADM made possible through the following three steps:

1. **Union of element outlines:** The outlines of the T_{NI} distinct elements of a given array are superimposed to form a SUC which can be placed at all array positions. Regions can be removed from the SUC at any position in the array to model the elements of the original array.

2. **Meshing of SUC:** The regions of the SUC are further discretized because they often exceed the maximum permissible electrical size. This step also involves adapting the mesh to accommodate any excitation structures.

3. **Identification of Hidden Unknowns:** For each of the T array elements, the unknowns pertaining to edges across which current should no longer flow is identified and hidden from the iterative solver, using the technique of Section 3.1.

After completing the initial three steps, the circulant generator $\mathbf{C}$ is computed for an array of SUCs. Because the non-identical array is realized through hiding unknowns in the iterative solution process, there is no need to recompute the circulant generator for different configurations of non-identical elements which are compatible with the given SUC. As such, the circulant generator can, in the case of non-identical elements, be considered as a database of non-identical elements, which can be put at any position in the array and simulated without recalculating $\mathbf{C}$. Based on numerous empirical tests, HO-ADM generally requires equal amount of time for both the setup phase and the iterative solution process, which in turn means that utilizing the database to simulate various non-identical element configurations can lead to a speed-up of approximately a factor of two.

4.1.2 Numerical Test Cases with Non-Identical Elements

In this section we present two numerical examples showcasing the capabilities of HO-ADM after its extension to arrays with non-identical elements. The first example is a 37-element thinned patch array on a 7×7 square lattice with extended ground plane, which necessitates all the techniques presented in Chapter 2, Chapter 3 and Section 4.1.1. The second example is a non-identical element patch array with $8 \times 128 = 1024$ elements, which employs space-tapering to reduce the first side-lobe level (FSLL). The subsequent numerical tests have been carried out on a laptop with specifications as outlined in Table E.1. The GMRES iterative solver is used with a relative residual error tolerance of 10^{-3} and a Krylov subspace maximum dimension of 500[†].

A) Thinned Patch Array with Extended ground plane

Figure 4.3 (a) shows a 37-element linearly polarized patch antenna array which has been thinned to conform to a circular rim. In addition, the ground plane has been extended beyond the bounds of the array elements, which from the perspective of HO-ADM necessitates a non-identical element analysis.

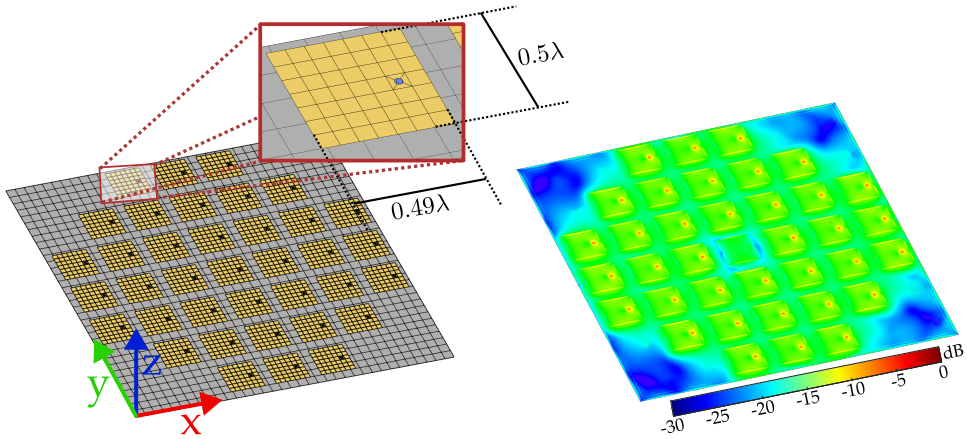

Figure 4.3: (a) Illustration of a thinned 37-element linearly polarized patch antenna on a 7×7 lattice, including main dimensions and wire-excitation feed-points. The center element is not excited. The illustrated coordinate system is employed for the far-field pattern evaluation for which ($\theta = 90°, \phi = 0°$) corresponds to the positive x-axis. (b) The resulting normalized total surface current density calculated using HO-ADM. — Note that the shown discretization is not the simulation mesh.

[†]Note that a relatively large Krylov subspace dimension is employed because the preconditioner $\mathcal{M}_C$ is less effective in the case of non-identical elements.

The array is excited by 36 independent wire excitations operating at 14 GHz, as the center element is left unexcited for illustration purposes. The resulting normalized total surface current density, as calculated with the HO-ADM, is shown in Figure 4.3 (b). We note that because the wire excitations require holes in the radiating patches as well as in the ground plane, the associated SUC has been meshed with extra quadrilaterals at those ends of the wires which are connected to the ground plane.

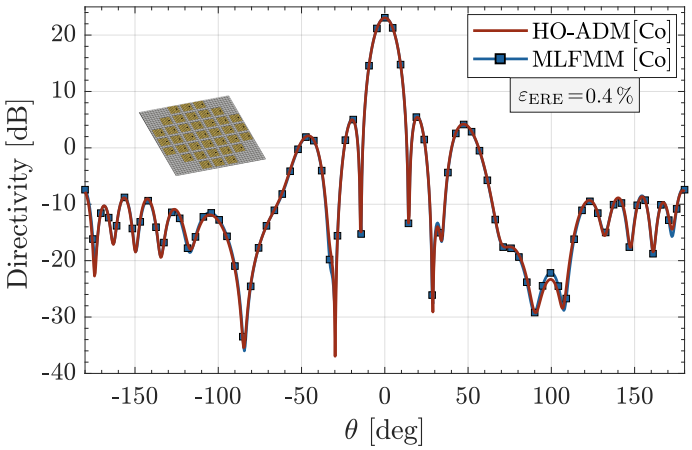

(a) E-plane ($\phi = 0°$)

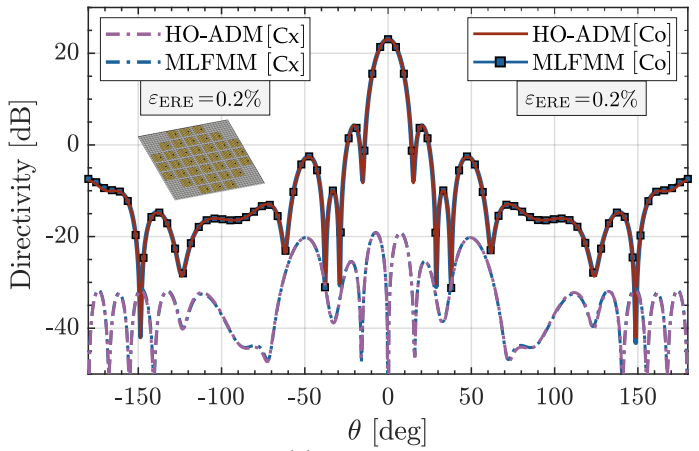

(b) H-plane ($\phi = 90°$)

Figure 4.4: Far-field co- and cross-pol directivity patterns at 14 GHz comparing HO-ADM to HO-MLFMM for the 37-element patch antenna array of Figure 4.3. (a) E-plane patterns ($\phi = 0°$) (b) H-plane patterns ($\phi = 90°$). The cross-pol field level in the E-plane is below -70 dB.

In this way, current continuity can be enforced on the extended ground plane while still allowing holes in the ground plane for the excited patches.

The array is meshed with 3,260 quadrilateral mesh cells, resulting in 57,027 unknowns for HO-MLFMM and 67,522 unknowns for HO-ADM, which corresponds to $s = 1378$ BFs per array element. For this relatively small case, the total computation time for HO-MLFMM is around 1 minute whereas HO-ADM uses 4 seconds, achieving more than an order of magnitude speed increase[†].

Figure 4.4 shows the co- and cross-polarization far-field patterns ($\phi = 0°$ and $\phi = 90°$ cuts) for both HO-ADM and HO-MLFMM. Both methods report a peak directivity of 23.1 dB and a first side-lobe level (FSLL) of -18 dB for the array. The patterns from HO-ADM and HO-MLFMM show excellent agreement in both the E- and H-plane.

B) Non-Identical 1024-element Patch Antenna

Next, we examine an 8×128-element linearly polarized patch antenna array, as shown in Figure 4.5, with 1024 independent wire excitations operating at 1.75 GHz. This array consists of 128 linear 8×1-element arrays with non-identical, space-tapered elements designed to achieve amplitude tapering in the E-plane, thereby reducing the FSLL. We note that this 2D array is an adaptation of the 1D array described in [125],

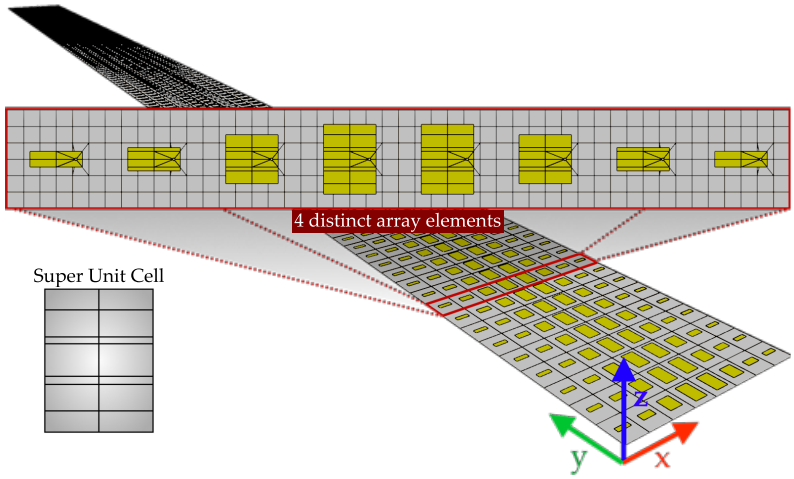

Figure 4.5: 8×128-element linearly polarized patch antenna, including illustration of employed meshing for the reported results of a single space-tapered row. The illustrated coordinate system is employed for the far-field evaluation in which ($\theta = 90°, \phi = 0°$) corresponds to the positive x-axis. © 2023 IEEE

[†]Because HO-ADM uses seconds to do full-wave simulations of small arrays $T < 100$, it can allow for full-wave optimization with thousands of evaluations in reasonable time.

and that each 1D array consists of four distinct elements, which results in the SUC as depicted in Figure 4.5.

The entire structure is meshed with 55,296 quadrilateral cells, resulting in 440,736 unknowns for HO-MLFMM and 507,904 unknowns for HO-ADM. The higher number of unknowns in HO-ADM is due to the specific meshing of the unit cell (as detailed in Section 4.1) and the incorporation of DGM-unknowns (explained in Section 3.2). Despite the approximately 15 % increase in the number of unknowns with HO-ADM (see Table 4.1), the total computation time is reduced from 29 minutes with HO-MLFMM to 3 minutes with HO-ADM, achieving a tenfold speed increase. The speedup is even greater for the MVP alone which is reduced from 4.9 s to 0.3 s per iteration (a factor of 16).

Method	Total Simulation Time	Memory Consumption	Number of Iterations	Time per Iteration
HO-MoM	N/A	1443 GB	N/A	N/A
HO-MLFMM	29 min	7.2 GB	223	4.9 s
HO-ADM	3 min	7.9 GB	441	0.3 s

Table 4.1: Total solution time and memory consumption for the 8×128 array in Figure 4.5, comparing HO-MLFMM and HO-ADM.

Figure 4.6 presents the co- and cross-pol far-field patterns ($\phi = 0°$ and $\phi = 90°$ cuts) for both HO-ADM and HO-MLFMM. Both methods yield a peak directivity of 37.9 dB and a FSLL of −18.5 dB for the array. The E- and H-plane patterns from HO-ADM and HO-MLFMM show excellent agreement. The co-pol equivalent error, $\varepsilon_{\mathrm{ERE}}$, is 0.4 % in the E-plane and 0.3 % in the H-plane. In the E-plane, the cross-pol is below numerical precision, and in the H-plane, the cross-pol error, $\varepsilon_{\mathrm{ERE}}$, is 0.5 % across the entire region of 360°.

4.2 Extension to Non-All-Metal Arrays

Thus far, only purely metallic antennas have been considered, where individual elements are either isolated (as in an array of horn antennas) or linked through a ground plane (like in a patch array). This section addresses the problem of a non-homogeneous background medium, brought about by the presence of several homogeneous dielectric regions (or substrates). In addition, the section deals with the challenge of array structures with a finite thickness. Numerical examples are provided to validate and evaluate the performance of the presented extensions.

We note that the integral equation used here for objects with several dielectric regions is the Poggio-Miller-Chang-Harrington-Wu-Tsai (PMCHWT) formulation [132–134]. It is able to handle an arbitrary number of homogeneous dielectric

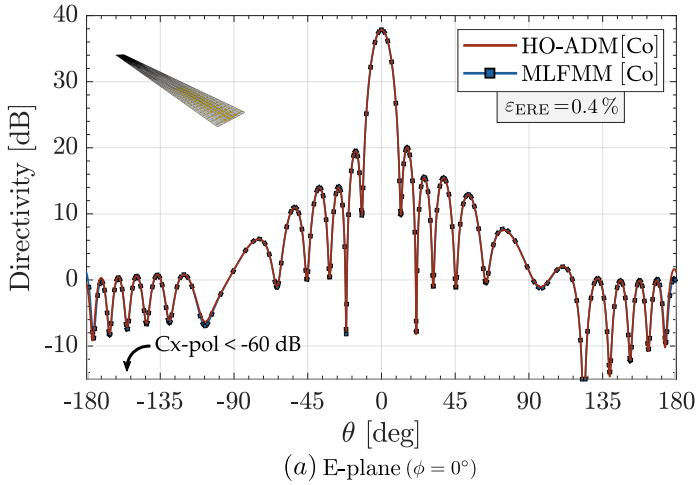

(a) E-plane ($\phi = 0°$)

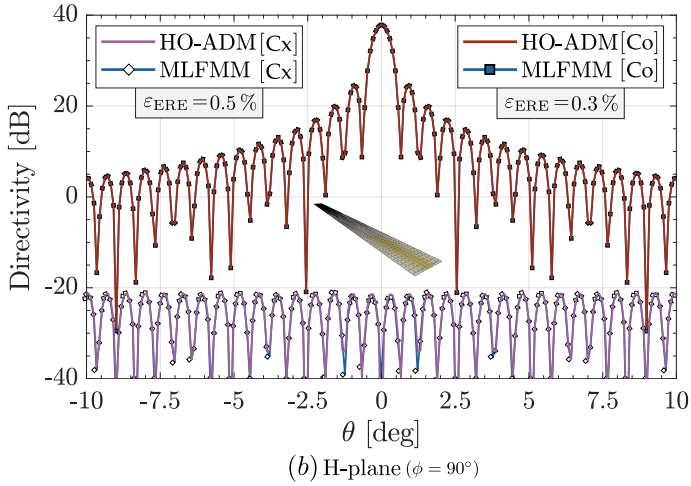

(b) H-plane ($\phi = 90°$)

Figure 4.6: Far-field co- and cross-pol directivity patterns at 1.75 GHz comparing the HO-ADM to the HO-MLFMM for the 8×128-element patch antenna array of Figure 4.5. (a) E-plane patterns ($\phi = 0°$) (b) H-plane patterns ($\phi = 90°$). – Due to the very narrow lobe width in the H-plane only the central 20°-region is shown here.

regions with metallic/dielectric junctions, by exploiting the surface equivalence principle to place equivalent electric and magnetic currents on the surface, and by enforcing tangential continuity of both the total electric and total magnetic field at the junc-

tions*. We emphasize that in the HO-ADM, the PMCHWT formulation is in itself sufficient to support array elements made of dielectric materials, however, only when the dielectric regions are not connected to adjacent array elements. In the following, we present an extension which allows the HO-ADM to analyze connected structures of finite thickness, which in combination with the PMCHWT formulation allows for dielectric substrates.

4.2.1 Internal Walls & Equivalent Currents

To understand the challenge with dielectric substrates in the HO-ADM, one could imagine a simple patch array of identical elements on a dielectric substrate described by a surface discretization. While all the radiating patches of the array are identical, their electromagnetic surroundings are not. A patch in the middle of the array is surrounded by equivalent electric and magnetic currents only on the upper surface of the array and possibly lower, if there is no ground plane. But, a patch at the edge of the array also "sees" equivalent currents on the lateral walls of the array, that is, along the height of the substrate. Thus, the different elements, identical in topology and materials, are subject to different boundary conditions. As a consequence, the MoM matrix is no longer block-Toeplitz, and the HO-ADM cannot be directly applied.

The same challenge applies to the finite thickness plate with holes as depicted in Figure 4.7 (1), which from an electromagnetic perspective consists of non-identical elements. To overcome this problem and to recover the block-Toeplitz property, the structure is first subdivided into four topologically identical elements (see Figure 4.7 (1) and (2)). To also obtain identical elements from an electromagnetic point of view, we let the internal walls radiate into the background medium, just as the external lateral walls of the original structure. Consequently, additional equivalent electric and magnetic currents are placed on the internal walls (see Figure 4.7 (2)), effectively increasing the problem size. Nevertheless, with this approach, the array now consists of identical elements, also from an electromagnetic point of view, and the associated MoM matrix will again be block-Toeplitz.

Finally, the now identical elements are reassembled as shown in Figure 4.7 (3) to obtain the original structure. However, by doing so, the equivalent currents on internal walls are part of the simulation, erroneously simulating their radiation into the background medium. Therefore, currents on internal walls must be excluded from the simulation, which is achieved by utilizing the technique of Section 3.1. Now, what remains is to ensure the continuity of the current over the edges where the individual elements are connected on the top and bottom surfaces (red lines in Figure 4.7 (3)). This is accomplished with the technique presented in Section 3.2, necessitating special care to ensure that:

- the singleton BFs on internal walls and doublet BFs which have support on one (or two) internal walls are hidden from the iterative solver (see Section 3.1).

*The PMCHWT formulation degenerates into the usual EFIE operator for PEC, since here the equivalent magnetic current is zero.

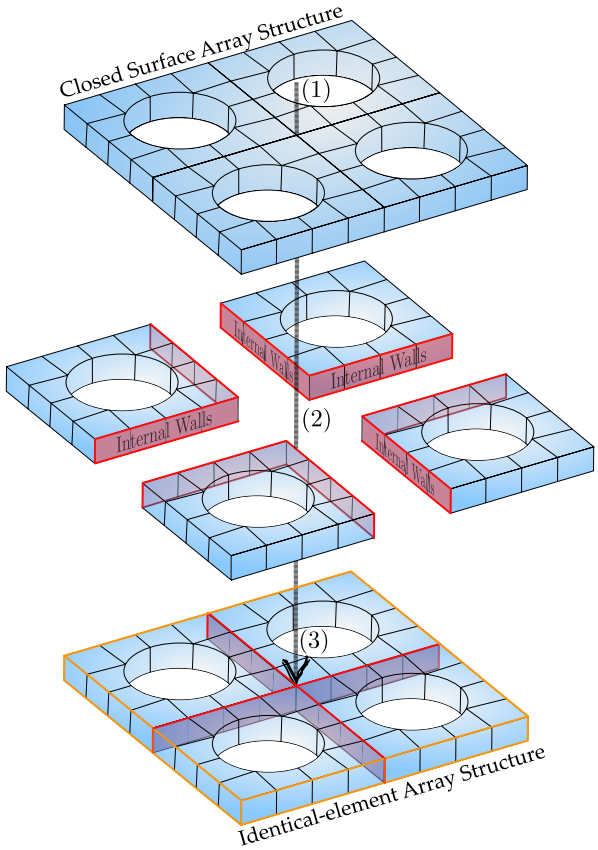

Figure 4.7: Illustration of how (1) an electrically connected array structure is split apart and (2) where equivalent electric and magnetic currents are added on the internal walls to make each element identical. At this stage, all lateral walls of the individual elements radiate into the background medium. (3) The identical elements are put back together. The internal equivalent currents are excluded from the simulation. Current continuity is enforced with half-doublets and DGM, the red lines. On the top and bottom surface, auxiliary DGM unknowns are placed at the orange lines.

- half-doublet BFs should be placed on those edges on which current continuity should be enforced between array elements via DGM, i.e. all edges marked in red in Figure 4.7.

- auxiliary DGM unknowns, as described in Section 3.2.2, are placed on outer array elements on those edges (marked in orange) which would have been connected if that element was completely surrounded by array elements.

We note that although the BFs associated with the internal walls are excluded from the iterative solvers perspective, they are not removed from the underlying full MoM matrix. This implies that the circulant generator $\mathbf{C}$ must accommodate an increasing number of internal wall BF interactions, leading to a progressively larger overhead both in terms of memory consumption and computation time. Nevertheless, this overhead can be significantly decreased in case of electrically thin structures, since the use of a hierarchical basis allows to use lower (even only first) order BFs on the internal walls. In addition, we note that the MoM matrix becomes asymmetric in case of closed PEC structures and/or dielectrics, which effectively doubles the computation time of the circulant generator (i.e. for the setup-phase in HO-ADM) compared to infinitely thin open structures.

To validate the efficiency of the presented internal wall approach we consider a plane wave obliquely incident on a finite thickness PEC plate with 2,500 holes with a diameter of $0.35\lambda_0$, as shown in Figure 4.8. The structure is analyzed as a

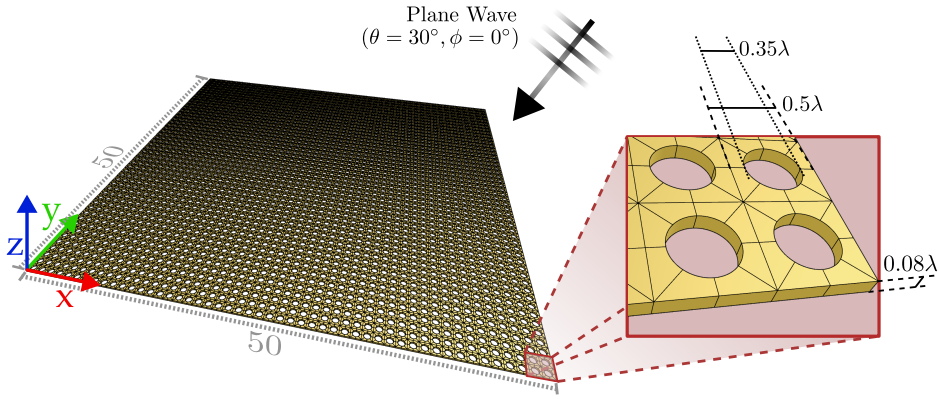

Figure 4.8: Illustration of a plane wave obliquely incident on a $50 \times 50 =$ 2,500-element finite thickness PEC plate with holes with a diameter of $0.35\lambda_0$. The structure is analyzed as an array of identical elements in the HO-ADM, in which the internal walls have been excluded from the simulation.

Method	Total Simulation Time	Memory Consumption	Number of Iterations	Time per Iteration
HO-MLFMM	68 min	18.1 GB	58	8.4 s
HO-ADM	4 min	15.2 GB	165	0.5 s

Table 4.2: Total solution time and memory consumption for the 50×50 array in Figure 4.8, comparing HO-MLFMM and HO-ADM.

$50 \times 50 = 2500$-element array of identical elements in the HO-ADM with a mesh comprising 120,000 quadrilateral mesh cells, resulting in $N = 1{,}140{,}000$ unknowns. In HO-MLFMM, the structure is modeled with 80,800 mesh cells and $N = 646{,}400$ unknowns. From Table 4.2 it is evident that despite HO-MLFMM using almost only half the number of unknowns compared to HO-ADM, the total computation time for HO-MLFMM is 68 min whereas HO-ADM uses 4 min. In addition, the memory consumption of HO-ADM is circa 15 GB whereas HO-MLFMM uses around 18 GB. It is important to recognize that the notably longer setup time for HO-MLFMM primarily stems from the substantial number of interactions included in the near-field interaction matrix, a consequence of the array elements' small electrical dimensions.

4.2.2 Numerical Test Case with Non-All-Metal Array

To validate the accuracy of the internal wall method in case of dielectrics, we consider a Gaussian beam[†] illumination of 400 PEC cylinders with a diameter of $0.2\lambda_0$ embedded in a $0.15\lambda_0$-thick dielectric layer with permittivity of $\varepsilon_r = 3.0$, as shown in Figure 4.9.

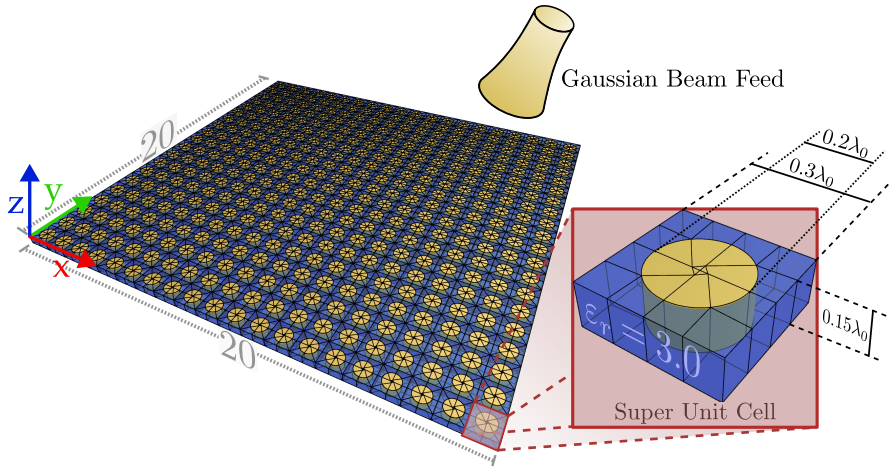

Figure 4.9: Illustration of a $20 \times 20 = 400$-element array of PEC cylinders with a diameter of $0.2\lambda_0$ embedded in a $0.15\lambda_0$-thick dielectric layer with a permittivity of $\varepsilon_r = 3.0$, including the SUC used for analysis in the HO-ADM.

In the HO-ADM, the structure is analyzed as a $20 \times 20 = 400$-element array of identical elements via the SUC depicted in Figure 4.9, with a mesh comprising 28,800 quadrilateral mesh cells, resulting in $N = 422{,}400$ unknowns. In HO-MLFMM, the

[†]The Gaussian beam feed is a Huygens point source radiating a tapered beam, the field of which is similar to that of a real corrugated feed horn. In this case, with a field taper of -20 dB at $\theta = 30°$.

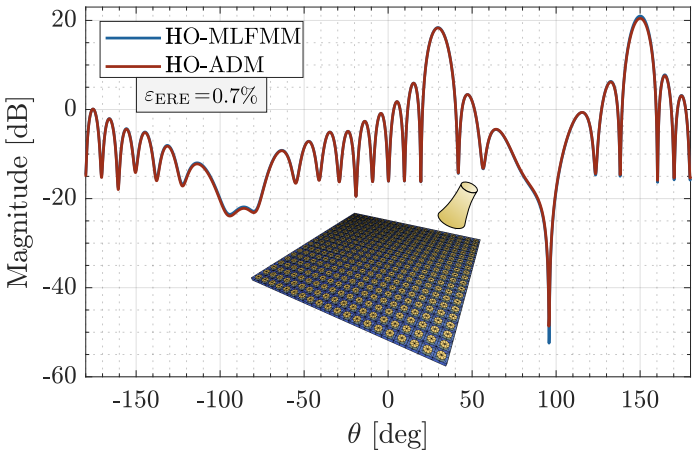

Figure 4.10: Co-pol scattered far-field $\phi = 180°$-cut for an obliquely incident $(\theta_i = 30°, \phi_i = 0°)$ y-polarized Gaussian beam feed on the $20 \times 20 = 400$-element array from Figure 4.9, comparing the HO-ADM to HO-MLFMM.

structure is modeled with 22,720 mesh cells and $N = 267,520$ unknowns. The total computation time for HO-ADM is 11 min while HO-MLFMM is more than an order of magnitude slower.

Figure 4.10 shows the co-polar scattered far-field calculated with the HO-ADM and the HO-MLFMM for the $\phi = 180°$ cut with no significant difference between the two simulations. The equivalent relative error $\varepsilon_{\mathrm{ERE}}$ is 0.7 % across the entire region of 360°. A similar equivalent relative error is observed in the $\phi = 45°$ and $\phi = 90°$ planes.

4.3 Summary

The HO-ADM has been extended to analyze arrays with non-identical elements by introducing the concept of a Super Unit Cell (SUC) and by hiding unknowns from the iterative solution process, effectively allowing the analysis of non-identical elements while retaining an FFT-accelerated MVP.

In addition, by combining all the techniques from Section 3.1, Section 3.2, and Section 4.1.1, an FFT-accelerated rigorous analysis of a 37-element thinned and connected patch array with extended ground plane is made possible. In addition, an $8 \times 128 = 1024$-element patch array can be analyzed in a matter of three minutes compared to half an hour for HO-MLFMM.

To analyze arrays where the elements are connected through a dielectric substrate, the concept of internal equivalent electric and magnetic currents has been introduced to maintain the block-Toeplitz property of the MoM matrix. By carefully excluding BFs associated with these internal equivalent currents, the HO-ADM is able to accurately and efficiently simulate the original structure.

The results show that by using the HO-ADM, an order of magnitude computational speed-up is achievable for arrays with non-identical elements compared to HO-MLFMM, while maintaining a memory consumption comparable to HO-MFLMM.

This page is intentionally not used for content

CHAPTER 5

Summary & Conclusions

In this study, a fast, accurate yet versatile computational analysis technique, denoted the Higher-Order Array Decomposition Method (HO-ADM), has been developed for electrically large arrays for space applications.

As a first step, a survey of existing literature on fast surface integral equation techniques for electrically large arrays was presented. Based on this survey, it was found that even though many of the existing fast methods are already well-suited to accelerate the analysis of general electrically large arrays, they are all based on analytical and/or physical approximations in the calculation of the matrix-vector product (MVP). Despite their error-controllability, the Array Decomposition Method (ADM) stands out as a full-wave solver because it is based on an exact MVP. For this, the ADM exploits the multi-level block-Toeplitz (MBT) property of the MoM matrix, permitting an FFT-accelerated and therefore exact MVP. Nonetheless, its inability to cope with aperiodic arrays, interconnecting geometry, and non-identical elements presented notable impediments which have been resolved in this dissertation.

After implementing the boundary integral part of ADM, it was combined with higher-order (HO) hierarchical Legendre basis functions (BFs). HO-convergence was verified using the HO-ADM for an array of spheres and the use of HO BFs was shown to provide higher accuracy than first-order BFs for the same number of unknowns. For the same accuracy, it has been shown that employing HO BFs in the HO-ADM reduces the total number of unknowns by a factor of nearly three compared to first-order BFs. In addition, numerical tests clearly demonstrated the power of using HO BFs in combination with ADM which generally yields an order of magnitude reduction in both computation time and memory consumption. As an example, a 40 times reduction in total computation time and a ten times reduction in memory consumption has been shown for a 100-element DRA of conical horns on a laptop resulting in a computation time of five minutes.

Comparing the HO-ADM to a state-of-the-art HO-MLFMM implementation, the computation time of HO-ADM was further shown to be more than an order of magnitude faster for arrays with a large number of HO BFs per array element ($s \approx 1000$).

The memory consumption of HO-ADM was shown to be one fourth of HO-MLFMM for array elements with $s < 100$, and on a par with HO-MLFMM for array elements comprising $s \approx 1000$ HO BFs per array element. Bear in mind that this performance is attained while maintaining an exact MVP.

The HO-ADM was extended to allow for the analysis of sparse array antennas by using a technique to implicitly keep the MoM matrix for the fully populated array and by using a constrained Krylov subspace in the iterative solver. We highlight that the latter technique was also crucial for the subsequent enhancements of HO-ADM to arrays with connected and non-identical elements. For a typical number of HO BFs per array element ($s \approx 1000$) and a typical thinning ratio of 40 %, the HO-ADM offers one order of magnitude faster computation time albeit with a modest penalty of increased memory consumption, compared to HO-MLFMM, as shown for a practical 793-element thinned dual-frequency RHCP antenna array.

The HO-ADM was extended to allow for arrays with electrical conduction currents between elements by introducing half-doublets at connected boundaries, using the Discontinuous Galerkin Method (DGM) to enforce current continuity and by introducing auxiliary unknowns to retain the MBT property of the MoM matrix, permitting an FFT-accelerated MVP. Nevertheless, this approach significantly increased the condition number of the MoM matrix, rendering the conventional block-diagonal preconditioning technique ineffective. Instead, a near-field coupling preconditioner was constructed and applied in the HO-ADM, which for a numerical test case with six million unknowns reduced the number of iterations by a factor of 35, going from 1448 to 41 iterations. More importantly, the identification of a constant memory construction of the near-field preconditioner for arrays is what made the extension to connected and sparse arrays feasible in practice. Numerical tests confirmed the efficacy and accuracy of the proposed extensions for a $32 \times 32 = 1024$-element all-metal antenna array designed for the Europa Lander mission, which was analyzed on a laptop within six minutes with one million unknowns. For this case, the HO-ADM showcased a tenfold reduction in computation time in comparison with HO-MLFMM.

The HO-ADM was further extended to arrays with non-identical elements by introducing the concept of a Super Unit Cell (SUC) from which individual mesh regions could be excluded from the iterative solution process. This approach unavoidably leads to an increased number of unknowns, especially in the case of increasing similarity between the non-identical array elements. Nevertheless, the results show that by using the HO-ADM, an order of magnitude computational speed-up compared to HO-MLFMM is achievable even for arrays with non-identical elements, while maintaining a memory consumption comparable to HO-MFLMM. For example, the analysis of a $8 \times 128 = 1024$-element patch array with non-identical elements can be solved with HO-ADM in three minutes compared to half an hour for HO-MLFMM. Furthermore, the extension to non-identical elements combined with all other presented extensions allowed for the analysis of e.g. a 37-element thinned and connected patch array with a ground plane extending beyond the bounds of the array.

Finally, the analysis of connected and finite thickness structures, including dielectric substrates, was made possible by introducing the method of internal walls and

internal equivalent currents, and by employing the Poggio-Miller-Chang-Harrington-Wu-Tsai (PMCHWT) integral equation formulation. The results show efficient and accurate analysis of a $20 \times 20 = 400$-element array of PEC cylinders embedded in a dielectric substrate. Moreover, a finite thickness PEC plate with 2500 holes could be analyzed as a $50 \times 50 = 2500$-element array of identical elements in the HO-ADM with a total computation time of four minutes, compared to 68 min for HO-MLFMM.

In conclusion, the techniques described in the present dissertation allow for the rigorous solution of electrically large arrays, with at least an order of magnitude faster computation time than a state-of-the-art HO-MLFMM implementation, paving the way for more innovative and efficient solutions of electrically large arrays for space applications.

This page is intentionally not used for content

Publications

This chapter contains publications that have been published during the project period, including both conference and journal articles. Each paper is preceded by a front-page including paper title, full author names, the status of publication, and the corresponding bibliography entry.

Paper I

Array Decomposition Method for Arbitrary-Element Regular Arrays using Higher-Order Basis Functions

Magnus Brandt-Møller, Michael Mattes,
Olav Breinbjerg, Min Zhou, Oscar Borries

Status: Published

Bibliography

Array Decomposition Method for Arbitrary-Element Regular Arrays using Higher-Order Basis Functions

Magnus Brandt-Møller, Michael Mattes, Olav Breinbjerg, Min Zhou, Oscar Borries

***Abstract*—The full-wave Array Decomposition Method for regular antenna arrays with arbitrary elements using higher-order hierarchical basis functions is investigated. We show that the use of higher-order basis functions results in significantly reduced memory consumption and computation time for a 10×10 element conical horn array with an aperture size of $22\lambda \times 22\lambda$, without the need for analytical nor numerical approximations. In addition, we demonstrate that by employing higher-order basis functions, the far-field error is considerably lower than by using common first-order basis functions for the same total number of unknowns.**

***Index Terms*—finite arrays, higher-order basis functions, full-wave, block toeplitz, higher-order convergence**

I. Introduction

Antenna arrays have customarily been used as feeds for reflector-based systems and in radar applications. With the current trend to move from large spacecrafts in the geostationary orbit (GEO) to smaller spacecrafts in low earth orbits (LEO), and a concurrent demand for flexible in-orbit configurations, electrically large direct radiating arrays (DRA) are becoming more frequently used for space missions. In this regard, traditional design approaches based on embedded element patterns and array factors or variants thereof have become inadequate, primarily due to their inaccurate modeling of edge and mutual coupling effects. For the typically more densely packed elements in DRA, it is important that mutual coupling effects are taken into account, which together with stringent performance requirements in space substantiates the necessity of rigorous full-wave numerical methods.

Traditional full-wave methods, e.g. the Method of Moments (MoM), suffer from excessive memory consumption and computational complexity, $\mathcal{O}(N^2)$ and $\mathcal{O}(N^2) - \mathcal{O}(N^3)$ respectively, where N is the number of unknowns. A range of methods have been proposed for more efficient analysis of electrically large arrays, in which the memory consumption and computational complexity become $\mathcal{O}(N \log N)$. Examples include the Multi-Level Fast Multipole Method (MLFMM) [1], [2], [3], the Adaptive Integral Method (AIM) [4] [5], and the pre-corrected Fast Fourier Transform (pFFT) [6], and variants hereof [7]. These methods are well suited to accelerate the analysis of general arrays. In the case of regular antenna arrays, the efficiency can be increased even further, both in terms of reduced memory consumption and computation time, by exploiting the regularity of the geometry [8].

The present work concerns the full-wave MoM solution of electrically large regular antenna arrays with arbitrary perfect electrically conducting (PEC) volumetric antenna elements, which is a common configuration for modern antenna arrays. Using the Array Decomposition Method (ADM), the translational invariance of the free-space Green function, together with the regular (e.g. rectangular, triangular or circular) geometrical lattice of the array and a consecutive basis functions (BF) numbering, the resulting MoM matrix becomes multi-level block-Toeplitz [9] which allows for a Fast Fourier Transform (FFT)-accelerated matrix-vector product (MVP) [8], [10] in the iterative solver. It is, however, known that both the computation time and memory consumption of ADM scales as the square of the number of basis functions per array element [10]. Consequently, it is of interest to keep the number of basis functions as low as possible for a fixed solution accuracy. Several approaches have been proposed to reduce the quadratic dependency on the number of basis functions on each array element [11], [8]; they are, however, based on error-controllable approximations.

We demonstrate how the number of basis functions per array element can be reduced using hierarchical higher-order (HO) basis functions [12], while retaining the desired solution accuracy. By using HO-BF in combination with ADM, a significant reduction in computation time and memory consumption can be achieved. Two test cases are used to demonstrate the benefits of higher order basis functions. The HO-ADM is applied to a $10 \times 10\,(22\lambda \times 22\lambda)$ conical horn array, resulting in much lower computation times compared to the ADM using first-order basis functions. We also apply HO-ADM to analyze the scattering from a 5×5 array of PEC spheres and look at the solution error as a function of the total number of unknowns. By increasing the polynomial order, the far-field solution error is considerably lower than by employing first-order basis functions, for the same total number of unknowns. We note that this is the first time, to the knowledge of the authors, such higher-order convergence [13] has been demonstrated using the ADM in combination with hierarchical higher order basis functions.

The paper is organized as follows. Section II outlines the mathematical foundation of the ADM. Section III reviews the employed basis functions and showcases higher-order convergence for an array of PEC spheres. Section IV investigates a direct radiating array, demonstrating the increased efficiency using HO-BF. Conclusions are given in Section V.

II. The Array Decomposition Method

This section outlines the boundary integral (BI) part of ADM [14] from a matrix algebraic perspective with the purpose demonstrating its implementation. We take outset in an

Manuscript created July, 2022; This work was developed by XXX...

arbitrary volumetric antenna array of identical elements, which are placed on a d-dimensional regular lattice, and write the total number of unknowns as

$$N = s\prod_{i=1}^{d} n_i = sT, \tag{1}$$

where s is the total number of basis functions (unknowns) on each array element, d is the total number of array lattice dimensions and n_i is the number of array elements in each dimension i. $T = n_1 n_2 \dots n_d$ is the total number of array elements. Due to the translation symmetry of the 3D free-space Green function, the regular lattice on which array elements are placed, as well as consecutively ordered basis functions, the MoM matrix $\mathbf{A} \in \mathbb{C}^{N\times N}$ becomes multi-level block-Toeplitz of $d+1$ levels. That is, $\mathbf{A}$ consists of $n_1 \times n_1$ block-Toeplitz (BT) matrices which themselves consist of $n_2 \times n_2$ BT sub-blocks, and so forth for the number of array lattice dimensions d. The last level $d+1$ contains, in general, an asymmetric $s\times s$ square matrix containing the basis/test function interactions between the array elements.

The speed-up of ADM comes from an expedited matrix-vector product combined with an iterative solver. The core of ADM can algebraically be regarded as extending the sub-blocks at each level $i = 1, \dots, d$ from Toeplitz to circulant blocks [15, sec. 4.7.7], excluding the blocks at the inner-most level which, in general, do not possess any special symmetry. The extended MoM matrix, $\mathbf{A}^{\mathcal{C}}$, formally increases the number of unknowns $\tilde{N}$ as

$$\tilde{N} = s\prod_{i=1}^{d}(2n_i - 1) \approx 2^d N. \tag{2}$$

The additional unknowns are eventually disregarded, and are as such merely a mathematical trick to allow for the circulant extension. We note that an antenna array on a 1-, 2-, or 3-dimensional regular lattice, results in about 2-, 4-, or 8 times as many unknowns, respectively. Nevertheless, as it will soon become clear, the circulant property allows for a significant reduction in both matrix storage and computational complexity.

Starting with the simpler example $(s = 1, d = 2, [n_1, n_2] = [2, 2])$, $\mathbf{A}^{\mathcal{C}}$ assumes a block-circulant with circulant-blocks (BCCB) structure:

$$\mathbf{A}^{\mathcal{C}} = \left[\begin{array}{c|c|c} \vec{\mathbf{c}}^{\,1} \left\{\begin{bmatrix}\underline{a_1}\\ \underline{a_2}\\ a_3\end{bmatrix}\right. & \begin{matrix}a_3 & a_2\\ a_1 & a_3\\ a_2 & a_1\end{matrix} & \left.\begin{bmatrix}\underline{a_7}\\ \underline{a_8}\\ a_9\end{bmatrix}\right. \begin{matrix}a_9 & a_8\\ a_7 & a_9\\ a_8 & a_7\end{matrix} \\ \hline \vec{\mathbf{c}}^{\,2} \left\{\begin{bmatrix}\underline{a_4}\\ \underline{a_5}\\ a_6\end{bmatrix}\right. & \begin{matrix}a_6 & a_5\\ a_4 & a_6\\ a_5 & a_4\end{matrix} & \left.\begin{bmatrix}\underline{a_1}\\ \underline{a_2}\\ a_3\end{bmatrix}\right. \begin{matrix}a_3 & a_2\\ a_1 & a_3\\ a_2 & a_1\end{matrix} \\ \hline \vec{\mathbf{c}}^{\,3} \left\{\begin{bmatrix}a_7\\ a_8\\ a_9\end{bmatrix}\right. & \begin{matrix}a_9 & a_8\\ a_7 & a_9\\ a_8 & a_7\end{matrix} & \left.\begin{bmatrix}a_4\\ a_5\\ a_6\end{bmatrix}\right. \begin{matrix}a_6 & a_5\\ a_4 & a_6\\ a_5 & a_4\end{matrix} \end{array}\right. \left.\begin{array}{c} \begin{bmatrix}a_1\\ a_2\\ a_3\end{bmatrix}\\ \begin{bmatrix}a_4\\ a_5\\ a_6\end{bmatrix}\\ \begin{bmatrix}a_7\\ a_8\\ a_9\end{bmatrix}\end{array}\right. \begin{matrix}a_4 & a_6 & a_5\\ a_5 & a_4 & a_6\\ a_6 & a_5 & a_4\end{matrix} \\ \hline \begin{matrix}a_1 & a_3 & a_2\\ a_2 & a_1 & a_3\\ a_3 & a_2 & a_1\end{matrix} & \begin{matrix}a_7 & a_9 & a_8\\ a_8 & a_7 & a_9\\ a_9 & a_8 & a_7\end{matrix} \\ \hline \begin{matrix}a_4 & a_6 & a_5\\ a_5 & a_4 & a_6\\ a_6 & a_5 & a_4\end{matrix} & \begin{matrix}a_1 & a_3 & a_2\\ a_2 & a_1 & a_3\\ a_3 & a_2 & a_1\end{matrix} \end{array}\right], \tag{3}$$

in which the entries of the original MoM matrix $\mathbf{A}$ are marked with an underline. Since circulant matrices are uniquely defined by their first row/column, we only need to store the first columns $\vec{\mathbf{c}}^{\,p}$ of size $(2n_1-1)\times 1$ of each circulant block where $p = 1, \dots, 2n_2 - 1$ denotes the index of the circulant block at the second level. The actual number of matrix entries to store become $s^2\prod_{i=1}^{d}(2n_i-1) \approx 2^d s^2 T$ which is linear rather than quadratic in the number of array elements T, compared to the ordinary MoM.

The unique information of the extended-MoM matrix is stored in a $(d = 2)$-dimensional matrix $\mathbf{C}$, which amounts to the first block columns $\vec{\mathbf{c}}^{\,p}$ of $\mathbf{A}^{\mathcal{C}}$

$$\mathbf{C} = \left[\vec{\mathbf{c}}^{\,1}\ \vec{\mathbf{c}}^{\,2}\ \vec{\mathbf{c}}^{\,3}\right] \in \mathbb{C}^{(2n_1-1)\times(2n_2-1)}. \tag{4}$$

The entries in the MVP, $\mathbf{V}$, of the circulant-extended MoM matrix $\mathbf{A}^{\mathcal{C}}$ with a given vector $\vec{\mathbf{x}}$, can be expressed as a $(d = 2)$-dimensional circular convolution

$$\mathbf{V} = \mathbf{C} \circledast \mathbf{X}, \tag{5}$$

in which $\mathbf{X}$ is a $(d = 2)$-dimensional matrix of the same size and dimensions as $\mathbf{C}$ in which the only non-zero elements are the original unknowns placed at the indices $\mathbf{X}_{1\dots n_1, 1\dots n_2}$. Through the circular convolution theorem, the $(d = 2)$-dimensional discrete circular convolution can be expressed in terms of the discrete Fourier transformation as

$$\mathbf{V} = \mathcal{F}_2^{-1}\left\{\mathcal{F}_2\left\{\begin{bmatrix}a_1 & a_4 & a_7\\ a_2 & a_5 & a_8\\ a_3 & a_6 & a_9\end{bmatrix}\right\} \odot \mathcal{F}_2\left\{\begin{bmatrix}x_1 & x_4 & 0\\ x_2 & x_5 & 0\\ 0 & 0 & 0\end{bmatrix}\right\}\right\}, \tag{6}$$

where $\mathcal{F}_2$ denotes the 2-dimensional discrete Fourier transform and $\odot$ denotes the Hadamard operator, i.e. element-wise multiplication. Hereafter, the entries $\mathbf{U}$ of the desired matrix-vector product $\vec{\mathbf{u}} = \mathbf{A}\vec{\mathbf{x}}$, is readily available by accessing the sub-matrix $\mathbf{U} = \mathbf{V}_{1\dots n_1, 1\dots n_2} \in \mathbb{C}^{n_1\times n_2}$, after which the column vector $\vec{\mathbf{u}}$ is obtained by interpreting the contiguous memory column-major matrix $\mathbf{U}$ as a one-dimensional vector.

In the more general case where $(s > 1, d = 2, [n_1, n_2] = [2, 2])$, the unique entries a_k of $\mathbf{A}^{\mathcal{C}}$ for $k = 1, \dots, \tilde{N}$ themselves become matrices $\mathbf{a}_k \in \mathbb{C}^{s\times s}$ with entries denoted by $a_k^{m,n}$, while the vector entries x_k become column vectors $\vec{\mathbf{x}}_k \in \mathbb{C}^{s\times 1}$ with entries enumerated as x_k^n. Since the inner-most $\mathbf{a}_k$ blocks do not, in general, possess any special symmetry they cannot be accelerated by the FFT. Consequently, in order to obtain the full MVP entries $\mathbf{V}$, several matrix-vector products $\mathbf{V}_m$ need to be computed for each $m = 1, \dots, s$ by summation of Hadamard products over $n = 1, \dots, s$ as follows

$$\mathbf{V}_m = \mathcal{F}_2^{-1}\left\{\sum_{n=1}^{s}\mathcal{F}_2\underbrace{\left\{\begin{bmatrix}a_1^{m,n} & a_4^{m,n} & a_7^{m,n}\\ a_2^{m,n} & a_5^{m,n} & a_8^{m,n}\\ a_3^{m,n} & a_6^{m,n} & a_9^{m,n}\end{bmatrix}\right\}}_{\mathbf{C}^{m,n}} \odot \mathcal{F}_2\underbrace{\left\{\begin{bmatrix}x_1^n & x_4^n & 0\\ x_2^n & x_5^n & 0\\ 0 & 0 & 0\end{bmatrix}\right\}}_{\mathbf{X}^n}\right\}. \tag{7}$$

The desired MVP $\vec{\mathbf{u}} = \mathbf{A}\vec{\mathbf{x}}$ is obtained by copying the sub-matrices $\mathbf{U}_m = \mathbf{V}_m(1 : n_1, 1 : n_2)$ interpreted as column-vectors, into $\vec{\mathbf{u}}$ in the order of m. Note that in practice the Fourier transformations $\mathcal{F}_2$ of $\mathbf{C}^{m,n}$ for all m and n is performed only once before entering the iterative solution process, while the Fourier transformation $\mathcal{F}_2$ of $\mathbf{X}_n$ and the inverse Fourier transformation $\mathcal{F}_2^{-1}$ for $\mathbf{V}_m$, over all n and m, respectively, is performed only once per MVP.

In the most general case where $(s > 1, d \geq 1)$, the entries $\mathbf{V}_m$ of the MVP of the circulant-extended MoM matrix $\mathbf{A}^{\mathcal{C}}$ with a given vector $\vec{\mathbf{x}}$ become

$$\mathbf{V}_m = \mathcal{F}_d^{-1}\left\{\sum_{n=1}^{s} \mathcal{F}_d\{\mathbf{C}^{m,n}\} \odot \mathcal{F}_d\{\mathbf{X}^n\}\right\}, \tag{8}$$

where $\mathcal{F}_d$ denotes the d-dimensional discrete Fourier transform. In this general case, $\mathbf{C}^{m,n}$ becomes a d-dimensional tensor containing the entries $a_k^{m,n}$ arranged consecutively in k along the d-dimensions of size $(2n_1-1)\times\ldots\times(2n_d-1)$. $\mathbf{X}$ becomes a d-dimensional tensor of the same size and dimensions in which the only non-zero elements are the original non-extended unknowns placed at the indices $\mathbf{X}_{1\ldots n_1,\ \ldots\ ,1\ldots n_d}$.

In conclusion, in the general case, the computational complexity of ADM is $\mathcal{O}(s^2 T\log(T))$ rather than $\mathcal{O}(N\log N)$. Hence, it is evident that the quadratic scaling with s is a consequence of permitting a general $s\times s$ matrix at the inner most level. Consequently, it is critical to keep the number of basis functions, s, on each array element (i.e. unknowns at the inner-most level) as low as possible without impacting the solution accuracy. This can be achieved using higher-order basis functions as will be demonstrated in the following section.

III. Higher-Order Convergence

In this work, ADM has been implemented using the mixed-potential electric field integral equation (EFIE), as well as the CFIE for closed surfaces [12]. Curved quadrilaterals (mesh-cells) with parametrization $\vec{\mathbf{r}}(u,v)$ are used to discretize the geometry [16], using the HO hierarchical Legendre basis functions from [12] to expand the surface current density as

$$\vec{\mathbf{J}}(u,v) = \frac{\vec{\mathbf{a}}_u}{\mathcal{J}_S(u,v)}\sum_{m=0}^{M^u}\tilde{P}_m(u)\sum_{n=0}^{N^v}C_{mn}^{uv}P_n(v)a_{mn}^u + \frac{\vec{\mathbf{a}}_v}{\mathcal{J}_S(u,v)}\sum_{m=0}^{M^v}\tilde{P}_m(v)\sum_{n=0}^{N^u}C_{mn}^{uv}P_n(u)a_{mn}^v, \tag{9}$$

in which $a_{mn}^{\{u,v\}}$ are the unknown current coefficients in the $\{u,v\}$-direction, $\vec{\mathbf{a}}_{\{u,v\}} = \frac{\partial\vec{\mathbf{r}}}{\partial\{u,v\}}$ are covariant unitary vectors, $\mathcal{J}_S$ is the surface Jacobian and P_n are Legendre polynomials of order n. C_{mn}^{uv} are constants chosen to minimize the MoM matrix condition number and $\tilde{P}_m$ are the modified Legendre polynomials

$$\tilde{P}_m(u) = \begin{cases} 1-u & m=0 \\ 1+u & m=1 \\ P_m(u)-P_{m-2}(u) & m\geq 2 \end{cases}. \tag{10}$$

The value $N^{\{u,v\}} = M^{\{u,v\}} - 1$, and is the maximum polynomial order used for the current expansion in the $\{u,v\}$-direction, which in this paper is denoted by ρ. The key benefit of employing polynomial orders $\rho > 1$ is that the discretization error behaves as $\mathcal{O}(h^\rho)$, where h is a relative mesh cell size [13]. That is, increasing the polynomial order ρ of employed basis functions theoretically yield better accuracy than increasing the mesh discretization (for the same number of unknowns). This property is customarily denoted as HO convergence, and has been verified for a single sphere for MoM [17] and MLFMM [18]. Note that in practice the polynomial order is adjusted to the electrical size of each mesh cell, since a general rule for choosing the optimum polynomial order a priori is not available. In this work we have used a fixed polynomial order on all mesh cells for the purpose of showing HO convergence.

A. Array of Spheres

To demonstrate HO convergence in HO-ADM, we consider a 5×5 array of PEC spheres (Fig. 1) with inter-element distance of $L = 16\lambda$ and diameter $D = 5\lambda$, illuminated by an $\hat{\mathbf{x}}$-polarized plane wave, propagating along the z-axis. The scattered electric far-field intensity is evaluated and compared to an accurate reference solution using the total relative RMS error measure (denoted far-field error)

$$\epsilon_{RMS} = \sqrt{\frac{\sum_{i=1}^{N_s}|\mathbf{E}_{i,\mathrm{ref}} - \mathbf{E}_i|}{\sum_{i=1}^{N_s}|\mathbf{E}_{i,\mathrm{ref}}|}}, \tag{11}$$

where $\mathbf{E}_{i,\mathrm{ref}}$ is the reference electric far-field, $\mathbf{E}_i$ is the calculated electric far-field vector and N_s is the number of far-field samples in a regular grid over the 4π far-field sphere. Because an analytical solution is not readily available, the reference is a direct solution of the full HO-MoM matrix with high integration precision and as fine a discretization as possible within memory limits.

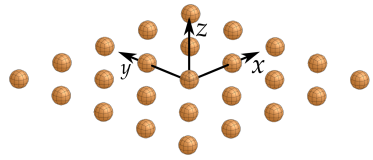

Fig. 1: 5×5 element PEC sphere array. 5λ diameter. 16λ inter-element distance.

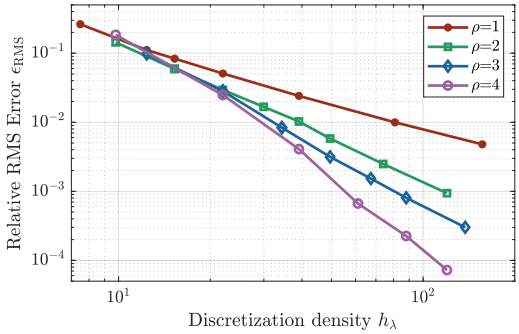

Fig. 2: Relative RMS error ϵ_{RMS} as a function of the discretization density h_λ (i.e. the number of unknowns normalized by total surface area in square wavelengths).

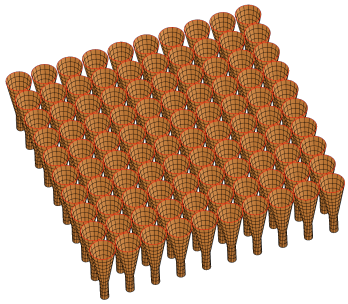

Fig. 3: 10×10 element conical horn array. 2.1λ aperture diameter. 5.6λ horn height. 2.2λ inter-element distance.

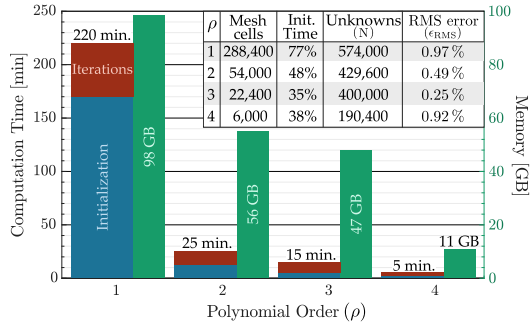

Fig. 4: Total computation time and memory consumption for HO-ADM required to reach $< 1\%$ far-field RMS error.

In Fig. 2, the far-field error ϵ_{RMS} for the sphere array is evaluated as a function of the discretization density $h_\lambda = \frac{N}{\Omega_\lambda}$, where Ω_λ is the total surface area in square wavelengths. For a discretization density $h_\lambda < 20$, employing higher polynomial orders $\rho > 1$ does not yield a more accurate far-field. However, as the discretization density rises above $h_\lambda > 20$, a clear distinction between the curves for different polynomial orders can be made. For a discretization density $h_\lambda > 100$ the far-field for $\rho = 4$ is around two orders of magnitude more accurate than the far-field for $\rho = 1$. Moreover, for higher polynomial orders, the increasing slope of the error curves agree with the theoretical estimate $\mathcal{O}(h^\rho)$. We note that this is the first time, that HO convergence has been demonstrated for an array using the ADM with hierarchical higher order basis functions.

IV. Conical Horn Array

As second example, we consider a $22\lambda \times 22\lambda$ direct radiating array (Fig. 3) which consists of 10×10 conical horn antennas fed by circular waveguides excited uniformly with the fundamental mode TE_{11}. The radiated far-field pattern has been calculated using HO-ADM on a computer with an Intel®Xeon®5218 CPU @ 2.3 GHz with 16 cores. A reference solution has been generated using the smallest mesh length possible on the available system. For fixed basis function order, ρ, the maximal admissible mesh length has been varied between 0.15λ and 1.5λ to ensure a relative total RMS error ϵ_{RMS} in the radiated far-field forward hemisphere that is less than $1\,\%$ (far-field requirement).

Fig. 4 shows the total computation time (including initialization and iterative solution) and memory consumption, for different basis function orders ρ. For each order ρ, the maximal admissible mesh length has been decreased until reaching the far-field requirement (or lower). For $\rho = 1$, a total of 288,400 mesh cells ($\approx 0.15\lambda$) are needed to satisfy the far-field requirement, which is considerably more than the 54,000 mesh cells ($\approx 0.3\lambda$) needed for $\rho = 2$. The high number of mesh cells for $\rho = 1$ results in high ADM initialization time, primarily due to the increased number of integrals to compute.

The significant reduction in computation time from 220 min. ($\rho = 1$) to 25 min. ($\rho = 2$) can be explained primarily by the decrease in the number of mesh cells. Notably, due to meshing constraints, the mesh is more refined for $\rho = 2$ and $\rho = 3$, resulting in a two and four times lower RMS error, respectively, than the solution for $\rho = 1$ and $\rho = 4$. The increased accuracy is the primary reason for the relatively small decrease in total number of unknowns, memory consumption and computation time from $\rho = 2$ to $\rho = 3$. Nevertheless, a significant fourfold reduction in memory consumption (47 GB to 11 GB) and a threefold reduction in computation time (15 min. to 5 min.) is evident going from $\rho = 3$ with 22400 mesh cells ($\approx 0.5\lambda$) to $\rho = 4$ with 6,000 mesh cells ($\approx 1.0\lambda$). Note that increasing the polynomial order above four for the present example requires a coarser mesh than possible for the given geometrical structure.

The results clearly demonstrate superior performance when increasing the basis function order. This is most clearly seen going from $\rho = 1$ to $\rho = 4$, where the total computation time decreases by a factor of about 40 and the memory consumption decrease by a factor of about 10. Moreover, by increasing the polynomial order by one (from $\rho = 1$ to $\rho = 2$), the total computation time decreases by a factor of nine, the memory decreases by a factor of two, even while the RMS error is halved.

V. Conclusion

In this contribution, the Array Decomposition Method and HO hierarchical basis functions have been combined for the first time to the authors' best knowledge. The efficiency of employing HO basis functions to represent the surface current density has been shown for both a scattering problem (array of spheres) and a radiation problem (conical horn array), achieving HO convergence.

The results show that substantial memory savings and considerable computational speed-ups are possible by this combination while at the same time maintaining, or even improving, the accuracy. In the present test case of a 10×10 element conical horn array ($22\lambda \times 22\lambda$), memory consumption could be reduced by a factor of up to 10 and the simulation accelerated up to 40 times, when going from first- to fourth-order basis functions.

REFERENCES

[1] R. Coifman, V. Rokhlin, and S. Wandzura, "The fast multipole method for the wave equation: A pedestrian prescription," *IEEE Antennas and Propagation magazine*, vol. 35, no. 3, pp. 7–12, 1993.

[2] C.-C. Lu and W. C. Chew, "A multilevel algorithm for solving a boundary integral equation of wave scattering," *Microwave and Optical Technology Letters*, vol. 7, no. 10, pp. 466–470, 1994.

[3] B. Karaosmanoğlu and Ö. Ergül, "Acceleration of MLFMA simulations using trimmed tree structures," *IEEE Transactions on Antennas and Propagation*, vol. 69, no. 1, pp. 356–365, 2020.

[4] E. Bleszynski, M. Bleszynski, and T. Jaroszewicz, "AIM: Adaptive integral method for solving large-scale electromagnetic scattering and radiation problems," *Radio Sci.*, vol. 31, no. 5, pp. 1225–1251, 1996.

[5] S. Sharma and P. Triverio, "AIMx: an extended adaptive integral method for the fast electromagnetic modeling of complex structures," *IEEE Transactions on Antennas and Propagation*, vol. 69, no. 12, pp. 8603–8617, 2021.

[6] J. White, J. Phillips, and T. Korsmeyer, "Comparing precorrected-FFT and fast multipole algorithms for solving three-dimensional potential integral equations,"," in *Proceedings of the Colorado Conference on Iterative Methods*. Citeseer, 1994, pp. 4–10.

[7] C.-F. Wang, F. Ling, and J.-M. Jin, "A fast full-wave analysis of scattering and radiation from large finite arrays of microstrip antennas," *IEEE Transactions on Antennas and Propagation*, vol. 46, no. 10, pp. 1467–1474, 1998.

[8] R. W. Kindt and J. L. Volakis, "Array decomposition-fast multipole method for finite array analysis," *Radio Sci.*, vol. 39, no. 2, pp. 1–9, 2004.

[9] A. Geranmayeh, W. Ackermann, and T. Weiland, "FFT accelerated marching-on-in-order methods," in *2008 38th European Microwave Conference*. IEEE, 2008, pp. 511–514.

[10] E. H. Bleszynski, M. K. Bleszynski, and T. Jaroszewicz, "Block-Toeplitz fast integral equation solver for large finite periodic and partially periodic array systems," *IEICE Trans. Electron.*, vol. 87, no. 9, pp. 1586–1594, 2004.

[11] R. Kindt, K. Sertel, E. Topsakal, and J. L. Volakis, "An extension of the array decomposition method for large finite-array analysis," *Microw. Opt. Technol. Lett.*, vol. 38, no. 4, pp. 323–328, 2003.

[12] E. Jørgensen, J. L. Volakis, P. Meincke, and O. Breinbjerg, "Higher order hierarchical Legendre basis functions for electromagnetic modeling," *IEEE Transactions on Antennas and Propagation*, vol. 52, no. 11, pp. 2985–2995, 2004.

[13] J.-C. Nédélec, "Mixed finite elements in R3," *Numerische Mathematik*, vol. 35, no. 3, pp. 315–341, 1980.

[14] R. W. Kindt, K. Sertel, E. Topsakal, and J. L. Volakis, "Array decomposition method for the accurate analysis of finite arrays," *IEEE Transactions on Antennas and Propagation*, vol. 51, no. 6, pp. 1364–1372, 2003.

[15] G. H. Golub and C. F. Van Loan, *Matrix computations*. JHU Press, 1996.

[16] R. D. Graglia, D. R. Wilton, and A. F. Peterson, "Higher order interpolatory vector bases for computational electromagnetics," *IEEE Transactions on Antennas and Propagation*, vol. 45, no. 3, pp. 329–342, 1997.

[17] E. Jørgensen, *Higher-order integral equation methods in computational electromagnetics*. Ørsted-DTU, PhD Dissertation, 2003.

[18] O. Borries, P. Meincke, E. Jørgensen, and P. C. Hansen, "Multilevel fast multipole method for higher order discretizations," *IEEE Transactions on Antennas and Propagation*, vol. 62, no. 9, pp. 4695–4705, 2014.

Paper II

Extended Higher-Order Array Decomposition Method for Fully Populated or Thinned Array Antennas and Scatterers with Connected Elements

Magnus Brandt-Møller, Michael Mattes, Olav Breinbjerg, Min Zhou, Erik Jørgensen

Status: Accepted 06/09-2023

Bibliography

Extended Higher-Order Array Decomposition Method for Fully Populated or Thinned Array Antennas and Scatterers with Connected Elements

Magnus Brandt-Møller, Michael Mattes, Olav Breinbjerg, Min Zhou and Erik Jørgensen

***Abstract*—The Higher-Order Array Decomposition Method (HO-ADM) is extended to handle fully populated or thinned finite array antennas and scatterers which can be modeled as arrays with connected elements lying on a regular lattice. The Discontinuous Galerkin Method (DGM) is employed to retain the multi-level block-Toeplitz Method of Moments (MoM) matrix structure even for connected elements. Moreover, by zeroing a selected subset of unknowns in the iterative solution process, thinned arrays can be handled as well. The presented method yields more than an order of magnitude shorter solution times for both a 32×32-element square- and a 793-element circular-thinned array with a memory consumption comparable to existing fast methods such as MLFMM.**

***Index Terms*—thinned array antennas, connected array elements, multi-level block-Toeplitz, discontinuous Galerkin method of moments, higher-order basis functions**

I. Introduction

ARRAY antennas have become a key component in numerous wireless communication and sensing applications. Phased array antennas are becoming an imperative part of next-generation space payloads and user terminals as they offer in-orbit reconfigurability and electronically steerable beams.

In order to accommodate the stringent performance requirements for space applications, future array antennas will be electrically and physically large with numerous densely packed array elements. Their performance is difficult to predict using traditional computational techniques such as embedded element patterns, primarily due to the inaccurate modeling of mutual coupling and edge effects. In addition, the larger number of needed unknowns challenges traditional full-wave numerical methods regarding memory consumption and solution time. This difficulty is further compounded when seeking an efficient solution for large finite arrays characterized by a thinned lattice, geometrically interconnected elements, and different element geometries.

For the conventional full-wave Method of Moments (MoM) for surface integral equations, the memory consumption and computational complexity scales as $\mathcal{O}(N^2)$ and $\mathcal{O}(N^2) - \mathcal{O}(N^3)$, respectively, where N is the number of unknowns. Although MoM is considered accurate in the sense that it rigorously takes into account mutual coupling and edge effects, its computational scaling is prohibitively large for the design of future electrically large but finite array antennas.

Thanks to...
TBD TBD and TBD TBD are with Anonymous University.
Manuscript received #, 2023; revised #, 2023.

Numerous proposed integral-equation-based methods enable efficient full-wave analysis of electrically large arrays, in which the memory scaling and computational complexity can be reduced to as low as $\mathcal{O}(N \log N)$ by means of error-controllable approximations.

One class is the multipole-based methods such as the Multi-Level Fast Multipole Method (MLFMM) [1], [2] which is a widely used error-controllable full-wave method for electrically large structures [3], [4], [5]. Nevertheless, sub-wavelength array element sizes and spacings pose a challenge in conventional MLFMM which in addition does not exploit the typical periodic nature of arrays [6].

A second class of methods is based on MacroBasis Functions (MBFs) such as characteristic basis functions (CBF) [7], [8], synthetic basis functions (SBF) [9] and accurate subentire-domain (ASED) [10] basis functions, which are all able to drastically reduce the number of unknowns in the MoM by aggregating many elementary basis functions (BFs) into fewer groups. Nevertheless, the generation and number of MBFs to include is in general problem specific, making the asymptotic scaling difficult to predict.

A third class of methods such as the fast Integral Equation Solver (IES) [11], Integral Equation QR algorithm (IE-QR) [12] and Adaptive Cross Approximation (ACA) [13] is based on lossy matrix compression. These methods can be regarded as algebraic in nature, in that they work by cleverly grouping and/or by factorization of unknowns with the aim of improving the compressibility of the system matrix and accelerating the simulation speed. Similar methods denoted as fast direct solvers are also based on compression, but focus strictly on efficient factorization and direct solution of the linear system [14], [15].

A fourth class of full-wave methods exploits the circular convolution theorem which allows the use of a Fast Fourier Transform (FFT) to accelerate the solution process. Examples are the Adaptive Integral Method (AIM) [16], [17], the pre-corrected Fast Fourier Transform method (pFFT) [18], the Integral Equation Fast Fourier Transform method (IE-FFT) [19]. In order to utilize the FFT, these methods require a regular lattice onto which the unknowns are projected.

We note that complementary methods based on the Domain Decomposition Method also allow for a very memory-efficient analysis of large finite arrays [20], [21], performing particularly well when combined with the Finite Element Method (FEM) in case of arrays with complicated stack-ups. On the other hand, integral-equation-based methods have a distinct

advantage in inherently satisfying the open boundary radiation condition, eliminating the need for absorbing boundary conditions.

Although the above-mentioned methods employ physically and/or analytically-based approximations, most of them are error controllable, making them well-suited to accelerate the analysis of general electrically large arrays. Nevertheless, when array elements are placed on a regular lattice the computation efficiency can be improved without compromising accuracy by employing the Array Decomposition Method (ADM) [22]. The ADM exploits the translational invariance of the 3D free-space Green function in connection with the regular geometrical lattice (e.g. rectangular, hexagonal or circular) of the array elements and consecutively ordered basis functions, allowing an FFT-accelerated matrix-vector product (MVP) [22], [23] in an iterative solution process. At the penalty of approximation, the ADM can be extended using FMM, yielding $\mathcal{O}(N)$ memory consumption and a solution time which can be faster than that of ADM alone, provided that the number of far-field directions used in the basis function expansions is less than the number of unknowns on each array element [24].

Recently, the boundary integral part of ADM has been implemented with higher-order (HO) basis functions and shown to use significantly less unknowns for a given accuracy [25]. The present work concerns two further extensions to the full-wave Higher-Order Array Decomposition Method (HO-ADM) [25] for array antennas or scatterers with arbitrary perfect electrically conducting (PEC) volumetric antenna elements. In this paper, the HO-ADM is extended to allow for conduction currents between connected elements, and thus allowing for arrays with a ground-plane or other interconnecting features. A second extension is that the regular lattice does not need to be fully populated with identical array elements, hence permitting thinned arrays. The two extensions presented in this work allow for significant computational and memory savings in the HO-ADM when applied to connected and thinned arrays. This includes such challenging cases as, but not limited to, circular arrays, arrays with a ground-plane extending beyond the bounds of the array, and even scatterers which can be modeled as finite arrays such as a PEC plate, a cylinder, or other 2D profiles that can be extruded and modeled as an array.

The paper is organized as follows. Section II reviews the basic HO-ADM. Section III discusses the necessary extensions to HO-ADM to be able to analyze connected and thinned arrays. Section IV presents various numerical examples validating the capabilities of the extended HO-ADM. Lastly, conclusions are given in Section V. Time-harmonic variation and phasor notation is employed throughout the manuscript.

II. Higher-Order Array Decomposition Method

This section summarizes the HO-ADM [25], in which the mixed-potential electric field integral equation (EFIE), as well as the combined field integral equation (CFIE) for closed surfaces [26] have been employed.

A. Surface Discretization and Basis Functions

Curved quadrilaterals (i.e. mesh-cells), henceforth referred to as quads, with parametrization $\vec{\mathbf{r}}(u,v)$ are used to discretize the geometry [27], using the HO-hierarchical Legendre BFs from [26] to expand the surface current density as

$$\vec{\mathbf{J}}(u,v) = \frac{\vec{\mathbf{e}}_u}{\mathcal{J}_S(u,v)} \sum_{m=0}^{M^u} \sum_{n=0}^{N^v} C_{mn}^{uv} \tilde{P}_m(u) P_n(v) \alpha_{mn}^u + \frac{\vec{\mathbf{e}}_v}{\mathcal{J}_S(u,v)} \sum_{m=0}^{M^v} \sum_{n=0}^{N^u} C_{mn}^{uv} \tilde{P}_m(v) P_n(u) \alpha_{mn}^v, \quad (1)$$

in which $\{u,v\}$ are curvilinear coordinates, $\alpha_{mn}^{\{u,v\}}$ are the unknown current coefficients in the $\{u,v\}$-direction, $\vec{\mathbf{e}}_{\{u,v\}} = \frac{\partial \vec{\mathbf{r}}}{\partial \{u,v\}}$ are unitary vectors, $\mathcal{J}_S$ is the Jacobian determinant, P_n are Legendre polynomials of order n and C_{mn}^{uv} are constants chosen to minimize the MoM matrix condition number. $\tilde{P}_m$ are modified Legendre polynomials defined as

$$\tilde{P}_m(u) = \begin{cases} 1-u, & m=0 \\ 1+u, & m=1 \end{cases} \Big\} \textbf{ Doublets} \quad \begin{cases} P_m(u) - P_{m-2}(u), & m \geq 2 \end{cases} \textbf{ Singletons}, \quad (2)$$

used only in the direction of the current. Herein, doublets correspond to the usual roof-top continuity-enforcing BFs having support over two quads. Singletons model local current density variations and have support only within a single quad. Other BF-formulations, e.g. Rao-Wilton-Glisson BFs on triangular cells can be used as well. Nevertheless, by using quads (instead of triangular cells) only two vectors (instead of three) are needed to represent the current, which, combined with the choice of the HO BFs in (1), enables better accuracy for the same number of unknowns [28]. In addition, since it is a hierarchical basis, the maximum polynomial order $N^{\{u,v\}} = M^{\{u,v\}} - 1$ for the current expansion in the $\{u,v\}$-direction can be chosen independently for each quad based on its electrical size.

B. Accelerated Matrix-Vector Product

For an array of antennas or scatterers with identical elements placed on a d-dimensional regular lattice, the total number of unknowns N can be formulated as

$$N = s \prod_{i=1}^{d} n_i = sT, \quad (3)$$

where s is the total number of unknowns on each array element, T is the total number of array elements and n_i is the number of elements in the i^{th} lattice dimension. Due to the translational invariance of the three-dimensional free-space Green function, the regular lattice on which array elements are placed, as well as consecutively ordered BFs, the MoM matrix $\mathbf{A} \in \mathbb{C}^{N \times N}$ becomes a multi-level (a)symmetric block-Toeplitz matrix of $d+1$ levels as depicted in Fig. 1b for a $T = 2 \times 3 = 6$-element array. That is, $\mathbf{A}$ consists of $n_d \times n_d$ block-Toeplitz (BT) matrices which themselves consist of $n_{d-1} \times n_{d-1}$ BT sub-blocks, and so forth for the

number of array lattice dimensions d. By using the HO-hierarchical Legendre BFs from (1), the inner-most level contains asymmetric square matrices $\mathbf{a} \in \mathbb{C}^{s\times s}$ comprising basis/test function interactions. The unknowns associated with a given array element at lattice position (a, b) is denoted as $\vec{\mathbf{x}}_{a,b}$, where $a \in \{1, \ldots, n_1\}$ and $b \in \{1, \ldots, n_2\}$.

In order to achieve an FFT-accelerated MVP, the sub-blocks at each level are extended from Toeplitz to circulant [29, sec. 4.7.7] as exemplified in Fig. 1 going from (b) $\rightarrow$ (c). The resulting extended MoM matrix, $\mathbf{A}^{\mathcal{C}}$, formally increases the number of unknowns to $\tilde{N} = s\prod_{i=1}^{d}(2n_i - 1)$, and merely serves as a mathematical trick since it does not require any zero-padding of $\mathbf{A}$ nor additional computation. This is evident from Fig. 1c, where the rearrangement of the blocks $\mathbf{a}_{k,l}$ suffices. Herein $k \in \{1, \ldots, 2n_1-1\}$ and $l \in \{1, \ldots, 2n_2-1\}$ enumerate the rearranged blocks at the first ($i = 1$) and second ($i = 2$) block-circulant level, respectively.

To ensure that the MVP with the extended MoM matrix $\mathbf{A}^{\mathcal{C}}\vec{\mathbf{x}}^{\mathcal{C}}$ contains entries equal to the original MVP, the unknown vector $\vec{\mathbf{x}} \in \mathbb{C}^{N\times 1}$ is extended to $\vec{\mathbf{x}}^{\mathcal{C}} \in \mathbb{C}^{\tilde{N}\times 1}$ as illustrated in Fig. 1c. Zeroes are placed at the positions pertaining to the extended blocks, i.e. $\vec{\mathbf{x}}_{k,l} = 0$ for $k > n_1 \wedge l > n_2$. The MVP $\mathbf{A}^{\mathcal{C}}\vec{\mathbf{x}}^{\mathcal{C}}$ favorably becomes a discrete circular block convolution operation which can be accelerated via the FFT.

In conclusion, the computational complexity of the HO-ADM becomes $\mathcal{O}(s^2T)$ in setup time and $\mathcal{O}(s^2T\log(T))$ for the MVP. The memory consumption is $\mathcal{O}(s^2T)$. Note that the quadratic scaling with s is a consequence of permitting a general matrix $\mathbf{a}_{k,l}$ at the inner most level. Nevertheless, by employing the HO-hierarchical BFs, s can be kept low (compared to ordinary first-order BFs) without impacting the solution accuracy [25].

III. Extended Array Decomposition Method

In the existing HO-ADM no conduction current is allowed to flow between elements, effectively excluding arrays with a ground-plane or other interconnecting features. Another restriction is that the regular d-dimensional lattice has to be fully populated with identical array elements. In this section two contributions to the existing HO-ADM are presented enabling it to handle electrically connected and thinned arrays. From this point, HO-ADM will refer to the extended method.

A. Extension to Thinned Arrays

Thinned array antennas are obtained by terminating or removing elements from uniformly spaced arrays [30]. The main motivation for thinning array antennas is the achievable reduction in cost and weight, without compromising desired performance parameters such as gain, beamwidth, or side lobe level. Another incentive for thinning can be spatial constraints, where the outer elements in a regular array need to be removed to conform to a given rim. In the remainder of this paper, the term thinning will refer to the removal of elements.

The challenge in retaining an FFT-accelerated MVP, when array elements are removed, is that the multi-level block-Toeplitz (MBT) property of the system matrix is lost. The

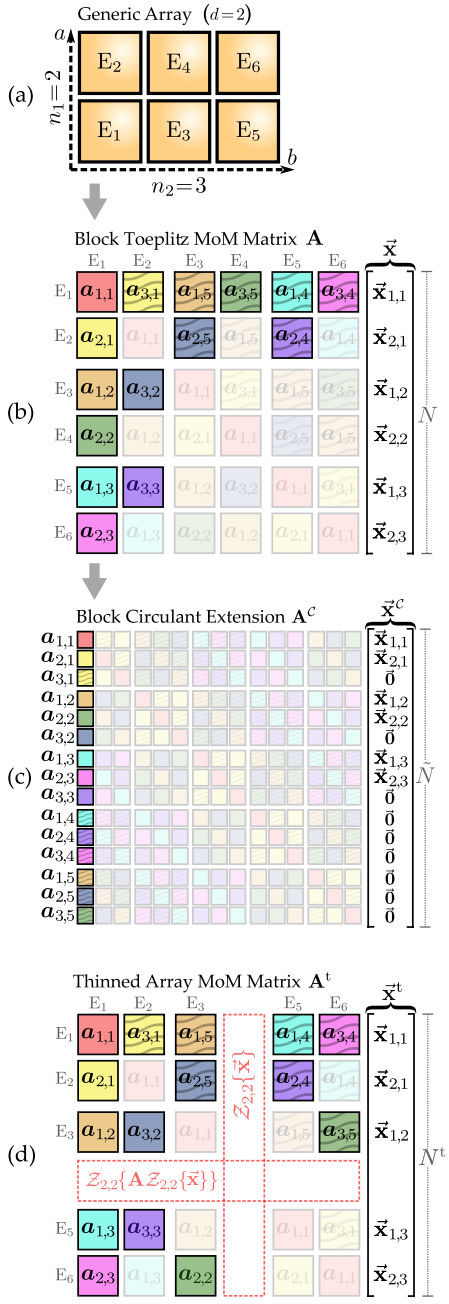

Fig. 1: Example of (a) $T = 2\times 3 = 6$-element generic array, (b) the resulting multi-level block Toeplitz MoM matrix $\mathbf{A}$ with $N = sT$ unknowns, (c) its full circulant extension $\mathbf{A}^{\mathcal{C}}$ with $\tilde{N} \approx 2^d N$ unknowns and (d) the thinned MoM matrix $\mathbf{A}^{\mathrm{t}}$ after removing element four (E_4). Colors indicate similar interaction matrices, while faint colors indicate blocks that do not need to be computed nor stored. A wavy pattern indicates blocks that have to be computed if the employed integral operators are not symmetric. In case of symmetric operators their calculation can be omitted.

thinned MoM matrix $\mathbf{A}^{\mathrm{t}} \in \mathbb{C}^{N^{\mathrm{t}} \times N^{\mathrm{t}}}$ results in the reduced system

$$\mathbf{A}^{\mathrm{t}} \vec{\mathbf{x}}^{\,\mathrm{t}} = \vec{\mathbf{b}}^{\,\mathrm{t}}, \tag{4}$$

where $\vec{\mathbf{x}}^{\,\mathrm{t}} \in \mathbb{C}^{N^{\mathrm{t}} \times 1}$ is the resulting thinned unknown vector, $\vec{\mathbf{b}}^{\,\mathrm{t}} \in \mathbb{C}^{N^{\mathrm{t}} \times 1}$ is the thinned right-hand side, and N^{t} is the total number of unknowns after thinning the array. Fig. 1d shows an example where the removal of array element number four (E_4) and its associated unknowns $\vec{\mathbf{x}}_{2,2}$ results in the deletion of both a block-row and -column which in turn destroys the MBT structure.

Instead of removing elements from $\mathbf{A}$, one remedy to maintain the MBT structure is to keep $\mathbf{A}$ as is, but employ zeroing of the unknown vector and the MVP result. Herein the full length of the unknown and right-hand side vectors is retained, while the unknowns and MVP entries associated with removed elements are forced to zero. Mathematically, the MVP for the thinned system can be formulated as

$$\mathbf{A}^{\mathrm{t}} \vec{\mathbf{x}}^{\,\mathrm{t}} = \mathcal{Z}_{a,b}\{\mathbf{A}\mathcal{Z}_{a,b}\{\vec{\mathbf{x}}_i\}\}, \tag{5}$$

where $\mathcal{Z}_{a,b}$ is a zeroing function placing zeros at those positions (a, b) in the vector which pertains to the removed array element(s) and $\vec{\mathbf{x}}_i \in \mathbb{C}^{N \times 1}$ is the i^{th} iteration solution vector guess. Because $\mathcal{Z}_{a,b}\{\vec{\mathbf{x}}_i\}$ is of full length N, it can be multiplied on the full MoM matrix $\mathbf{A}$ possessing the MBT property, effectively preserving the FFT-acceleration.

The zeroing of unknowns pertaining to e.g. element number four (E_4) via $\mathcal{Z}_{2,2}\{\vec{\mathbf{x}}_i\}$, being equivalent to $\vec{\mathbf{x}}_{2,2} = 0$, effectively removes the influence of the blocks in column number four as illustrated with the vertical red dashed rectangle in Fig. 1d. From an electromagnetic perspective, zeroing basis function coefficients $\mathcal{Z}\{\vec{\mathbf{x}}_i\}$ in each iteration can be interpreted as enforcing zero current flow on removed element(s). Remark, however, that this does not eliminate the corresponding block-row number four, which represents the coupling from all other elements to the removed element. Therefore, to also remove the influence of the row, the MVP result $\mathbf{A}\mathcal{Z}_{2,2}\{\vec{\mathbf{x}}_i\}$ should be zeroed as well, as indicated with the horizontal red dashed rectangle in Fig. 1d.

In addition, the right-hand side vector $\vec{\mathbf{b}}$ must be zeroed accordingly in order for the iterative solver to calculate the correct residual vectors $\vec{\mathbf{r}}_i$, that is

$$\vec{\mathbf{r}}_i = \mathcal{Z}_{a,b}\{\vec{\mathbf{b}}\} - \mathcal{Z}_{a,b}\{\mathbf{A}\mathcal{Z}_{a,b}\{\vec{\mathbf{x}}_i\}\}. \tag{6}$$

Zeroing the resulting MVP, i.e. $\mathcal{Z}\{\mathbf{A}\mathcal{Z}\{\vec{\mathbf{x}}_i\}\}$, can be understood as not letting the coupling field from all other elements induce any current on the removed element(s). In short, by appropriately zeroing, the iterative solver will converge to the same solution as if the ordinary MVP $\mathbf{A}^{\mathrm{t}}\vec{\mathbf{x}}^{\,\mathrm{t}}$ was applied for the truncated system.

B. Extension to Electrically Connected Arrays

The MBT property of $\mathbf{A}$ is lost in the case of electrically connected array elements. This is because the doublet basis function coefficients α_{0n}, α_{1n} on connected edges have to be associated with either one or the other array element. In order to overcome this limitation, the Discontinuous Galerkin Method (DGM) for surface integral equations is employed [31].

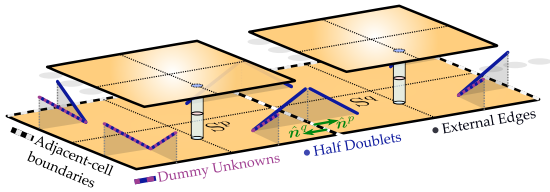

Fig. 2: Two patch elements at the corner of a larger ground-plane-connected array. Half-doublet BFs are introduced on either side of the boundaries between adjacent elements. Dummy unknowns, which are appropriately placed half-doublets, are added on external edges to retain the MoM matrix MBT property (see Section III-B2).

1) Discontinuous Galerkin Method: The DGM is commonly recognized for its ability to handle non-conformal meshes of complex targets comprising mesh elements of a wide range of electrical sizes, resulting in a significant reduction in memory consumption and solution time [32], [33], [34]. In the present contribution yet another application of the DGM is presented to retain the MBT MoM matrix $\mathbf{A}$. Quite recently, the DGM has been applied to finite array analysis [10], but not in the context of retaining the MBT property of the MoM matrix to facilitate the use of an FFT-accelerated MVP.

The essence of DGM is that current continuity is weakly enforced via an extra surface integral penalty term albeit at the cost of an increased condition number of $\mathbf{A}$ [31]. For this reason, it was proposed in [31] to stabilize the resulting DGM MoM matrix and provide practical iterative convergence with an extra boundary interior penalty stabilization function $\mathcal{I}_{\mathrm{IP}}(\beta)$

$$\mathcal{I}_{\mathrm{IP}}(\beta) = \frac{\beta}{k^2} \int_{\mathcal{C}_{pq}} [\hat{\boldsymbol{n}}^p \cdot \vec{\mathbf{f}}_t^{\,m}(\vec{\mathbf{r}})][\hat{\boldsymbol{n}}^q \cdot \vec{\mathbf{f}}_b^{\,n}(\vec{\mathbf{r}})] d\vec{\mathbf{r}}, \tag{7}$$

in which $\beta = \frac{1}{10h}$ is a scalar depending on the average electrical mesh size h, k is the wavenumber, $\vec{\mathbf{f}}_t^{\,m}$ is the m^{th} test function, $\vec{\mathbf{f}}_b^{\,n}$ is the n^{th} basis function and $\vec{\mathbf{r}}$ is a position vector along the common edge $\mathcal{C}_{pq}$ between quads p and q with in-plane outward normal unit vectors denoted as $\hat{\boldsymbol{n}}^p$ and $\hat{\boldsymbol{n}}^q$, respectively (see Fig. 2).

In the HO-ADM, exclusion of this interior boundary penalty term is paramount because including it destroys the MBT property of $\mathbf{A}$. This is due to the opposite signs of the two normal vectors $\hat{\boldsymbol{n}}^{\{p,q\}}$ when evaluated along the common edge $\mathcal{C}_{pq}$. Note that $\mathcal{I}_{\mathrm{IP}}$ is merely responsible for stabilization and that its exclusion is feasible provided proper preconditioning is employed [35], [36], [33].

2) Application of DGM in HO-ADM: With the DGM at hand, Fig. 2 illustrates how the above outlined approach is only applied at the electrically connected boundaries between array elements. More specifically, the half-doublet BFs are placed only at edges associated with two quads which lie on two different array elements. As a consequence, twice the number of doublet unknown coefficients are introduced, but only at those edges which connect different array elements.

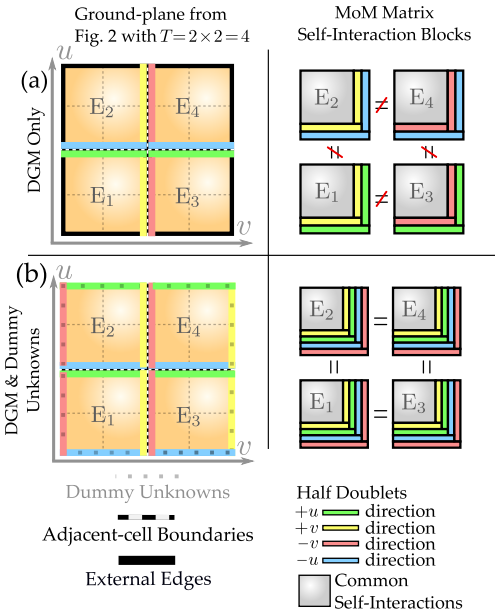

Fig. 3: Ground-plane of the array from Fig. 2 using, for illustration, $T = 2 \times 2 = 4$ elements with (a) DGM applied at differently oriented connected edges resulting in dissimilar MoM matrix self-interaction blocks and (b) with dummy BFs (half-doublets) appropriately placed at external edges in order to make self-interaction blocks equal. In this way, the full MoM matrix $\mathbf{A}$ retains its multi-level block Toeplitz property.

In the case of the patch array in Fig. 2, this means that DGM only has to be applied at the ground-plane edges. Note that this allows for normal divergence-conforming and inherently continuity-enforcing BFs between all other quads inside the array-elements.

Hence, by the use of half-doublets, the basis function coefficients can be distributed evenly between array element matrices $\mathbf{a}_{k,l}$ in $\mathbf{A}$, while the DGM maintains current continuity. The MoM matrix is, however, not yet fully BT because the array elements do not possess the same amount nor the same enumeration of BFs. Since DGM only needs to be applied at edges which connect different array elements, we focus now only on the ground-plane of the patch array of Fig. 2, which is illustrated in Fig. 3 for clarity reasons. Herein, the DGM has been used to place half-doublets on each of the connecting edges on the ground-plane between the four array elements. However, because these half-doublets are placed at differently oriented edges (indicated with colors), the resulting MoM self-interaction matrix blocks are no longer equal, despite having many basis function self-interactions in common (indicated in gray). Consequently, retaining the MBT property of $\mathbf{A}$ is not possible with the DGM alone.

3) Dummy Unknowns: To this end, a number of dummy BFs need to be added to the ground-plane on those array elements which are placed along the edges of the array. Here, one solution is to introduce half-doublets on all external edges, i.e. edges which are only associated with one quad, as illustrated in Fig. 3b. By doing so, self-interaction blocks for all array elements become equal, and the MBT property of $\mathbf{A}$ can be retained. Note that unlike the formally added unknowns $\tilde{N}$ due to the circulant extension, the additional dummy unknowns involve some overhead since they have to be computed and stored. Therefore, in the HO-ADM only strictly necessary external edges are identified on which dummy unknowns have to be placed.

Although the addition of dummy unknowns together with the DGM retains the MBT MoM matrix, the additional unknowns placed at external edges alter the Krylov subspace and subsequently the obtainable solution. It is therefore of paramount importance to exclude dummy basis function coefficients from the iterative solver. Fortunately, the technique of Section III-A can also be employed here to effectively hide dummy unknowns from the iterative solver's perspective, such that the underlying Krylov subspace remains unchanged. As such, dummy unknowns are never solved for and merely serve to preserve the MBT property of $\mathbf{A}$ for retaining a fast MVP.

After employing the DGM and adding required dummy unknowns, the total number of unknowns $N_\dagger$ can be approximated as

$$N_\dagger = [s + \kappa(s)]\, T, \tag{8}$$

where $\kappa(s) \in \{0, \ldots, s\}$ is the average number of BFs connecting two array elements. For example, if half of the BFs on an array element is electrically connected to a neighboring element $\left(\text{i.e. } \frac{\kappa(s)}{s} = 0.5\right)$, we would need 50 % more unknowns. Nevertheless, for practical antenna arrays the amount of connected edges and thus doublet BFs between array elements is considerably smaller than the number of BFs on each array element (i.e. $\kappa(s) \ll s$), hence $N_\dagger \approx N$.

In summary, by employing half-doublets only at connected boundaries between array elements (i.e. only on the ground-plane for the patch array of Fig. 2), using the DGM to enforce current continuity and by introducing dummy unknowns which are hidden from the iterative solver, electrical conduction currents are allowed to flow between array elements while retaining the MBT property of the MoM matrix, permitting an FFT-accelerated MVP.

C. Required Preconditioning Strategy

In this section, a necessary preconditioning strategy is presented in order to arrive at an effective solver for the HO-ADM in the case of connected arrays. A left-preconditioned linear system of equations is assumed, with a relative error ϵ defined as

$$\epsilon = \frac{\left\| \mathcal{P}^{-1} \left[\vec{\mathbf{b}} - \mathbf{A}\vec{\mathbf{x}}_i \right] \right\|_2}{\left\| \mathcal{P}^{-1} \vec{\mathbf{b}} \right\|_2}, \tag{9}$$

in which $\mathcal{P}$ represents a block-diagonal (BD) preconditioning matrix with ($\mathcal{P}_\text{C}$) or without ($\mathcal{P}_\text{NC}$) coupling terms from nearby array elements. Note that $\mathcal{P}$ is never formed explicitly nor applied to $\mathbf{A}$ directly.

Due to the inherent MBT structure of $\mathbf{A}$, a constant-memory block-diagonal preconditioner has been shown to be effective

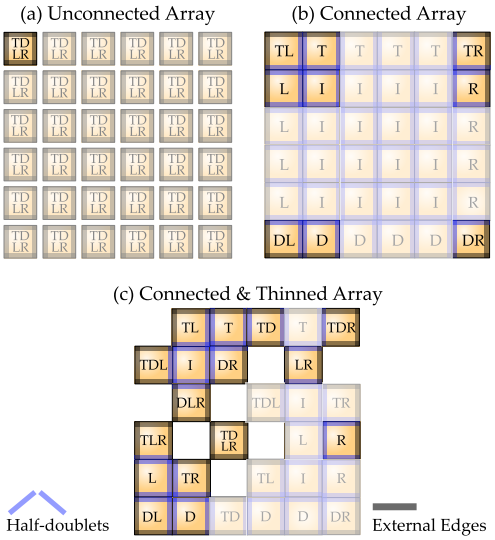

Fig. 4: Unique interaction groups required to build the constant memory NF-coupling preconditioner for the example of a 6×6 element (a) unconnected array (b) connected array and (c) connected and thinned array. DGM half-doublet BFs are placed at connected edges marked in blue. Faint colors indicate groups that do not need to be computed nor stored.

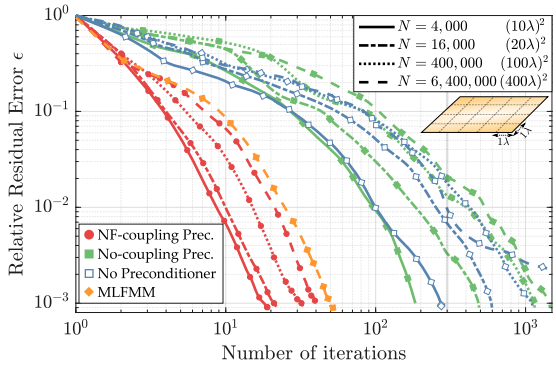

Fig. 5: Performance of the constant memory NF-coupling (CNF) preconditioner compared to the common block-diagonal preconditioner without coupling; both applied to the case of a normal-incident plane wave on ground-planes (PEC square plates) of different sizes which are constructed by electrically connecting $(1\lambda)^2$ quadrilateral mesh cells using HO-ADM. The wavelength is fixed to $1.0\,\mathrm{m}$ and the size is varied. For reference, the MLFMM result is presented only for the computationally most demanding case of the $(400\lambda)^2$ plate.

for the Array Decomposition Method [22]. Herein, an LU-factorization of the interaction matrix of a single array element is used in a BD preconditioner, which will be referred to as $\mathcal{P}_{\mathrm{NC}}$. However, in the case of connected arrays in the HO-ADM, a preconditioner not including coupling with nearby array elements no longer suffices. This is mainly due to the now closely coupled half-doublet BFs but also due to the excluded interior stabilization term $\mathcal{I}_{\mathrm{IP}}$.

1) Constant-Memory NF-Coupling Preconditioner: To overcome the bad iterative convergence when array elements become electrically connected, a NF-coupling BD preconditioner, $\mathcal{P}_{\mathrm{C}}$, is needed. Nevertheless, an inherent challenge with BD preconditioners including coupling is that each block along the main diagonal has to be stored. For the HO-ADM, doing so would mean that the preconditioner memory consumption would become proportional to the number of array elements T and even comparable to the storage of the unique interaction matrices $\mathbf{a}_{k,l}$. However, in case of regular arrays a unique set of basis function preconditioner groups can be identified as depicted in Fig. 4 for the example of an unconnected, connected and simultaneously thinned and connected 6×6 element array.

In the simple case where elements are not electrically connected, only one interaction group, comprising the self-interactions of a single array element, needs to be computed and stored as illustrated in Fig. 4a. This corresponds to the previously discussed no-coupling preconditioner $\mathcal{P}_{\mathrm{NC}}$. By realizing that redundant groups exist for connected arrays as well, we have in practice only nine unique preconditioner groups [I, T, D, L, R, TL, TR, DL, DR] as illustrated in Fig. 4b, in which letters {(I)nner, (T)op, (D)own, (L)eft, (R)ight} are used to distinguish unique interaction groups, and simultaneously indicate the positions of external edges for a given group. If we, in addition, allow array thinning, we can still identify a finite but slightly larger set of 16 unique preconditioner groups as seen in Fig. 4c. Consequently, it is possible to construct a constant-memory NF-coupling (CNF) preconditioner $\mathcal{P}_{\mathrm{C}}$ for simultaneously connected and thinned arrays, by only computing and storing at most 16 unique interaction matrices.

The CNF preconditioner $\mathcal{P}_{\mathrm{C}}$ is constructed by LU-factorization of at most 16 unique interaction matrices, whereafter they can be applied in parallel on the complete array by simple forward/backward substitutions on the associated right-hand side ($\vec{\mathbf{b}}$) entries. Remark that building the required preconditioner groups (including coupling) requires no re-computation since all interaction information is already contained in the storage of $\mathbf{a}_{k,l}$.

In Fig. 5, the relative residual error versus the number of iterations is plotted, for comparison purposes, for the simple case of plane-wave scattering from a ground-plane (i.e. square PEC plate) of various electrical sizes modeled by connecting many smaller $(1\lambda)^2$-sized plates, where λ is the wavelength. For ground-plane sizes up to around $(100\lambda)^2$, the no-coupling preconditioner $\mathcal{P}_{\mathrm{NC}}$ converges similarly as the system without preconditioning. For a $(400\lambda)^2$-ground-plane comprising 6.4 million (M) unknowns, the no-coupling preconditioner converges to a residual error of 10^{-3} after 1448 iterations, whereas no preconditioning stagnates at over 3200 iterations. Interestingly, it is noted that for all considered ground-plane sizes ranging from $(10\lambda)^2$ to $(400\lambda)^2$, the residual error starts out being significantly higher with the no-coupling preconditioner compared to not applying a preconditioner at all. Only for small ground-planes, e.g. $(10\lambda)^2$ and $(20\lambda)^2$, is the final number of iterations of the no-coupling preconditioner better than not applying any preconditioning. This impeded effectiveness of $\mathcal{P}_{\mathrm{NC}}$ makes sense if we perceive the connected array using DGM as the limiting case of unconnected array

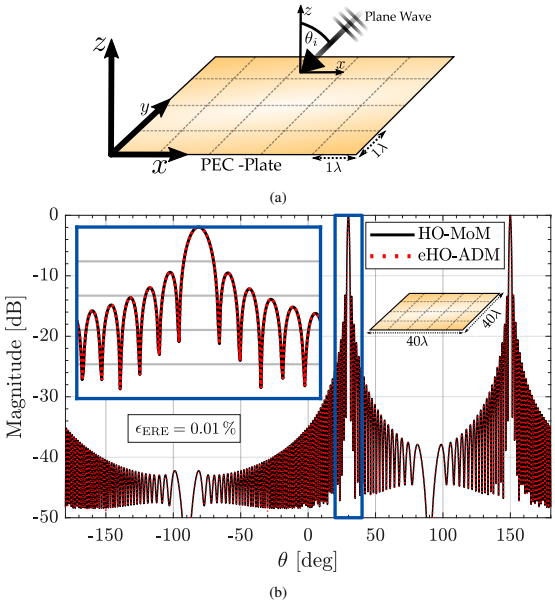

Fig. 6: Normalized scattered far-field $\phi = 180°$-cut for an obliquely incident ($\theta_i = 30°, \phi_i = 0°$) plane wave on a $(40\lambda)^2$-sized PEC square plate comparing the HO-ADM and HO-MoM. The blue marking is a view of the range $\theta = [20°, 40°]$ with the same y-axis dynamic-range as the full plot.

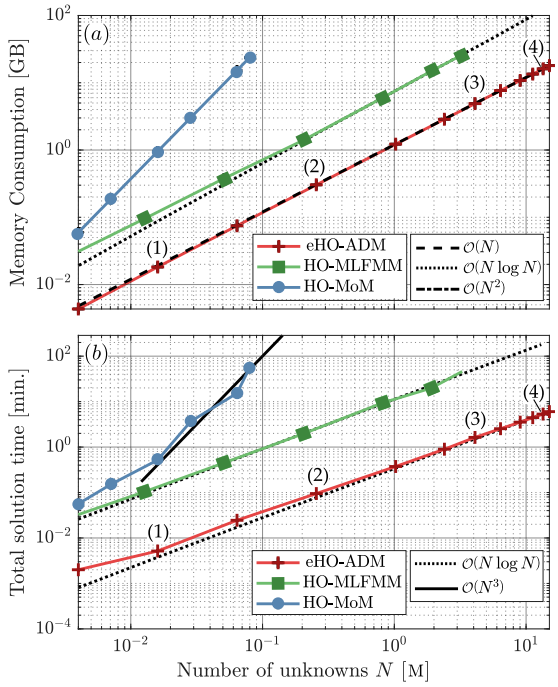

Fig. 7: Comparing HO-ADM with HO-MLFMM/HO-MoM in terms of (a) total memory consumption and (b) total solution time for the case of obliquely-incident ($\theta_i = 30°$) plane-wave scattering of various electrically large PEC plates (up to an area of $(620\lambda)^2$ corresponding to ca. 15 million unknowns). – The wavelength is fixed to 1.0 m and the size is varied. Markers do not reflect number of data points.

elements moving closer to each other, since $\mathcal{P}_{\mathrm{NC}}$ effectively assumes an uncoupled array problem.

Instead, by applying the NF-coupling preconditioner $\mathcal{P}_{\mathrm{C}}$, a residual error of 10^{-3} is reached after 17 iterations for a $(10\lambda)^2$-ground-plane compared to 185 iterations for the simple $\mathcal{P}_{\mathrm{NC}}$ preconditioner. The efficacy is even clearer for the larger $(400\lambda)^2$-ground-plane for which the number of iterations reduces from 1448 to 41 iterations by employing $\mathcal{P}_{\mathrm{C}}$. For reference, comparison with a HO-MLFMM implementation which converges after 51 iterations for the $(400\lambda)^2$-ground-plane establishes the efficacy of $\mathcal{P}_{\mathrm{C}}$. Here it should be stressed that the HO-MLFMM implementation also employs a coupling preconditioner and that HO-MLFMM uses flexible GMRES including inner and outer iterations. Therefore, to make a fair comparison with HO-MLFMM, only outer iterations have been allowed.

IV. Validation Examples

Numerical experiments are performed to demonstrate the validity and efficiency of the presented HO-ADM. Results have been generated on a computer with an Intel® Core® i7-9850H CPU @ 2.6 GHz with 6 cores and 32 GB of RAM, unless otherwise stated. The generalized minimal residual (GMRES) iterative solver is employed with Krylov subspace maximum dimension of 300 and relative residual error tolerance of 10^{-3}. Comparisons are made with the full-wave solver in ESTEAM [37] which is based on a state-of-the-art HO-MoM/MLFMM implementation [26], [38]. In the following, total solution time includes the generation of BFs, the calculation of and the block-FFT across unique interaction blocks, the preconditioner generation, and the iterative solution time. Total memory consumption refers to the storage of required matrices, the Krylov subspace, as well as the preconditioner. An Equivalent Relative Error (ERE) is used to compare HO-ADM with HO-MLFMM

$$\epsilon_{\mathrm{ERE}} = \sqrt{\frac{\sum_{i=1}^{N_s} |\mathbf{E}_{i,\mathrm{ADM}} - \mathbf{E}_{i,\mathrm{MoM/MLFMM}}|^2}{\sum_{i=1}^{N_s} |\mathbf{E}_{i,\mathrm{MoM/MLFMM}}|^2}}, \qquad (10)$$

where $\mathbf{E}_{\mathrm{ADM}}$ and $\mathbf{E}_{\mathrm{MoM/MLFMM}}$ are the electric far-field vectors for HO-ADM and HO-MoM/MLFMM, respectively. $N_s = 5403$ is the number of far-field samples used on a regular θ-ϕ-grid over the 4π far-field sphere for the examples of Section IV.

A. Plane Wave Incidence on Square Plate

As a first validation example, we continue the example of the ground-plane of Fig. 5 and consider the problem of a plane wave obliquely incident ($\theta_i = 30°, \phi_i = 0°$) on a square $(40\lambda)^2$-sized PEC plate, as depicted in Fig. 6a. The scattered far-field is plotted in Fig. 6b for a $\phi = 180°$-cut and is seen to coincide with the results of the HO-MoM within the full dynamic range (50 dB) with an equivalent relative error of

TABLE I: Total solution time and memory consumption samples from Fig. 7 for ground-planes of various sizes, comparing HO-MLFMM and HO-ADM on an Intel® Core® i7-9850H CPU @ 2.6 GHz with 6 cores. Note that separating s and T ($N = sT$) is only valid for HO-ADM.

Ground-plane Size	HO-MLFMM				HO-ADM				
	Time	Mem.	N	Iter.	Time	Mem.	s	T	Iter.
1: $(10\lambda)^2$	1.5 s	25 MB	3120	11	0.1 s	4.4 MB	40	100	18
2: $(80\lambda)^2$	118 s	1.4 GB	204,160	17	5.7 s	0.3 GB	40	6400	29
3: $(320\lambda)^2$	46 m	26 GB	3,274,240	28	98 s	4.9 GB	40	102400	40
4: $(620\lambda)^2$	-	90 GB	12,300,800	-	6 m	18 GB	40	384400	53

$0.01\,\%$. In the HO-ADM, the plate is modeled as many $(1\lambda)^2$-sized connected elements (see Fig. 6a) and by applying the DGM with dummy unknowns as described in Section III-B.

In Fig. 7 the total solution time and memory consumption is plotted, including theoretical asymptotic scaling, comparing HO-MoM/MLFMM and the HO-ADM for increasingly larger plates. Note that the wavelength is fixed to $1.0\,\mathrm{m}$ and the size is varied. Selected samples (marked with numbers in parenthesis in Fig. 7) have been tabulated in Table I. Herein it is evident that HO-ADM is more than an order of magnitude faster than the HO-MLFMM in terms of total solution time in the whole span from $N = 4,000$ to $N = 15\,\mathrm{M}$ unknowns. For PEC plates smaller than $(80\lambda)^2$ corresponding to $N = 256,000$ unknowns, the total solution time of the HO-ADM does not follow the theoretical asymptotic scaling because it is dominated by the overhead associated with the special DGM and dummy unknowns handling.

For a larger $(320\lambda)^2$ PEC plate, the HO-ADM requires circa $N = 4\,\mathrm{M}$ unknowns and uses $98\,\mathrm{s}$ with $5\,\mathrm{GB}$ of total memory consumption whereas MLFMM requires around $N = 3.2\,\mathrm{M}$ unknowns but uses $46\,\mathrm{min}$ with a memory consumption of $26\,\mathrm{GB}$. For the largest $(620\lambda)^2$ PEC plate ($N \approx 15\,\mathrm{M}$), HO-ADM uses a total simulation time of around $6\,\mathrm{min}$, and a memory consumption of $18\,\mathrm{GB}$, whereas HO-MLFMM would require $90\,\mathrm{GB}$ and could not be run on the computer at hand.

B. Phased Patch Antenna Array

As a second example, we consider a 32×32-element dual-frequency right-hand circularly polarized (RHCP) high-gain antenna array based on the design from [39] with 1024 independent wire excitations, which is illustrated in Fig. 8a including the employed simulation mesh. The array is meshed with a total of $122{,}880$ quadrilaterals comprising $N = 975{,}000$ unknowns in the HO-MLFMM, whereas $N \approx 1\,\mathrm{M}$ unknowns are needed in the HO-ADM due to the DGM and dummy unknowns as described in Section III-B.

The radiated far-field pattern in Fig. 9a has been computed at $8.4\,\mathrm{GHz}$, and the peak directivity for both HO-ADM and HO-MLFMM is $38.4\,\mathrm{dBi}$ (which is close to the reported calculated directivity of $38.5\,\mathrm{dBi}$ [39] considering that not all design parameters are known). In Fig. 9a both the co- and cross-polarization patterns are seen to coincide comparing the HO-ADM with HO-MLFMM, with an equivalent relative error of $0.03\,\%$ and $0.05\,\%$ for co-pol and cx-pol, respectively.

Table II shows a comparison of solution time and memory consumption between the HO-ADM and ESTEAM. For HO-MLFMM the solution time is around 1 hour with a memory consumption of only $25.1\,\mathrm{GB}$. At the penalty of slightly increased memory consumption ($28.2\,\mathrm{GB}$) using the extended HO-ADM, the solution time can be reduced by a factor of 10 to around 6 min. Both HO-MLFMM and HO-ADM use around half of the total solution time to setup matrices and the other half to solve the system, and both use approximately the same order of iterations. The ten-fold reduction in solution time for HO-ADM is observed both in terms of setup time and time per iteration.

Whereas a speed-up by a factor of 30 is possible in the case of an electrically large PEC plate constructed by simple flat quads, a speed-up by a factor of only 10 is achievable for the 32×32 array. The main reason is the quadratic com-

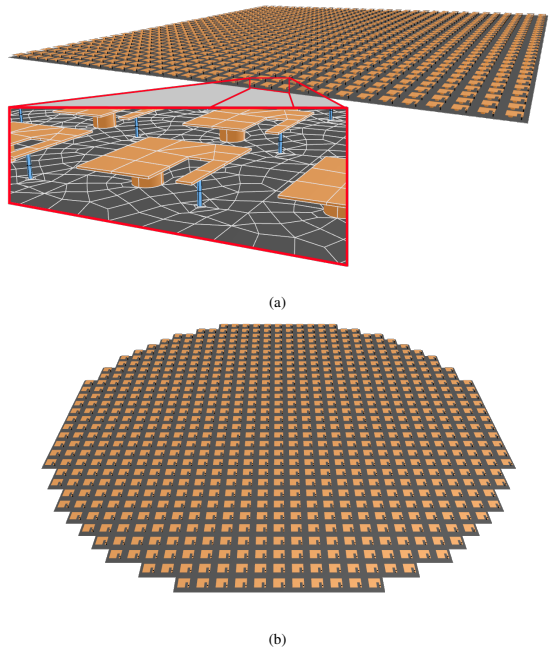

(a)

(b)

Fig. 8: (a) 32×32-element dual-frequency right-hand circularly polarized all-metal high-gain antenna array, including employed meshing of the element cell for the reported results. – White lines indicate edges of the mesh, blue signify wire-quads, dark gray quads designate the ground-plane and orange illustrate quads on the radiating elements. (b) Thinned 793-element all-metal array conforming to a circular rim.

TABLE II: Total solution time and memory consumption for the 32×32 array in Fig. 8a and the corresponding circular-thinned array in Fig. 8b, comparing HO-MLFMM and HO-ADM on an Intel® Core® i9-10980XE CPU @ 3.0 GHz with 18 cores. Results in parentheses are for the thinned array.

Method	Total Simulation Time	Memory Consumption	Number of Iterations	Time per Iteration
HO-MoM	N/A	3540 GB	N/A	N/A
HO-MLFMM	1 h 2 min (57 min)	25.1 GB (22.5 GB)	540 (567)	3.9 s (3.8 s)
HO-ADM	6 min 18 s (6 min 18 s)	28.2 GB (28.2 GB)	481 (506)	0.4 s (0.38 s)

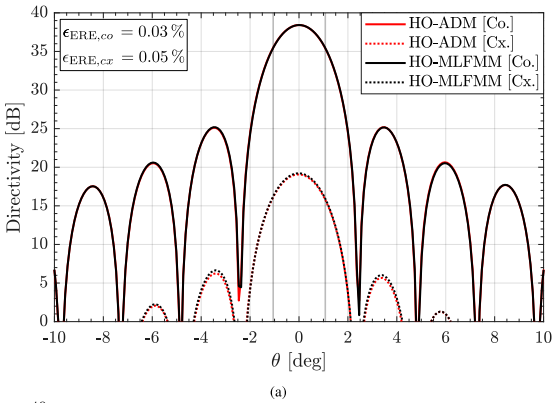

(a)

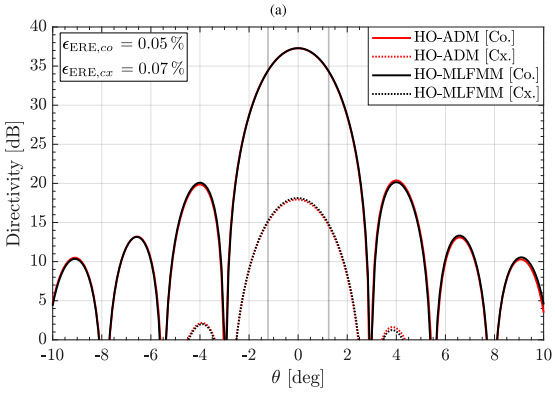

(b)

Fig. 9: Far-field directivity pattern ($\phi = 0°$-cut) at 8.4 GHz comparing the HO-ADM to the HO-MLFMM for (a) the antenna of Fig. 8a (b) the thinned array of Fig. 8b. Co-polarization is RHCP whereas the cross-polarization is LHCP. 3.0 dB-beamwidths are marked with dark-gray vertical lines.

putational complexity scaling in s (number of basis functions per array element), which impacts both the memory $\mathcal{O}(s^2T)$ and computational complexity $\mathcal{O}(s^2T \log T)$ for HO-ADM. Here it should be noted that the asymptotic total computational complexity and memory scaling of MLFMM is $\mathcal{O}(sT \log sT)$. For a fixed array element discretization, s can be considered constant, hence the memory consumption of HO-ADM will become smaller than that of HO-MLFMM for larger arrays. While the computational complexity remains the same between HO-ADM and HO-MLFMM, they differ significantly in their respective computational complexity constants. The break-even value of s is strongly problem-dependent; that is, it varies significantly with the complexity of the individual elements and how many array elements are considered. From our investigations, we found that the asymptotic break-even point, s_∞ for $T \to \infty$ (infinite number of array elements) is on average in the order of 4000 but can vary from 1000 to 10000 and even higher.

C. Circular Rim Patch Antenna Array

The third example takes outset in the same 32×32-element array but assuming it needs to conform to a circular rim. To this end, the antenna array needs to be thinned which is achieved in HO-ADM as described in Section III-A. The resulting 793-element array is depicted in Fig. 8b, and is meshed with a total of 92,323 quadrilaterals comprising $N = 755{,}370$ unknowns in the HO-MLFMM, whereas 18,312 (2.4 %) additional unknowns are needed in the HO-ADM due to the DGM and dummy unknowns.

The radiated far-field pattern has been computed at 8.4 GHz and is shown in Fig. 9b with an equivalent relative error of 0.05 % and 0.07 % for co-pol and cx-pol, respectively. As anticipated for a smaller aperture, the peak-directivity is 1.1 dB smaller at 37.3 dB, and the first side-lobe level at 19.9 dB is close to a uniformly excited circular aperture. The 3 dB beamwidth is only 0.2° larger for the thinned array compared to the full 32×32 array.

Solution time and memory consumption in the case of the circular-thinned antenna array can be found in Table II enclosed in parentheses. Whereas the HO-MLFMM uses 57 min, the total solution time for the HO-ADM in case of the thinned array is unaltered at 6 min and 18 s. Firstly, this is because all matrix blocks $\mathbf{a}_{k,l}$ need to be computed and stored in the HO-ADM regardless of the number of thinned elements in the array. Secondly, for this particular case, the slightly faster MVP compensates for the additional iterations which are needed due to the employed preconditioner being less effective for the circular-thinned array.

V. Conclusion

We presented two extensions to the Higher-Order Array Decomposition Method enabling it to handle thinned and connected arrays of antennas or scatterers. The Discontinuous Galerkin Method (DGM) for surface integral equations has been employed together with appropriately placed dummy unknowns to retain the FFT-accelerated matrix-vector product even for connected arrays.

The presented method significantly reduces the solution time by more than an order of magnitude for both a 32×32-element square array and a 793-element circular-thinned array. This improvement in speed is achieved without approximations and without significantly increasing memory consumption compared to existing fast methods like the MLFMM.

We note that future work includes an extension to the presented method enabling the simulation of non-identical array elements, by exploiting the same technique as described in Section III-A.

Acknowledgment

The authors would like to thank the anonymous reviewers for their valuable comments and suggestions.

References

[1] R. Coifman, V. Rokhlin, and S. Wandzura, "The fast multipole method for the wave equation: A pedestrian prescription," *IEEE Antennas and Propagation Magazine*, vol. 35, no. 3, pp. 7–12, 1993.

[2] C.-C. Lu and W. C. Chew, "A multilevel algorithm for solving a boundary integral equation of wave scattering," *Microwave and Optical Technology Letters*, vol. 7, no. 10, pp. 466–470, 1994.

[3] J. Song, C.-C. Lu, and W. C. Chew, "Multilevel fast multipole algorithm for electromagnetic scattering by large complex objects," *IEEE Transactions on Antennas and Propagation*, vol. 45, no. 10, pp. 1488–1493, 1997.

[4] X. Zhao, Z. Lin, Y. Zhang, S.-W. Ting, and T. K. Sarkar, "Parallel hybrid method of HOMoM–MLFMA for analysis of large antenna arrays on an electrically large platform," *IEEE Transactions on Antennas and Propagation*, vol. 64, no. 12, pp. 5501–5506, 2016.

[5] B. Karaosmanoğlu and Ö. Ergül, "Acceleration of MLFMA simulations using trimmed tree structures," *IEEE Transactions on Antennas and Propagation*, vol. 69, no. 1, pp. 356–365, 2020.

[6] W. B. Lu, T. J. Cui, and H. Zhao, "Acceleration of fast multipole method for large-scale periodic structures with finite sizes using sub-entire-domain basis functions," *IEEE Transactions on Antennas and Propagation*, vol. 55, no. 2, pp. 414–421, 2007.

[7] V. Prakash, , and R. Mittra, "Characteristic basis function method: A new technique for efficient solution of method of moments matrix equations," *Microwave and Optical Technology Letters*, vol. 36, no. 2, pp. 95–100, 2003.

[8] E. Lucente, A. Monorchio, and R. Mittra, "An iteration-free MoM approach based on excitation independent characteristic basis functions for solving large multiscale electromagnetic scattering problems," *IEEE Transactions on Antennas and Propagation*, vol. 56, no. 4, pp. 999–1007, 2008.

[9] L. Matekovits, V. A. Laza, and G. Vecchi, "Analysis of large complex structures with the synthetic-functions approach," *IEEE Transactions on Antennas and Propagation*, vol. 55, no. 9, pp. 2509–2521, 2007.

[10] W. Xiang, W. Yang, and W. Lu, "Fast sub-entire-domain basis functions method for analysis of composite finite periodic structures with dielectric-conductor cells," *IEEE Antennas and Wireless Propagation Letters*, 2022.

[11] S. Kapur and D. E. Long, "IES3: a fast integral equation solver for efficient 3-dimensional extraction." in *ICCAD*, vol. 97, 1997, pp. 448–455.

[12] S. M. Seo and J.-F. Lee, "A single-level low rank IE-QR algorithm for PEC scattering problems using EFIE formulation," *IEEE Transactions on Antennas and Propagation*, vol. 52, no. 8, pp. 2141–2146, 2004.

[13] S. Kurz, O. Rain, and S. Rjasanow, "The adaptive cross-approximation technique for the 3d boundary-element method," *IEEE Transactions on Magnetics*, vol. 38, no. 2, pp. 421–424, 2002.

[14] Q. Gueuning, E. D. L. Acedo, A. K. Brown, and C. Craeye, "An inhomogeneous plane-wave based single-level fast direct solver for the scattering analysis of extremely large antenna arrays," *IEEE Transactions on Antennas and Propagation*, 2022.

[15] W. Yu, H. Yang, S. Li, and Y. Xu, "An HSS-matrix-based fast direct solver with randomized algorithm," *The Applied Computational Electromagnetics Society Journal*, pp. 814–817, 2018.

[16] E. Bleszynski, M. Bleszynski, and T. Jaroszewicz, "AIM: Adaptive integral method for solving large-scale electromagnetic scattering and radiation problems," *Radio Science*, vol. 31, no. 5, pp. 1225–1251, 1996.

[17] S. Sharma and P. Triverio, "AIMx: an extended adaptive integral method for the fast electromagnetic modeling of complex structures," *IEEE Transactions on Antennas and Propagation*, vol. 69, no. 12, pp. 8603–8617, 2021.

[18] J. White, J. Phillips, and T. Korsmeyer, "Comparing precorrected-FFT and fast multipole algorithms for solving three-dimensional potential integral equations,"," in *Proceedings of the Colorado Conference on Iterative Methods*. Citeseer, 1994, pp. 4–10.

[19] S. M. Seo and J.-F. Lee, "A fast IE-FFT algorithm for solving PEC scattering problems," *IEEE Transactions on Magnetics*, vol. 41, no. 5, pp. 1476–1479, 2005.

[20] S.-C. Lee, M. N. Vouvakis, and J.-F. Lee, "A non-overlapping domain decomposition method with non-matching grids for modeling large finite antenna arrays," *Journal of Computational Physics*, vol. 203, no. 1, pp. 1–21, 2005.

[21] Z. Peng, X.-C. Wang, and J.-F. Lee, "Integral equation based domain decomposition method for solving electromagnetic wave scattering from non-penetrable objects," *IEEE Transactions on Antennas and Propagation*, vol. 59, no. 9, pp. 3328–3338, 2011.

[22] R. W. Kindt, K. Sertel, E. Topsakal, and J. L. Volakis, "Array decomposition method for the accurate analysis of finite arrays," *IEEE Transactions on Antennas and Propagation*, vol. 51, no. 6, pp. 1364–1372, 2003.

[23] E. H. Bleszynski, M. K. Bleszynski, and T. Jaroszewicz, "Block-Toeplitz fast integral equation solver for large finite periodic and partially periodic array systems," *IEICE Transactions on Electronics*, vol. 87, no. 9, pp. 1586–1594, 2004.

[24] R. W. Kindt and J. L. Volakis, "Array decomposition-fast multipole method for finite array analysis," *Radio Science*, vol. 39, no. 2, pp. 1–9, 2004.

[25] M. Brandt-Møller, M. Mattes, O. Breinbjerg, M. Zhou, and O. Borries, "Array decomposition method for arbitrary-element regular arrays using higher-order basis functions," *IEEE Antennas and Wireless Propagation Letters*, 2022.

[26] E. Jørgensen, J. L. Volakis, P. Meincke, and O. Breinbjerg, "Higher order hierarchical Legendre basis functions for electromagnetic modeling," *IEEE Transactions on Antennas and Propagation*, vol. 52, no. 11, pp. 2985–2995, 2004.

[27] R. D. Graglia, D. R. Wilton, and A. F. Peterson, "Higher order interpolatory vector bases for computational electromagnetics," *IEEE Transactions on Antennas and Propagation*, vol. 45, no. 3, pp. 329–342, 1997.

[28] E. Jørgensen, *Higher-order integral equation methods in computational electromagnetics*. Ørsted-DTU, PhD Dissertation, 2003.

[29] G. H. Golub and C. F. Van Loan, *Matrix computations*. JHU Press, 1996.

[30] "IEEE standard for definitions of terms for antennas," pp. ix+38, 2014.

[31] Z. Peng, K.-H. Lim, and J.-F. Lee, "A discontinuous Galerkin surface integral equation method for electromagnetic wave scattering from non-penetrable targets," *IEEE Transactions on Antennas and Propagation*, vol. 61, no. 7, pp. 3617–3628, 2013.

[32] Z. Peng, R. Hiptmair, Y. Shao, and B. MacKie-Mason, "Domain decomposition preconditioning for surface integral equations in solving challenging electromagnetic scattering problems," *IEEE Transactions on Antennas and Propagation*, vol. 64, no. 1, pp. 210–223, 2015.

[33] X.-W. Huang, M.-L. Yang, and X.-Q. Sheng, "A simplified discontinuous Galerkin self-dual integral equation formulation for electromagnetic scattering from extremely large IBC objects," *IEEE Transactions on Antennas and Propagation*, vol. 70, no. 5, pp. 3575–3586, 2021.

[34] V. F. Martin, D. M. Solis, M. G. Araujo, L. Landesa, F. Obelleiro, and J. M. Taboada, "A discontinuous galerkin integral equation approach for electromagnetic modeling of realistic and complex radiating systems," *IEEE Transactions on Antennas and Propagation*, pp. 1–1, 2023.

[35] B.-B. Kong and X.-Q. Sheng, "A discontinuous Galerkin surface integral equation method for scattering from multiscale homogeneous objects," *IEEE Transactions on Antennas and Propagation*, vol. 66, no. 4, pp. 1937–1946, 2018.

[36] V. F. Martín, L. Landesa, F. Obelleiro, and J. M. Taboada, "A discontinuous Galerkin combined field integral equation formulation for electromagnetic modeling of piecewise homogeneous objects of arbitrary shape," *IEEE Transactions on Antennas and Propagation*, vol. 70, no. 1, pp. 487–498, 2021.

[37] TICRA, "TICRA Tools ESTEAM," https://www.ticra.com/software/esteam/, 2019.

[38] O. Borries, P. Meincke, E. Jørgensen, S. B. Sørensen, and P. C. Hansen, "Improved multilevel fast multipole method for higher-order discretizations," *European Conference on Antennas and Propagation*, pp. 3610–3614, 2014.

[39] N. Chahat, B. Cook, H. Lim, and P. Estabrook, "All-metal dual-frequency RHCP high-gain antenna for a potential europa lander," *IEEE Transactions on Antennas and Propagation*, vol. 66, no. 12, pp. 6791–6798, 2018.

Magnus Brandt-Møller was born in Hvidovre, Denmark, in 1995. He received the B.Sc. and M.Sc. degrees in electrical engineering from the Technical University of Denmark (DTU), Lyngby, in 2017 and 2020, respectively. He is currently pursuing the Ph.D. degree at the Technical University of Denmark, focusing on the full-wave numerical modeling of electrically large finite-array structures. His research interest include computational electromagnetics, antenna theory, and analysis and design techniques for phased array antennas.

Conference Paper I

Performance of Array Decomposition Method with Higher-Order Basis Functions

Magnus Brandt-Møller, Michael Mattes,
Olav Breinbjerg, Min Zhou, Oscar Borries

Status: Published

Bibliography

Performance of Array Decomposition Method with Higher-Order Basis Functions

Magnus Brandt-Møller*‡, Michael Mattes*, Olav Breinbjerg†, Min Zhou‡, Oscar Borries‡
*EMS, Technical University of Denmark, Kgs. Lyngby, Denmark, {magbran,mmattes}@elektro.dtu.dk
†ElMaReCo, Copenhagen, Denmark, olavbreinbjerg@outlook.com
‡TICRA, Copenhagen, Denmark, {mbm, mz,ob}@ticra.com

***Abstract*—The performance of the Array Decomposition Method for finite regular antenna arrays with arbitrary identical elements using higher order basis functions is investigated. We demonstrate how using higher-order basis functions, which drastically reduce the number of basis functions per array element, results in significantly reduced simulation time for a $10 \times 10\,(22\lambda \times 22\lambda)$ circular horn array.**

***Index Terms*—antennas, finite array, higher-order basis functions, block Toeplitz solver**

I. Introduction

TRADITIONALLY, antenna arrays have been employed in radar applications, radio astronomy and as feeds for reflector based systems. For such applications, traditional design approaches based on embedded element patterns and array factors or variants thereof have sufficed. With the on-going move from large spacecrafts in the geostationary orbit (GEO) to smaller spacecrafts in low earth orbits (LEO), as well as an increasing demand for flexible in-orbit configurations, direct radiating arrays (DRA) are employed more frequently for space missions. DRA commonly comprise densely packed elements which in turn demands more accurate modelling of edge and mutual coupling effects. In addition, stringent performance requirements in space substantiates the necessity of rigorous full-wave numerical methods.

Conventional full-wave methods, e.g. the Method of Moments (MoM), suffer from excessive memory requirement and computational complexity, $\mathcal{O}(N^2)$ and $\mathcal{O}(N^2) - \mathcal{O}(N^3)$ respectively, where N is the number of unknowns.

Several iterative methods have been proposed for the solution of electrically large arrays, in which the memory and computational requirement is $\mathcal{O}(N \log N)$. Examples include the Multi-Level Fast Multipole Method (MLFMM) [1], the Adaptive Integral Method (AIM) [2] and the pre-corrected fast Fourier transform (pFFT) [3]. While these methods accelerate the analysis of general arrays, it has been shown that exploiting the geometry of regular antenna arrays significantly reduce both memory requirement and computation time [4].

The present work concerns the MoM solution of electrically large antennas arrays with arbitrarily shaped, regularly spaced, identical and perfectly electrically conducting identically oriented elements, a common configuration for modern antenna arrays. The translational invariance of the associated Greens function, together with the regular geometrical structure of the array results in a block-Toeplitz matrix [5] which allows for a Fast Fourier Transform (FFT)-accelerated matrix-vector product (MVP) [4], [6] in the iterative solution, using the Array Decomposition Method (ADM).

ADM scales as the square of the number of basis functions per array element [6]. It is therefore paramount to keep the number of basis functions as low as possible for a fixed solution accuracy. Several approaches to reduce the sensitivity of ADM to increasing number of basis functions have been proposed [4], [7]; however, they are based on approximations, which may impact solution accuracy.

We demonstrate how the number of basis functions per array element can be reduced using higher-order (HO) basis functions [8]. Consequently, used in combination with ADM, a significant reduction in computation time can be achieved. To demonstrate this, the HO-ADM is applied to a $10 \times 10\,(22\lambda \times 22\lambda)$ circular horn array, resulting in much lower computation times compared to the ADM using first-order basis functions, without the need for approximations.

II. The Array Decomposition Method

This section is a distilled version of ADM [4], for the purpose of understanding ADM's quadratic scaling in number of basis functions per array element. We take outset in an arbitrary $p \times q$ element planar array, and write the total number of unknowns as $N = ST$, where S is the total number of unknowns per array element, and $T = p \times q$ is the total number of array elements.

Since the MVP with a (circulantly extended) block-Toeplitz matrix is equivalent to a convolution operation on the blocks, the MVP can be accelerated by the FFT. However, the individual matrix blocks of size $S \times S$ do not, in general, possess any special symmetry, and can therefore not be accelerated by the FFT. Thus, ADM scales computationally as $\mathcal{O}(S^2 T \log(T))$.

Moreover, in order to perform the MVP, ADM needs to store $(2p-1) \times (2q-1)$ blocks of size $S \times S$, resulting in an asymptotic memory scaling of $\mathcal{O}(S^2 T)$. With this asymptotic scaling, it is critical to keep S as low as possible without impacting solution accuracy. This can be achieved using higher-order basis functions. In this work, an ADM implementation using the higher-order hierarchical Legendre basis functions from [8] is used.

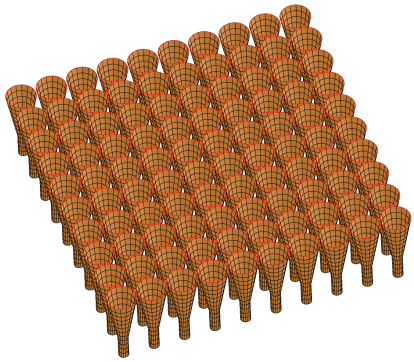

Fig. 1: $10\times10\,(22\lambda \times 22\lambda)$ element circular horn array.

III. Results

We consider a direct radiating 10×10 $(22\lambda \times 22\lambda)$ array (Fig. 1) which consists of circular horn antennas fed by circular waveguides excited with the fundamental TE_{11} mode. The radiated far-field patterns have been calculated using HO-ADM on a computational machine with an Intel®Xeon®5218 CPU @ 2.3 GHz with 16 cores. A reference solution has been generated using the smallest mesh length possible on the available system. For fixed basis function order p, the maximal admissible mesh length has been varied between 0.15λ and 1.5λ to ensure an RMS error in the radiated far-field forward hemisphere that is less than $1\,\%$ (far-field requirement).

Fig. 2 (a) shows the total computation time (including initialisation) and memory usage (b), for different fixed BF orders p. For each order p, the maximal admissible mesh length has been decreased until reaching the far-field requirement (or lower). For $p = 1$, a total of 288,400 mesh cells ($\approx 0.15\lambda$) are needed to converge to the far-field requirement, which is considerably more than the 54,000 mesh cells ($\approx 0.3\lambda$) needed for $p = 2$. The high number of mesh cells for $p = 1$ results in high ADM initialisation time, primarily due to the increased number of integrals to compute.

The significant difference in computation time from 220 min. ($p = 1$) to 25 min. ($p = 2$) can be explained primarily by the decrease in the number of mesh cells. Notably, due to meshing constraints, the mesh is more refined for $p = 2$ and $p = 3$, resulting in a two and four times lower RMS error, respectively, than the solution for $p = 1$ and $p = 4$. The increased accuracy is the primary reason for the relatively small decrease in total number of unknowns, memory and computation time from $p = 2$ to $p = 3$.

Overall, the results clearly demonstrate superior performance when increasing the basis function order. This is most clearly seen in the transition from $p = 1$ and $p = 2$, where the total computation time decreases by a factor of 9, the memory decreases by a factor of two, even while the RMS error is halved.

IV. Conclusion

A reduction in required memory and computation time for simulation of regular arrays has been demonstrated. This

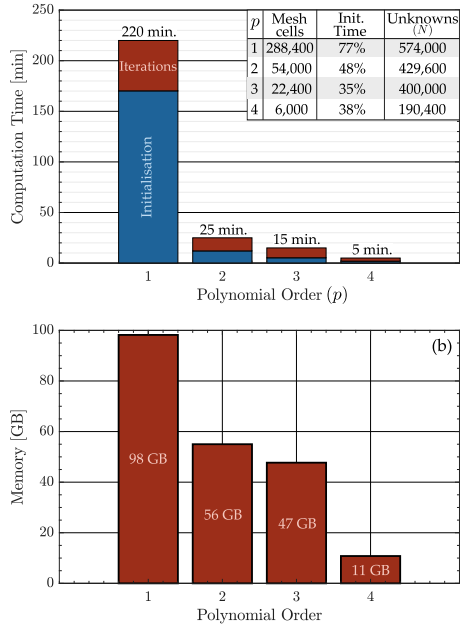

p	Mesh cells	Init. Time	Unknowns (N)
1	288,400	77%	574,000
2	54,000	48%	429,600
3	22,400	35%	400,000
4	6,000	38%	190,400

Fig. 2: Total simulation time (a) and memory usage (b) for HO-ADM required to reach $< 1\,\%$ far-field RMS error.

is achieved by means of the Array Decomposition Method used in conjunction with higher order basis functions. It is, to the best of the authors' knowledge, the first time such a combination has been implemented. The results show that using this approach, the memory and computation time savings in the order of 9 and 44 times, respectively, can be achieved compared to traditional first-order basis function implementations.

References

[1] O. Borries, P. Meincke, E. Jørgensen, S. B. Sørensen, and P. C. Hansen, "Improved multilevel fast multipole method for higher-order discretizations," *EuCAP*, pp. 3610–3614, 2014.

[2] E. Bleszynski, M. Bleszynski, and T. Jaroszewicz, "Aim: Adaptive integral method for solving large-scale electromagnetic scattering and radiation problems," *Radio Sci.*, vol. 31, no. 5, pp. 1225–1251, 1996.

[3] J. White, J. Phillips, and T. Korsmeyer, "Comparing precorrected-fft and fast multipole algorithms for solving three-dimensional potential integral equations," pp. 4–10, 1994.

[4] R. W. Kindt and J. L. Volakis, "Array decomposition-fast multipole method for finite array analysis," *Radio Sci.*, vol. 39, no. 2, pp. 1–9, 2004.

[5] A. Geranmayeh, W. Ackermann, and T. Weiland, "FFT accelerated marching-on-in-order methods," pp. 511–514, 2008.

[6] E. H. Bleszynski, M. K. Bleszynski, and T. Jaroszewicz, "Block-toeplitz fast integral equation solver for large finite periodic and partially periodic array systems," *IEICE Trans. Electron.*, vol. 87, no. 9, pp. 1586–1594, 2004.

[7] R. Kindt, K. Sertel, E. Topsakal, and J. L. Volakis, "An extension of the array decomposition method for large finite-array analysis," *Microw. Opt. Technol. Lett.*, vol. 38, no. 4, pp. 323–328, 2003.

[8] E. Jørgensen, J. L. Volakis, P. Meincke, and O. Breinbjerg, "Higher order hierarchical Legendre basis functions for electromagnetic modeling," *IEEE Trans. Antennas Propag.*, vol. 52, no. 11, pp. 2985–2995, 2004.

Conference Paper II

Higher-Order Array Decomposition Method for Array Antennas with Connected Elements

Magnus Brandt-Møller, Michael Mattes, Olav Breinbjerg, Min Zhou, Erik Jørgensen

Status: Published

Bibliography

Higher-Order Array Decomposition Method for Array Antennas with Connected Elements

Magnus Brandt-Møller[(1)(3)], Michael Mattes[(1)], Olav Breinbjerg[(2)], Min Zhou[(3)], and Erik Jørgensen[(3)]

[(1)] EMS, Technical University of Denmark, Kgs. Lyngby, Denmark, {magbran, mmattes}@elektro.dtu.dk
[(2)] ElMaReCo, Copenhagen, Denmark, olavbreinbjerg@outlook.com
[(3)] TICRA, Copenhagen, Denmark, {mbm, mz, ej}@ticra.com

***Abstract*—The Higher-Order Array Decomposition Method (HO-ADM) is extended to handle regular array antennas with interconnected elements. The Discontinuous Galerkin Method (DGM) is used to retain the multi-level block-Toeplitz Method of Moments (MoM) matrix structure, even for connected elements. The presented method yields more than an order of magnitude reduced solution time for a 8×8 real-world antenna array and similar memory consumption compared to existing fast methods.**

I. Introduction

Future array antennas will include a huge number of densely packed elements, resulting in electrically massive structures with strong edge effects and mutual coupling occurring. To accurately take into account these effects for electrically large arrays, traditional methods such as the embedded element pattern approach no longer suffice.

When analyzing arrays by solving surface integral equations (SIE) using the full-wave Method of Moments (MoM), all mutual coupling and edge effects are taken into account. This is nevertheless at the expense of a computational complexity and memory consumption which scales as $\mathcal{O}(N^2)$ and $\mathcal{O}(N^2) - \mathcal{O}(N^3)$, respectively, where N is the number of unknowns. By means of error-controllable approximations, various effective full-wave analysis techniques have been proposed, in which memory consumption and computational complexity can be reduced to as low as $\mathcal{O}(N \log N)$.

Widely used examples include the Multi-Level Fast Multipole Method (MLFMM) [1], the Adaptive Integral Method (AIM) [2], and the pre-corrected fast Fourier transform (pFFT) [3], the latter two require projection of BFs on a regular grid. For Macro-Basis Function (MBF) based methods [4], [5], the generation and number of MBFs to include is problem specific and the error cannot be controlled a priori.

When array elements are placed on a regular lattice the computation efficiency can be improved without compromising accuracy by employing the Array Decomposition Method (ADM) [6]. Recently, the boundary integral part of ADM has been implemented with higher-order (HO) basis functions and shown to use significantly less unknowns for a given accuracy [7]. Nevertheless, a restriction in the HO-ADM has been that no conduction current was allowed between elements, i.e. that elements could not be connected, effectively excluding arrays with a ground-plane or other interconnecting features. In this paper the existing HO-ADM has been extended, enabling it to handle electrically connected arrays.

II. HO-ADM with Connected Elements

The HO-ADM makes use of consecutively ordered HO basis functions (BFs), the regular arrangement of array elements, as well as the translational invariance of the 3D free-space Green function, to enable an FFT-accelerated matrix-vector product (MVP) used in the iterative solution procedure. This acceleration is only possible due to the resulting multi-level block-Toeplitz (MBT) MoM matrix $\mathbf{A}$. In case of electrically connected array elements this Toeplitz property is lost because the BF coefficients on connecting edges have to be associated with either one or the other array element. In the present contribution, the Discontinous Galerkin Method (DGM) [8] for surface integral equations is employed to keep the MBT property of $\mathbf{A}$. Consequently, the MVP can be FFT-accelerated in the case of connected array elements.

More specifically, the DGM is employed to split the roof-top BFs into half roof-tops at edges associated with two mesh-cells which belong to two different array elements. As a consequence, twice the number of BF coefficients are needed at connecting edges, but they can now be distributed evenly between array element interaction-matrix blocks in $\mathbf{A}$. To make $\mathbf{A}$ fully block-Toeplitz, however, a number of dummy BF need to be added to the array unit cell. These are half roof-tops but are placed on all external edges, i.e. edges which are only associated with a single mesh-cell. By doing so, self-interaction blocks for all array elements become equal, which in turn means that the MBT property of $\mathbf{A}$ is retained.

It should be noted that placing additional dummy unknowns at external edges changes the Krylov subspace and therefore also the obtained solution. However, by hiding the dummy BFs from the iterative solver, which is done by zeroing appropriate entries in the residual vector calculation, the solution is unchanged. As such, dummy unknowns are never solved for and merely serve to preserve the MBT property of $\mathbf{A}$ in order to accelerate the MVP using the FFT.

In summary, by splitting roof-tops into half roof-tops using the DGM to enforce current continuity and by introducing dummy unknowns, which are hidden from the iterative solver, electrical conduction currents are now allowed to flow between array elements in the extended HO-ADM.

III. Application Example

As a validation case, we consider an 8×8-element dual-frequency right-hand circularly polarized (RHCP) high-gain antenna sub-array based on the design in [9] (Fig. 1) with

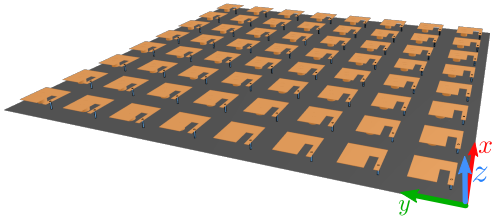

Fig. 1. 8×8-element (area of $28.5\lambda^2$) dual-frequency right-hand circularly polarized (RHCP) high-gain antenna sub-array from [9], with radiation pattern coordinate system.

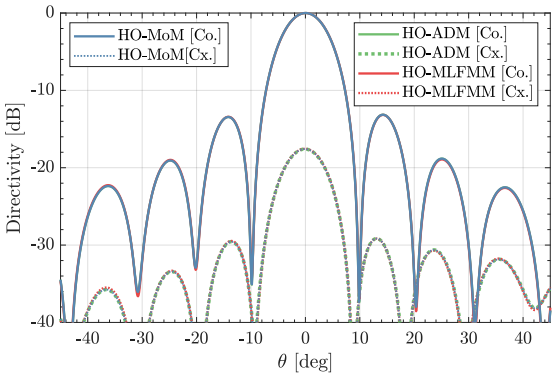

Fig. 2. Normalized far-field directivity pattern ($\phi = 0°$-cut) for the sub-array in Fig. 1 at 8.425 GHz, comparing the extended HO-ADM to HO-MLFMM and HO-MoM. Co-polarization is RHCP whereas the cross-polarization is LHCP.

64 independent wire excitations. The sub-array is meshed with a total of 7,552 quadrilaterals comprising $N = 60{,}832$ unknowns in the HO-MLFMM/HO-MoM, while $N = 62{,}464$ unknowns are needed in the HO-ADM due to the DGM and dummy unknowns as described in Section II.

The radiated far-field pattern in Fig. 2 has been computed at 8.425 GHz on a laptop with an Intel® Core® i7-9850H CPU @ 2.6 GHz with 6 cores. Comparisons are made with the full-wave solver in ESTEAM [10] which is based on a state-of-the-art HO-MoM/MLFMM implementation. The calculated peak directivity for all methods is 26.07 dB, which is close to the reported measured directivity of 26 dB [9]. In Fig. 2, both the co- and cross-polarization $\phi = 0°$-patterns are seen to coincide comparing the HO-ADM with HO-MoM, effectively verifying the outlined procedure in Section II. There is equally good agreement in other ϕ-cuts.

Table I shows a comparison of solution time and memory consumption between the HO-ADM and ESTEAM. Herein, the total solution time refers to generation of BFs, matrix filling, preconditioner generation and the iterative solution time. Total memory consumption refers to storage of required matrices, the Krylov subspace as well as the preconditioner.

For reference, the HO-MoM solution has been included

TABLE I
COMPARISON OF SOLUTION TIME AND MEMORY CONSUMPTION ON AN INTEL® CORE® I7-9850H CPU @ 2.6 GHZ WITH 6 CORES.

Method	Total Simulation Time	Memory Consumption	Number of Iterations
HO-MoM	1 h 12 min	14 GB	N/A
HO-MLFMM	24 min	1.2 GB	245
Extended HO-ADM	41 s	1.6 GB	181

which takes 1 hour and 12 min to complete, with a memory consumption of 14 GB. By employing the more appropriate HO-MLFMM the solution time is around 24 min with a memory consumption of only 1.2 GB. At the penalty of slightly increased memory consumption (1.6 GB) using the extended HO-ADM, the solution time is reduced to 41 s.

IV. CONCLUSION

We presented an extended Higher-Order Array Decomposition Method capable of analyzing connected antenna arrays and applied it to a 8×8 sub-array designed for the Europa Lander mission. The results show a substantial computational speed-up by a factor of 35 compared to HO-MLFMM. This speed-up is achieved while maintaining a memory consumption comparable to HO-MFLMM. Results for the full 32×32-element array will be presented at the conference.

REFERENCES

[1] O. Borries, P. Meincke, E. Jørgensen, S. B. Sørensen, and P. C. Hansen, "Improved multilevel fast multipole method for higher-order discretizations," *European Conference on Antennas and Propagation*, pp. 3610–3614, 2014.

[2] S. Sharma and P. Triverio, "AIMx: an extended adaptive integral method for the fast electromagnetic modeling of complex structures," *IEEE Transactions on Antennas and Propagation*, vol. 69, no. 12, pp. 8603–8617, 2021.

[3] J. White, J. Phillips, and T. Korsmeyer, "Comparing precorrected-FFT and fast multipole algorithms for solving three-dimensional potential integral equations," in *Proceedings of the Colorado Conference on Iterative Methods*. Citeseer, 1994, pp. 4–10.

[4] E. Lucente, A. Monorchio, and R. Mittra, "An iteration-free MoM approach based on excitation independent characteristic basis functions for solving large multiscale electromagnetic scattering problems," *IEEE Transactions on Antennas and Propagation*, vol. 56, no. 4, pp. 999–1007, 2008.

[5] W. Xiang, W. Yang, and W. Lu, "Fast sub-entire-domain basis functions method for analysis of composite finite periodic structures with dielectric-conductor cells," *IEEE Antennas and Wireless Propagation Letters*, 2022.

[6] R. W. Kindt, K. Sertel, E. Topsakal, and J. L. Volakis, "Array decomposition method for the accurate analysis of finite arrays," *IEEE Transactions on Antennas and Propagation*, vol. 51, no. 6, pp. 1364–1372, 2003.

[7] M. Brandt-Møller, M. Mattes, O. Breinbjerg, M. Zhou, and O. Borries, "Array decomposition method for arbitrary-element regular arrays using higher order basis functions," *IEEE Antennas and Wireless Propagation Letters*, vol. 22, no. 1, pp. 24–28, 2023.

[8] Z. Peng, K.-H. Lim, and J.-F. Lee, "A discontinuous Galerkin surface integral equation method for electromagnetic wave scattering from non-penetrable targets," *IEEE Transactions on Antennas and Propagation*, vol. 61, no. 7, pp. 3617–3628, 2013.

[9] N. Chahat, B. Cook, H. Lim, and P. Estabrook, "All-metal dual-frequency RHCP high-gain antenna for a potential Europa lander," *IEEE Transactions on Antennas and Propagation*, vol. 66, no. 12, pp. 6791–6798, 2018.

[10] TICRA, "TICRA Tools ESTEAM," https://www.ticra.com/software/esteam/, 2019.

Conference Paper III

Extension of the Higher-Order Array Decomposition Method for Arrays with Non-identical Elements

Magnus Brandt-Møller, Michael Mattes, Olav Breinbjerg, Min Zhou, Erik Jørgensen

Status: Published

Bibliography

Extension of the Higher-Order Array Decomposition Method for Arrays with Non-identical Elements

Magnus Brandt-Møller*
Michael Mattes
National Space Institute
Technical University of Denmark
Kongens Lyngby, Denmark
{magbran,mmattes}@dtu.dk

Min Zhou
Erik Jørgensen
TICRA
Copenhagen, Denmark
{mz,ej}@ticra.com

Olav Breinbjerg
ElMaReCo
Copenhagen, Denmark
olavbreinbjerg@outlook.com

***Abstract*—The Higher-Order Array Decomposition Method (HO-ADM) is extended to arrays with non-identical elements. This extension is achieved by appropriate manipulation of the FFT-accelerated matrix-vector product (MVP), special meshing, and by hiding a selected subset of unknowns in the iterative solution process. We demonstrate that the simulation time for a 1024-element patch array can be reduced by an order of magnitude by employing HO-ADM compared to other fast methods such as MLFMM.**

***Index Terms*—antenna-arrays, non-identical elements, multi-level block-Toeplitz, higher-order basis functions**

I. Introduction

Array antennas are a key component in next-generation satellite payloads and user terminals. To meet performance requirements for space applications, future array antennas will be electrically large with densely packed array elements. While such antennas commonly employ identical elements, the use of non-identical elements can provide additional flexibility e.g. in beam shaping, side lobe suppression, and optimization of weight, size, and cost [1], [2].

The conventional full-wave Method of Moments (MoM) takes into account the mutual coupling between the densely packed elements, but suffers from high computational complexity $\mathcal{O}(N^2) - \mathcal{O}(N^3)$ and memory consumption $\mathcal{O}(N^2)$.

Numerous methods, based on error-controllable approximations, have been proposed to enable the efficient full-wave analysis of electrically large arrays, reducing memory consumption and computational complexity to $\mathcal{O}(N \log N)$. These comprise the Multi-Level Fast Multipole Method (MLFMM) [3], the Adaptive Integral Method (AIM) [4], and the pre-corrected fast Fourier transform (pFFT) [5], with the last two necessitating the projection of Basis Functions (BFs) onto a regular grid. For methods based on Macro-Basis Functions (MBFs) [6], [7], the generation and number of MBFs to be included are determined by the specific problem, and the error cannot be controlled beforehand.

By employing the Higher-Order Array Decomposition Method (HO-ADM) [8], it is possible to improve the computational efficiency even further without using approximations. Hitherto, each array element had to be identical in the HO-ADM, effectively excluding the analysis of non-identical-element arrays, and frequency selective surfaces. In this paper, the existing HO-ADM is extended to handle arrays with non-identical elements.

This paper is organized as follows. Section II briefly reviews the HO-ADM and presents the necessary steps to extent the HO-ADM to arrays with non-identical elements. Section III presents a numerical example validating the capabilities of the extended HO-ADM. Lastly, conclusions are given in Section IV.

This work was partly funded by Innovation Fund Denmark with grant number 0153-00057B. *Corresponding author.

II. HO-ADM with Non-identical Elements

The Higher-Order Array Decomposition Method (HO-ADM) is a fast full-wave boundary integral equation method, employing higher-order hierarchical Legendre basis functions on curved quadrilateral mesh-cells applicable to regular arrays with arbitrary volumetric elements. As detailed in [9], the Discontinuous Galerkin Method (DGM) can be employed in the HO-ADM to also handle thinned and connected arrays.

The computational complexity and memory consumption of the HO-ADM scales as $\mathcal{O}(s^2 T \log T)$ and $\mathcal{O}(s^2 T)$, respectively, where s is the number of basis functions for each array element and T is the total number of array elements. Key to the computational efficiency is an FFT-accelerated matrix-vector product (MVP), which relies on the inherent multi-level block-Toeplitz (MBT) MoM matrix arising for regular arrays.

For the MBT property to hold, array elements have to be identical, i.e. they must possess exactly the same number of basis functions and mesh-discretization. Therefore, to allow for non-identical elements in the HO-ADM, two key aspects are needed: special unit-cell meshing and appropriate manipulation of the MVP.

A. Unit-cell Meshing

For illustration, we take outset in a generic non-identical $3 \times 3 = 9$-element array as depicted in Fig. 1 (a). By superimposing the outline of the nine different elements on top of each other (a mathematical union), a new super unit-cell (SUC) with 13 distinct mesh-regions arise as shown in Fig. 1 (c). Utilizing this SUC, a 3×3-identical-element array

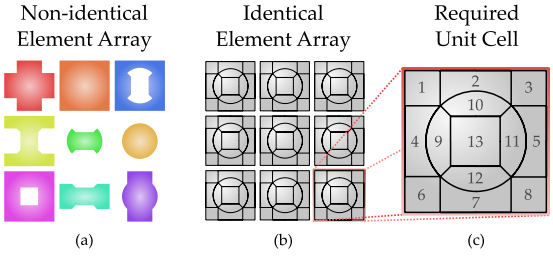

Fig. 1. (a) Illustration of a 3×3 array of generic non-identical elements. (b) an array of identical elements with mesh-regions which can be removed to transform each element to that of the original non-identical element array. (c) The unit-cell for the HO-ADM with the 13 required mesh-regions.

(Fig. 1 (b)) can be constructed on which the HO-ADM can readily be applied.

Assuming for now that we can exclude mesh-regions from the SUC at any position in the array, we can realize any of the nine different elements. For example, the green center element of the non-identical element array can be formed by excluding mesh-regions $\{1, 2, 3, 4, 5, 6, 7, 8, 10, 12\}$ from the SUC, while the blue top-right element can be formed by excluding mesh-regions $\{10, 12, 13\}$. It is noted, that the 13 mesh-regions of the SUC can be combined into numerous more individual elements than the nine distinct elements discussed here. Also, bear in mind that finer meshing inside the 13 mesh-regions is possible and could be necessary depending on their electrical size.

This meshing procedure inevitably requires modeling of unnecessary mesh-cells and therefore also unknowns. However, since the MoM matrix is MBT it contains many redundant blocks. Consequently, only the unique information needs to be calculated and the computational overhead is still small enough for the HO-ADM to have an advantage over other fast methods as demonstrated in Section III.

B. MVP Manipulation

It was assumed above that any desired number of mesh-regions can be excluded from the array elements at any position in the array lattice. In practice, this exclusion is achieved by manipulating the MVP used in the iterative solution process and by hiding unknowns from the perspective of the iterative solver.

More specifically, when performing the FFT-accelerated MVP, the entries pertaining to quadrilaterals in excluded mesh-regions are zeroed in the unknown vector. This ensures that the currents on removed quadrilaterals can not couple to currents on any other quadrilateral in the array. Additionally, entries in the vector resulting from the MVP associated with excluded mesh-regions are zeroed to ensure that currents on all other elements cannot induce any currents on excluded quadrilaterals themselves.

Finally, the excitation vector, too, must be zeroed accordingly for the iterative solver to calculate the residual vectors corresponding to the real situation where the zeroed unknowns did not exist at all, effectively hiding unknowns from the iterative solver. We note that the use of a SUC together with hidden unknowns allows for the analysis of all combinations of the nine distinct array elements in every position, without recalculation of any MoM matrix elements.

In summary, by carefully constructing the mesh of the unit-cell of the array while simultaneously hiding unknowns from the iterative solver, individual mesh-cells can be excluded from the iterative solution process. This allows one to obtain the exact same MoM solution as if those mesh-cells did not exist at all. Consequently, the analysis of non-identical elements has been made possible while retaining an FFT-accelerated MVP.

III. Numerical Verification

We consider an 8×128-element linearly polarized patch antenna array with 1024 independent wire excitations operating at $1.75\,\mathrm{GHz}$, as depicted in Fig. 2. It is composed of 128 linear arrays of size 8×1 comprising non-identical space-tapered elements which effectively achieve an amplitude tapering in the E-plane to reduce the first side-lobe level (FSLL). This 2D-array is based on the 1D-array reported in [10].

The reported results have been generated on a laptop with an Intel® Core® i7-9850H CPU @ $2.6\,\mathrm{GHz}$ with 6 cores. Comparisons are made with the full-wave solver in ESTEAM [11] which is based on a state-of-the-art HO-MLFMM implementation. The generalized minimal residual method (GMRES) iterative solver is employed with relative residual error tolerance of 10^{-3}.

The complete structure is meshed using 55,296 quadrilateral mesh-cells comprising $N = 440{,}736$ unknowns in the HO-MLFMM, while $N = 507{,}904$ unknowns are needed in the HO-ADM. The additional unknowns are required due to the special meshing of the unit-cell as described in Section II as well as the use of DGM-unknowns as detailed in [9]. Nevertheless, as evident from Table I, the total computation time can be reduced from $29\,\mathrm{min}$ using HO-MLFMM to $3\,\mathrm{min}$ using the HO-ADM (a factor of 10), even though HO-ADM requires circa $15\,\%$ more unknowns than HO-MLFMM.

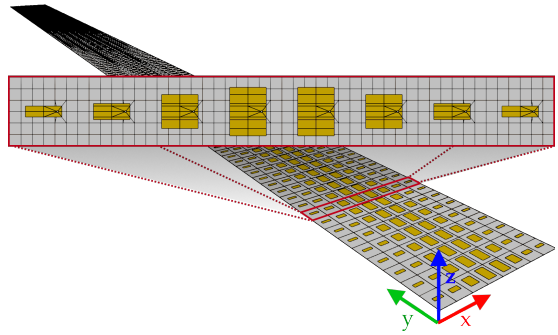

Fig. 2. 8×128-element linearly-polarized patch antenna, including illustration of employed meshing for the reported results of a single space-tapered row. The illustrated coordinate system is employed for the far-field evaluation in which ($\theta = 0°, \phi = 0°$) corresponds to the positive x-axis.

TABLE I
TOTAL SOLUTION TIME AND MEMORY CONSUMPTION FOR THE 8×128 ARRAY IN FIG. 2, COMPARING HO-MLFMM AND HO-ADM ON AN INTEL® CORE® I7-9850H CPU @ 2.6 GHZ WITH 6 CORES.

Method	Total Simulation Time	Memory Consumption	Number of Iterations	Time per Iteration
HO-MoM	N/A	1443 GB	N/A	N/A
HO-MLFMM	29 min	7.2 GB	223	4.9 s
HO-ADM	3 min 2 s	7.9 GB	441	0.3 s

The speedup is even greater for the MVP alone which is reduced from $4.9\,\mathrm{s}$ to $0.3\,\mathrm{s}$ per iteration (a factor of 16). Here it should be noted that the FFT-accelerated MVP in the HO-ADM is exact, while the MLFMM-accelerated MVP is approximate, though error-controllable.

Fig. 3 shows the radiated co- and cx-pol far-field patterns ($\phi{=}\,0°$- and $\phi{=}\,90°$-cuts) comparing HO-ADM and HO-MLFMM. The calculated peak directivity for the array is $37.9\,\mathrm{dB}$ and the FSLL is $-18.5\,\mathrm{dB}$ for both methods. The patterns for the HO-ADM and HO-MLFMM are seen to agree excellently in both the E- and H-plane. The co-pol relative RMS-difference $\varepsilon_{\mathrm{RMS}}$ between the HO-ADM and HO-MLFMM is $0.4\,\%$ and $0.3\,\%$ in the E- and H-plane, respectively. The cx-pol is below the numerical precision in the E-plane and the H-plane cx-pol relative RMS-difference $\varepsilon_{\mathrm{RMS}}$ is $0.5\,\%$ for the complete 360 deg. region.

IV. CONCLUSION

In this paper, we proposed and validated an extension to the Higher-Order Array Decomposition Method for the analysis of antenna arrays with non-identical elements and applied it to a $8 \times 128 = 1024$-element patch array. The results show that by using the HO-ADM, an order of magnitude computational speed-up is achievable compared to HO-MLFMM, while maintaining a memory consumption comparable to HO-MFLMM. In addition, the results demonstrate excellent agreement between the HO-ADM and MLFMM ($< 0.4\,\%$ relative RMS difference).

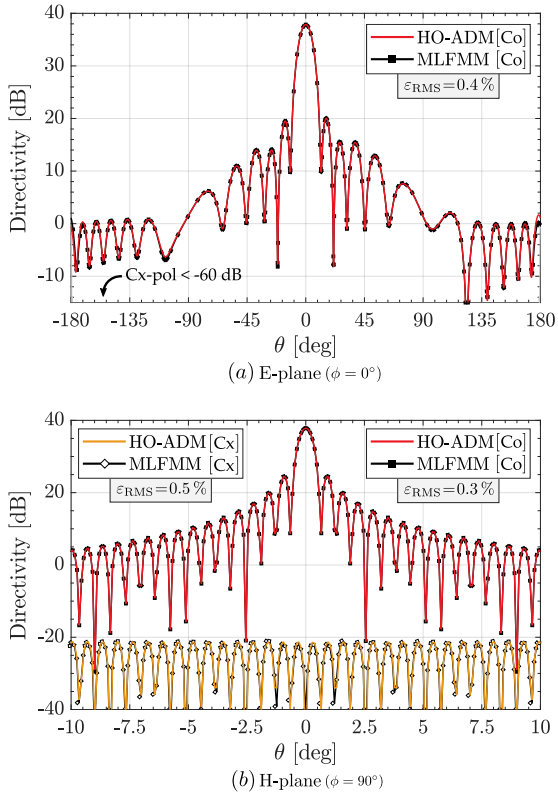

Fig. 3. Far-field co- and cx-pol directivity patterns at 1.75 GHz comparing the HO-ADM to the HO-MLFMM for the 8×128-element patch antenna array of Fig. 2. (a) E-plane patterns ($\phi = 0°$) (b) H-plane patterns ($\phi = 90°$). – Due to the very narrow lobe width in the H-plane only the central 20 deg. region is shown here. The cross-pol field level in the E-plane is below $60\,\mathrm{dB}$.

REFERENCES

[1] S. Maddio, G. Pelosi, M. Righini, and S. Selleri, "16-element circular polarised antenna array based on sequential arrangement of non-identical disc patches," *Electronics Letters*, vol. 54, no. 3, pp. 113–114, 2018.

[2] H. A. Diawuo and Y.-B. Jung, "Broadband proximity-coupled microstrip planar antenna array for 5g cellular applications," *IEEE Antennas and Wireless Propagation Letters*, vol. 17, no. 7, pp. 1286–1290, 2018.

[3] O. Borries, P. Meincke, E. Jørgensen, S. B. Sørensen, and P. C. Hansen, "Improved multilevel fast multipole method for higher-order discretizations," *European Conference on Antennas and Propagation*, pp. 3610–3614, 2014.

[4] S. Sharma and P. Triverio, "AIMx: an extended adaptive integral method for the fast electromagnetic modeling of complex structures," *IEEE Transactions on Antennas and Propagation*, vol. 69, no. 12, pp. 8603–8617, 2021.

[5] J. White, J. Phillips, and T. Korsmeyer, "Comparing precorrected-FFT and fast multipole algorithms for solving three-dimensional potential integral equations," in *Proceedings of the Colorado Conference on Iterative Methods*. Citeseer, 1994, pp. 4–10.

[6] E. Lucente, A. Monorchio, and R. Mittra, "An iteration-free MoM approach based on excitation independent characteristic basis functions for solving large multiscale electromagnetic scattering problems," *IEEE Transactions on Antennas and Propagation*, vol. 56, no. 4, pp. 999–1007, 2008.

[7] W. Xiang, W. Yang, and W. Lu, "Fast sub-entire-domain basis functions method for analysis of composite finite periodic structures with dielectric-conductor cells," *IEEE Antennas and Wireless Propagation Letters*, 2022.

[8] M. Brandt-Møller, M. Mattes, O. Breinbjerg, M. Zhou, and O. Borries, "Array decomposition method for arbitrary-element regular arrays using higher order basis functions," *IEEE Antennas and Wireless Propagation Letters*, vol. 22, no. 1, pp. 24–28, 2023.

[9] M. Brandt-Møller, M. Mattes, O. Breinbjerg, M. Zhou, and E. Jørgensen, "Extended higher-order array decomposition method for fully populated or thinned array antennas and scatterers with connected elements," *IEEE Transactions on Antennas and Propagation*, submitted, 2023.

[10] B. Singh, N. Sarwade, and K. Ray, "Non-identical rectangular microstrip antenna arrays for amplitude tapering," *IETE Journal of research*, vol. 64, no. 3, pp. 387–393, 2018.

[11] TICRA, "TICRA Tools ESTEAM," https://www.ticra.com/software/esteam/, 2019.

Appendices

APPENDIX A

Mathematical Foundation of HO-ADM

This chapter contains mathematical details pertaining to the implemented Higher-Order Array Decomposition method.

A.1 Surface Discretization and Higher-Order Basis Functions

Curved quadrilaterals (also called quads or mesh cells) with parametrization $\vec{r}(u,v)$ are used to discretize the geometry [87], using the HO-hierarchical Legendre basis functions from [88] to expand the surface current density as

$$\vec{J}(u,v) = \frac{\vec{e}_u}{\mathcal{J}_S(u,v)} \sum_{m=0}^{M^u} \sum_{n=0}^{N^v} C_{mn}^{uv} \tilde{P}_m(u) P_n(v) x_{mn}^u + \frac{\vec{e}_v}{\mathcal{J}_S(u,v)} \sum_{m=0}^{M^v} \sum_{n=0}^{N^u} C_{mn}^{uv} \tilde{P}_m(v) P_n(u) x_{mn}^v, \tag{A.1}$$

in which $\{u,v\}$ are curvilinear coordinates of a given quad, $x_{mn}^{\{u,v\}}$ are the unknown current coefficients in the $\{u,v\}$-direction, $\vec{e}_{\{u,v\}} = \frac{\partial \vec{r}}{\partial \{u,v\}}$ are unitary vectors, $\mathcal{J}_S$ is the Jacobian, P_n are Legendre polynomials of order n and C_{mn}^{uv} are constants chosen to minimize the MoM matrix condition number. $\tilde{P}_m$ are the modified Legendre

polynomials defined as

$$\tilde{P}_m(u) = \begin{cases} 1-u, & m=0 \\ 1+u, & m=1 \\ P_m(u) - P_{m-2}(u), & m \geq 2 \end{cases} \begin{matrix} \left.\vphantom{\begin{matrix}1\\1\end{matrix}}\right\} \textbf{Doublets} \\ \textbf{Singletons} \end{matrix} . \tag{A.2}$$

The modified Legendre polynomials are only used in the direction of the current, whereas ordinary Legendre polynomials are used in the transverse direction. The term doublets refer to the usual roof-top current continuity-enforcing basis functions having support over two quads. The term singletons refer to local current density variations and have support only within a single quad and are zero on the edges of the quad. The maximum polynomial order $N^{\{u,v\}} = M^{\{u,v\}} - 1$ for the current expansion in the $\{u, v\}$-direction is chosen independently for each quad based on its electrical size.

A.2 Accelerated Matrix-Vector Product

The efficiency of the Array Decomposition Method and other FFT-accelerated methods stems from a fundamental yet indispensable property of circulant matrices; The matrix-vector product between a circulant matrix $\mathbf{M} \in \mathcal{C}^{N\times N}$ and a given vector $\vec{x} \in \mathcal{C}^{N\times 1}$ can be expressed as as a discrete circular convolution:

$$\begin{aligned} \mathbf{M}\vec{x} &= \begin{bmatrix} c_0 & c_{N-1} & \dots & c_2 & c_1 \\ c_1 & c_0 & c_{N-1} & & c_2 \\ \vdots & c_1 & c_0 & \ddots & \vdots \\ c_{N-2} & & \ddots & \ddots & c_{N-1} \\ c_{N-1} & c_{N-2} & \dots & c_1 & c_0 \end{bmatrix} \begin{bmatrix} x_0 \\ x_1 \\ x_2 \\ \vdots \\ x_N \end{bmatrix} = \begin{bmatrix} \sum_{i=0}^{N-1} x_i c_{(N-i+0) \bmod N} \\ \sum_{i=0}^{N-1} x_i c_{(N-i+1) \bmod N} \\ \vdots \\ \sum_{i=0}^{N-1} x_i c_{(2N-1-i) \bmod N} \end{bmatrix} \\ &= \underbrace{\begin{bmatrix} c_0 \\ c_1 \\ \vdots \\ c_{N-2} \\ c_{N-1} \end{bmatrix}}_{\vec{m}} \circledast \begin{bmatrix} x_0 \\ x_1 \\ x_2 \\ \vdots \\ x_N \end{bmatrix} \end{aligned} \tag{A.3}$$

where $\vec{m}$ is the first column of the circulant matrix $\mathbf{M}$, and $\circledast$ denotes the discrete circular convolution. This, together with the circular convolution theorem [135], allows one to retrieve the direct solution to a linear system of equations with a circulant system matrix in $\mathcal{O}(N \log N)$ time:

$$\mathbf{M}\vec{x} = \vec{m} \circledast \vec{x} = \mathcal{F}^{-1}\{\mathcal{F}\{\vec{m}\} \odot \mathcal{F}\{\vec{x}\}\} = \vec{b} \leftrightarrow \vec{x} = \mathcal{F}^{-1}\{\mathcal{F}\{\vec{b}\} \oslash \mathcal{F}\{\vec{m}\}\}, \tag{A.4}$$

where $\mathcal{F}$ denotes the discrete Fourier transform, $\odot$ is the Hadamard (element-wise) product, and $\oslash$ is the Hadamard division operator as defined in [136]. This generalizes trivially to multi-level block circulant matrices, for which the matrix-vector product (MVP) can be found as

$$\mathbf{M}\vec{x} = \mathcal{F}_d^{-1}\{\mathcal{F}_d\{\mathbf{C}\} \odot \mathcal{F}_d\{\mathbf{X}\}\}, \tag{A.5}$$

and the direct solution can be found as

$$\vec{x} = \mathcal{F}_d^{-1}\{\mathcal{F}_d\{\mathbf{B}\} \oslash \mathcal{F}_d\{\mathbf{C}\}\}, \tag{A.6}$$

in which $\mathbf{B}$, $\mathbf{X}$ and $\mathbf{C}$ are d-dimensional tensors containing the rearranged (according to the d multi-levels) right-hand side entries, unknowns, and the unique entries of the system matrix, respectively.

Unfortunately, the direct solution approach as outlines in (A.6) is not applicable for a general full-wave computational electromagnetics solver. This is mainly due to the vector nature of the Helmholtz wave equation, which in the context of integral equations does not allow for a multi-level Toeplitz (or circulant) MoM matrix structure where the inner-most matrix is also Toeplitz*. Nevertheless, as we shall see in the following, an FFT-accelerated MVP is still possible, albeit with a quadratic scaling in the number of unknowns, s, associated with the inner-most matrix.

We take outset in the hypothetical case of a 2×2 array with one BF per array element (i.e. $s = 1$) which gives rise to a MoM matrix with $d = 2$ multi-levels and without any arbitrary matrix at the inner-most level. In this case, the MoM matrix $\mathbf{A}$ assumes a block-Toeplitz with Toeplitz-blocks (BTTB) structure, and the resulting MVP is given as

$$\mathbf{A}\vec{x} = \left[\begin{array}{cc:cc} a_1 & a_3 & a_7 & a_9 \\ a_2 & a_1 & a_8 & a_7 \\ \hdashline a_4 & a_6 & a_1 & a_3 \\ a_5 & a_4 & a_2 & a_1 \end{array}\right] \left[\begin{array}{c} x_1 \\ x_2 \\ x_3 \\ x_4 \end{array}\right], \tag{A.7}$$

where we have $d = 2$ Toeplitz levels and where the generally complex-valued entries $a_1, \ldots, a_9$ are the unique values of the matrix. The idea is now to extend the Toeplitz blocks at each level to end up with a block-circulant with circulant blocks (BCCB) matrix. To do so, the blocks at the first level is extended from Toeplitz to circulant blocks [84, sec. 4.7.7] giving rise to the following one-level extended MoM matrix $\mathbf{A}^{\mathcal{C},1}$:

*We note that any matrix can in principle be made circulant, and thus the associated MVP can be accelerated via the FFT. However, for an arbitrary matrix that would require more operations than just doing the ordinary MVP itself.

$$\mathbf{A}^{\mathcal{C},1}\vec{x}^{\,\mathcal{C},1} = \left[\begin{array}{cc|cc|cc} \underline{a}_1 & \underline{a}_3 & \underline{a}_7 & \underline{a}_9 & a_4 & a_6 \\ \underline{a}_2 & \underline{a}_1 & \underline{a}_8 & \underline{a}_7 & a_5 & a_4 \\ \underline{a}_4 & \underline{a}_6 & \underline{a}_1 & \underline{a}_3 & a_7 & a_9 \\ \underline{a}_5 & \underline{a}_4 & \underline{a}_2 & \underline{a}_1 & a_7 & a_9 \\ a_7 & a_9 & a_4 & a_6 & a_1 & a_3 \\ a_8 & a_7 & a_5 & a_4 & a_2 & a_1 \end{array}\right] \left[\begin{array}{c} x_1 \\ x_2 \\ x_3 \\ x_4 \\ 0 \\ 0 \end{array}\right], \tag{A.8}$$

where zeros have been placed at appropriate positions in the extended unknown vector $\vec{x}^{\,\mathcal{C},1}$, in order to calculate correctly the original MVP. Note that underlines indicates the positions of the orignal entries of the MoM matrix $\mathbf{A}$. Note also, that the resulting MVP $\mathbf{A}^{\mathcal{C},1}\vec{x}^{\,\mathcal{C},1}$ has two additional rows which are eventually discarded.

Next, the blocks at the second level is extended from Toeplitz to circulant blocks giving rise to the two-level circularly extended MoM matrix $\mathbf{A}^{\mathcal{C},2}$

$$\mathbf{A}^{\mathcal{C},2}\vec{x}^{\,\mathcal{C},2} = \left[\begin{array}{ccc|ccc|ccc} \underline{a}_1 & \underline{a}_3 & a_2 & \underline{a}_7 & \underline{a}_9 & a_8 & a_4 & a_6 & a_5 \\ \underline{a}_2 & \underline{a}_1 & a_3 & \underline{a}_8 & \underline{a}_7 & a_9 & a_5 & a_4 & a_6 \\ \underline{a}_3 & \underline{a}_2 & \underline{a}_1 & \underline{a}_9 & \underline{a}_8 & \underline{a}_7 & \underline{a}_6 & \underline{a}_5 & \underline{a}_4 \\ \underline{a}_4 & \underline{a}_6 & a_5 & \underline{a}_1 & \underline{a}_3 & a_2 & a_7 & a_9 & a_8 \\ \underline{a}_5 & \underline{a}_4 & a_6 & \underline{a}_2 & \underline{a}_1 & a_3 & a_8 & a_7 & a_9 \\ \underline{a}_6 & \underline{a}_5 & \underline{a}_4 & \underline{a}_3 & \underline{a}_2 & \underline{a}_1 & \underline{a}_9 & \underline{a}_8 & \underline{a}_7 \\ a_7 & a_9 & a_8 & a_4 & a_6 & a_5 & a_1 & a_3 & a_2 \\ a_8 & a_7 & a_9 & a_5 & a_4 & a_6 & a_2 & a_1 & a_3 \\ a_9 & a_8 & a_7 & a_6 & a_5 & a_4 & a_3 & a_2 & a_1 \end{array}\right] \left[\begin{array}{c} x_1 \\ x_2 \\ 0 \\ x_3 \\ x_4 \\ 0 \\ 0 \\ 0 \\ 0 \end{array}\right]. \tag{A.9}$$

where zeros have again been placed at appropriate positions in the extended unknown vector $\vec{x}^{\,\mathcal{C},2}$, in order to calculate correctly the original MVP.

For the present case with a two-dimensional array lattice $d = 2$ we can stop extending the matrix at this point. For arrays in higher dimensions $d > 2$ one would keep on extending the MoM matrix using the outlined procedure, until reaching $\mathbf{A}^{\mathcal{C},d}$. We note, that in practice $\mathbf{A}^{\mathcal{C},d}$ is never formed explicitly, which will be evident in the following.

The entries in the MVP, $\mathbf{V}$, of the circulant-extended MoM matrix $\mathbf{A}^{\mathcal{C},2}$ with a given extended vector of unknowns $\vec{x}^{\,\mathcal{C},2}$ can now, using the result of (A.3), be expressed as a $(d = 2)$-dimensional circular convolution

$$\mathbf{V} = \underbrace{\begin{bmatrix} a_1 & a_4 & a_7 \\ a_2 & a_5 & a_8 \\ a_3 & a_6 & a_9 \end{bmatrix}}_{\mathbf{C}} \circledast \underbrace{\begin{bmatrix} x_1 & x_3 & 0 \\ x_2 & x_4 & 0 \\ 0 & 0 & 0 \end{bmatrix}}_{\mathbf{X}}, \tag{A.10}$$

where $\mathbf{C}$ is a matrix containing only the unique entries of the original MoM matrix $\mathbf{A}$. Because these entries can be used to generate the circularly extended MoM matrix $\mathbf{A}^{\mathcal{C},2}$, $\mathbf{C}$ is denoted as the circulant generator.

Note how the extended unknown vector $\vec{x}^{\mathcal{C},2}$ has been arranged in a matrix $\mathbf{X}$ of the same size and dimensions as $\mathbf{C}$ in which the only non-zero elements are the original unknowns.

By utilizing the result of (A.5), the $(d = 2)$-dimensional discrete circular convolution can be expressed in terms of the discrete Fourier transformation as

$$\mathbf{V} = \mathcal{F}_2^{-1}\left\{\mathcal{F}_2\left\{\begin{bmatrix} a_1 & a_4 & a_7 \\ a_2 & a_5 & a_8 \\ a_3 & a_6 & a_9 \end{bmatrix}\right\} \odot \mathcal{F}_2\left\{\begin{bmatrix} x_1 & x_3 & 0 \\ x_2 & x_4 & 0 \\ 0 & 0 & 0 \end{bmatrix}\right\}\right\}, \tag{A.11}$$

where $\mathcal{F}_2$ denotes the 2-dimensional discrete Fourier transform and $\odot$ denotes the Hadamard operator, i.e. element-wise multiplication[†]. Hereafter, the entries $\mathbf{U}$ of the matrix-vector product $\vec{u} = \mathbf{A}\vec{x}$, are readily available by accessing the sub-matrix $\mathbf{U} = \mathbf{V}_{1\dots n_1, 1\dots n_2} \in \mathbb{C}^{n_1 \times n_2}$,, where $n_1 = 2$ and $n_2 = 2$ are the number of array elements in each lattice dimension. The desired column vector $\vec{u}$ is obtained by interpreting the contiguous memory column-major matrix $\mathbf{U}$ as a one-dimensional vector.

In the more general case where we have more than $s = 1$ BF per array element, the unique entries a_k of $\mathbf{A}^{\mathcal{C}}$ for $k = 1, \dots, 9$ themselves become matrices $\mathbf{a}_k \in \mathbb{C}^{s\times s}$ with entries denoted by $a_k^{m,n}$, while the vector entries x_k become column vectors $\vec{x}_k \in \mathbb{C}^{s\times 1}$ with entries enumerated as x_k^n. Since the inner-most $\mathbf{a}_k$ blocks do not, in general, possess any special symmetry they cannot be accelerated by the FFT. Consequently, in order to obtain the full MVP entries $\mathbf{V}$, several matrix-vector products $\mathbf{V}_m$ need to be computed for each row $m = 1, \dots, s$ by summation of Hadamard products over each column $n = 1, \dots, s$ of $\mathbf{a}_k$ as follows

$$\mathbf{V}_m = \mathcal{F}_2^{-1}\left\{\sum_{n=1}^{s} \mathcal{F}_2 \underbrace{\left\{\begin{bmatrix} a_1^{m,n} & a_4^{m,n} & a_7^{m,n} \\ a_2^{m,n} & a_5^{m,n} & a_8^{m,n} \\ a_3^{m,n} & a_6^{m,n} & a_9^{m,n} \end{bmatrix}\right\}}_{\mathbf{C}^{m,n}} \odot \mathcal{F}_2 \underbrace{\left\{\begin{bmatrix} x_1^n & x_4^n & 0 \\ x_2^n & x_5^n & 0 \\ 0 & 0 & 0 \end{bmatrix}\right\}}_{\mathbf{X}^n}\right\}. \tag{A.12}$$

The desired MVP $\vec{u} = \mathbf{A}\vec{x}$ is obtained by copying the sub-matrices $\mathbf{U}_m = \mathbf{V}_m(1{:}n_1, 1{:}n_2)$ interpreted as column-vectors, into $\vec{u}$ in the order of m. Note that in practice the Fourier transformations $\mathcal{F}_2$ of $\mathbf{C}^{m,n}$ for all m and n is performed only once before entering the iterative solution process, while the Fourier transformation $\mathcal{F}_2$ of $\mathbf{X}_n$ and the inverse Fourier transformation $\mathcal{F}_2^{-1}$ for $\mathbf{V}_m$, over all n and m, respectively, is performed only once per MVP.

[†]We note that the MVP need not be formulated with Hadamard products. In fact, implementation wise, it is more efficient to implicitly diagonalize $\mathbf{C}$ and multiply it with the extended unknown vector $\vec{x}^{\mathcal{C},d}$ directly, for which very efficient LAPACK routines exist.

A.3 The Discontinuous Galerkin Formulation for Surface Integral Equations

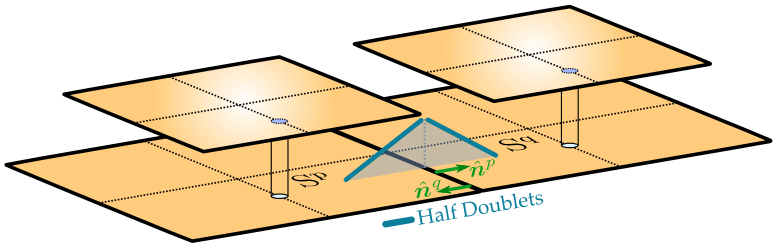

Figure A.1: Two patch antennas on which half-doublet BFs are introduced on either side of the connected boundaries between adjacent elements. Only one full-roof top is shown for illustrative purposes. The Discontinuous Galerkin Method is used to enforce current continuity even after splitting the full-roof top BF into two half roof-tops.

Suppose that we are interested in the interaction between two quads p and q which happen to reside on two different array elements as depicted in Figure A.1. The MoM matrix $\mathbf{A}$ with entries $A_{m,n}$ associated with the m^{th} test function $\vec{f}_t^{\,m}$, n^{th} basis function $\vec{f}_b^{\,n}$, and the integral operator $\mathcal{L}$, can be formulated with five inner products $\mathcal{I}_i,\ i \in \{1,\ldots,5\}$ as

$$\begin{aligned} A_{m,n} &= \langle \vec{f}_t^{\,m}, \mathcal{L}[\vec{f}_b^{\,n}; \mathcal{S}^q] \rangle_{\mathcal{S}^p} \\ &= -\overbrace{\langle \vec{f}_t^{\,m}, \mathcal{M}[\vec{f}_b^{\,n}; \mathcal{S}^q] \rangle_{\mathcal{S}^p}}^{\mathcal{I}_1} + k^{-2} \Bigg[\overbrace{\langle \nabla \cdot \vec{f}_t^{\,m}, \mathcal{M}[\nabla' \cdot \vec{f}_b^{\,n}; \mathcal{S}^q] \rangle_{\mathcal{S}^p}}^{\mathcal{I}_2} \\ &\quad - \underbrace{\langle \nabla \cdot \vec{f}_t^{\,m}, \mathcal{N}[\hat{\boldsymbol{n}}^q \cdot \vec{f}_b^{\,n}; \mathcal{C}^q] \rangle_{\mathcal{S}^p}}_{\mathcal{I}_3} - \underbrace{\langle \hat{\boldsymbol{n}}^p \cdot \vec{f}_t^{\,m}, \mathcal{M}[\nabla' \cdot \vec{f}_b^{\,n}; \mathcal{S}^q] \rangle_{\mathcal{C}^p}}_{\mathcal{I}_4} \\ &\quad + \underbrace{\langle \hat{\boldsymbol{n}}^p \cdot \vec{f}_t^{\,m}, \mathcal{N}[\hat{\boldsymbol{n}}^q \cdot \vec{f}_b^{\,n}; \mathcal{C}^q] \rangle_{\mathcal{C}^p}}_{\mathcal{I}_5} \Bigg], \end{aligned} \tag{A.13}$$

after having applied the product rule for divergence, integration by parts and the symmetry of the Green function to remove the non-integrable singularity. $\mathcal{S}^p$ and $\mathcal{S}^q$ are the surfaces of the test and source quads, respectively. $\mathcal{C}^p$ and $\mathcal{C}^q$ are the closed contours around $\mathcal{S}^p$ and $\mathcal{S}^q$, with in-plane outward normal unit vectors denoted as $\hat{\boldsymbol{n}}^p$ and $\hat{\boldsymbol{n}}^q$, respectively. The EFIE operator $\mathcal{L}$, the vector and scalar single-layer

potentials $\mathcal{P}$ and $\mathcal{Q}$, respectively, are defined as

$$\mathcal{L}[\vec{f};\mathcal{S}] = -j\omega\mu \int_{\mathcal{S}} \left[1 + \frac{1}{k^2}\nabla\nabla\cdot\right] \vec{f}(\vec{r}\,')G(\vec{r},\vec{r}\,')d\mathcal{S}' \tag{A.14}$$

$$\mathcal{P}[\vec{f};\mathcal{S}] = j\omega\mu \int_{\mathcal{S}} \vec{f}(\vec{r}\,')G(\vec{r},\vec{r}\,')d\mathcal{S}' \tag{A.15}$$

$$\mathcal{Q}[\psi;\mathcal{C}] = j\omega\mu \oint_{\mathcal{C}} \psi(\vec{r}\,')G(\vec{r},\vec{r}\,')dl', \tag{A.16}$$

in which $G(\vec{r},\vec{r}\,') = \frac{e^{-jk|\vec{r}-\vec{r}\,'|}}{|\vec{r}-\vec{r}\,'|}$ is the three dimensional free-space Green function with wave number $k = \omega\sqrt{\mu_0\varepsilon_0}$, in which μ_0 and ε_0 are the free space magnetic permeability and electric permittivity, respectively. $\vec{r}\,'$ and $\vec{r}$ are position vectors of the source and test quad, respectively.

In case of divergence-conforming BFs and conformal mesh cells, the three inner products $\mathcal{I}_n,\ n \in \{3,4,5\}$ vanish, and we are left with the usual EFIE terms $\mathcal{I}_n,\ n \in \{1,2\}$. In DGM, this is not the case as we tear/cut the doublets (full roof-tops) into half-doublets thereupon necessitating the additional contour integral terms in (A.13). Although current continuity is no longer directly part of the DGM basis function formulation, it is instead weakly enforced via the addition of an extra surface integral penalty term. This residual term is found as outlined in [105] by multiplying the left-hand side of the continuity equation $\hat{\boldsymbol{n}}^p \cdot \vec{f}^{\,m} + \hat{\boldsymbol{n}}^q \cdot \vec{f}^{\,n} = 0$ with the Green function and testing it at the common edge $\mathcal{C}_{pq} = \mathcal{C}_p \cap \mathcal{C}_q$ between two quads p and q, i.e.

$$\mathcal{I}_6 = 2\langle \hat{\boldsymbol{n}}^p \cdot \vec{f}_t^{\,m}, \mathcal{N}[\hat{\boldsymbol{n}}^q \cdot \vec{f}_b^{\,n};\mathcal{C}^q]\rangle_{\mathcal{C}^p}. \tag{A.17}$$

Remarkably, by multiplying $\mathcal{I}_6$ with $-\frac{1}{2k^2}$ and adding it to (A.13), not only is current continuity enforced but the difficult double contour integral $\mathcal{I}_5$ is canceled, albeit with the cost of increased condition number of $\mathbf{A}$ [103]. Therefore, to stabilize the resulting DGM MoM matrix and to provide practical iterative convergence, an extra boundary interior penalty stabilization function $\mathcal{I}_{\mathrm{IP}}(\beta)$ is typically added

$$\mathcal{I}_{\mathrm{IP}}(\beta) = \frac{\beta}{k^2} \oint_{\mathcal{C}_{pq}} [\hat{\boldsymbol{n}}^m \cdot \vec{f}_t^{\,m}(\vec{r})][\hat{\boldsymbol{n}}^n \cdot \vec{f}_b^{\,n}(\vec{r})]dl, \tag{A.18}$$

in which $\beta = \frac{1}{10h}$ is a scalar depending on the average electrical mesh size h. Note that $\mathcal{I}_{\mathrm{IP}}$ is merely responsible for stabilization as the current continuity is already enforced by canceling $\mathcal{I}_5$ via $\mathcal{I}_6$.

This page is intentionally not used for content

APPENDIX B

Computational & Memory Complexity of HO-ADM

The Method of Moments matrix has a multi-level block Toeplitz (MBT) structure in case of two or higher dimensional regular arrays (provided that basis functions are generated sequentially, i.e. in order of the array elements). It should be noted that the number of levels in the block Toeplitz structure corresponds to the number of array lattice dimensions d. The remainder of this appendix will establish formulas for the computational complexity and memory-scaling of HO-ADM. For a detailed discussion on how HO-ADM is implemented, the reader is referred to publications [J1][J2]. For an introduction on FFT accelerated matrix-vector products of MBT matrices, the reader is referred to Appendix A.

In the HO-ADM algorithm, the Toeplitz blocks at each level are extended to circulant matrix blocks (see Appendix A), effectively introducing additional unknowns, resulting in a total number of extended unknowns N_{ext}:

$$N_{ext} = s\prod_{i=1}^{d}[2n_i - 1] \approx 2^d N = s2^d T. \tag{B.1}$$

where s is the total number of basis functions (unknowns) on each array element, d is the total number of array lattice dimensions and n_i is the number of array elements in each dimension i. $T = n_1 n_2 \dots n_d$ is the total number of array elements.

B.1 Computational Complexity - Setup Phase

The algorithm starts in the setup phase. Herein only the unique interactions are calculated, and are extended to circulant blocks, and finally multi-dimensional discrete FFTs are taken along the d array dimensions.

The calculation of the $\prod_{i=1}^{d}[2n_i - 1]$ unique interaction-matrices, each with s^2 entries, gives a computational complexity F_1^{set} of:

$$F_1^{set} = C^{set} s^2 \prod_{i=1}^{d}[2n_i - 1] \approx C^{set} s^2 2^d T \rightarrow O(s^2 T) \tag{B.2}$$

where C^{set} is a constant indicating the average time needed to calculate the interactions between two basis functions on two different array elements. Keep in mind the approximation already employed in Eq. B.1, which means that Eq. B.2 generally overestimates the memory consumption of ADM.

Next, the FFTs of the circulant extended blocks have the computational complexity denoted as F_2^{set}. N_{FFT1} number of FFTs of length L_{FFT1} are applied along the first array lattice dimension, while N_{FFT2} number of FFTs of length L_{FFT2} are applied in the second array lattice dimension:

$$\begin{aligned}
&N_{FFT1} \rightarrow \text{Total number of FFTs in first dimension} = s^2(2n_2 - 1)\\
&N_{FFT2} \rightarrow \text{Total number of FFTs in second dimension} = s^2(2n_1 - 1)\\
&L_{FFT1} \rightarrow \text{Length of FFTs in first dimension} = 2n_1 - 1\\
&L_{FFT2} \rightarrow \text{Length of FFTs in second dimension} = 2n_2 - 1
\end{aligned}$$

Mathematically, the computational cost F_2^{set} can now be found as follows:

$$\begin{aligned}
F_2^{set} &= N_{FFT1} L_{FFT1} \log(L_{FFT1}) + N_{FFT2} L_{FFT2} \log(L_{FFT2})\\
&= s^2(2n_2 - 1)(2n_1 - 1)\log(2n_1 - 1) + s^2(2n_1 - 1)(2n_2 - 1)\log(2n_2 - 1)\\
&= s^2(2n_2 - 1)(2n_1 - 1)[\log(2n_1 - 1)] + \log(2n_2 - 1)]\\
&= s^2(2n_2 - 1)(2n_1 - 1)\log((2n_1 - 1)(2n_2 - 1)) \leftarrow \textbf{2D-FFT}\\
&= sN_{ext}\log\left(\frac{N_{ext}}{s}\right), \text{ for } d = 2
\end{aligned} \tag{B.3}$$

We notice in passing that because we are dealing with a two-dimensional array lattice, a **2D-FFT** scaling appears scaled with s^2. Although only derived in two dimensions, the expression in (B.3) generalizes trivially to higher dimensional arrays $d > 2$.
Using that $N_{ext} \approx s2^d T$ we get:

$$F_2^{set} \approx s2^d \underbrace{sT}_{N} \log\left(2^d \underbrace{T}_{\frac{N}{s}}\right) \rightarrow O(s^2 T \log(T)) \tag{B.4}$$

which shows that the complexity grows quadratically with the number of basis functions s on each array element, and that it grows like the FFT for increasing total

number of array elements T. In passing, we note that it scales exponentially with the number of array dimensions (2^d).
Another perspective is to look at it from the total number of unknowns N:

$$F_2^{set} \approx s2^d N \log\left(2^d \frac{N}{s}\right) \rightarrow O\left(sN \log\left(\frac{N}{s}\right)\right) \tag{B.5}$$

Because the total number of unknowns N is a function of s, this perspective renders it very difficult to understand why the algorithm has a quadratic scaling, which is why the separation $N = sT$ is adopted in this dissertation.
With a constant number of basis functions per array element (s is considered constant), however, this scaling perspective readily reveals a more understandable asymptotic scaling:

$$O\left(sN \log\left(\frac{N}{s}\right)\right) \underbrace{\rightarrow}_{s=\text{const.}} O(N \log(N)) \tag{B.6}$$

The total computational complexity of the setup phase can be summarized as:

$$\begin{aligned} F^{set} &= F_1^{set} + F_2^{set} = C^{set} s^2 2^d T + s^2 2^d T \log\left(2^d T\right) \\ &\rightarrow O\left[s^2\left(C^{set} T + T \log(T)\right)\right] \end{aligned} \tag{B.7}$$

The term $C^{set}T$ has here been included in the asymptotic scaling since it depends on the number of basis functions s on each array element. This result is fast compared to the complexity of ordinary MoM which scales quadratically in both s and total number of array elements (i.e. $O(C^{set}s^2T^2)$). To be more precise, whether HO-ADM is faster than ordinary MoM, depends not only on the asymptotic scaling of HO-ADM, but also on the constant C^{set} and the number of iterations needed in the iterative solver.

B.2 Computational Complexity - Matrix-Vector Product

After the setup phase in which a block-circulant matrix has been implicitly generated, the HO-ADM algorithm provides a fast matrix vector product (MVP) for an iterative solver.
For each iteration this MVP is calculated in three steps:

- F_1^{MVP} Calculate FFT of current iteration unknown vector
- F_2^{MVP} Calculate Hadamard product between circulant generator and the FFT of current unknown vector
- F_3^{MVP} Calculate IFFT of Hadamard product

The required number and lengths of FFTs of the unknown vector is summarized below for $d = 2$:

$$
\begin{aligned}
N_{FFT1} &\rightarrow \text{Total number of FFTs in first dimension} = s(2n_2 - 1) \\
N_{FFT2} &\rightarrow \text{Total number of FFTs in second dimension} = s(2n_1 - 1) \\
L_{FFT1} &\rightarrow \text{Length of FFTs in first dimension} = 2n_1 - 1 \\
L_{FFT2} &\rightarrow \text{Length of FFTs in second dimension} = 2n_2 - 1
\end{aligned}
$$

which means the complexity can be written as:

$$
\begin{aligned}
F_1^{MVP} &= N_{FFT1} L_{FFT1} \log(L_{FFT1}) + N_{FFT2} L_{FFT2} \log(L_{FFT1}) \\
&= s(2n_2 - 1)(2n_1 - 1) \log(2n_1 - 1) + s(2n_1 - 1)(2n_2 - 1) \log(2n_2 - 1) \\
&= s(2n_2 - 1)(2n_1 - 1)[\log(2n_1 - 1)] + \log(2n_2 - 1)] \\
&= s(2n_2 - 1)(2n_1 - 1) \log((2n_1 - 1)(2n_2 - 1)) \\
&= N_{ext} \log\left(\frac{N_{ext}}{s}\right) \\
&\approx s2^d T \log\left(2^d T\right), \text{ for } d = 2
\end{aligned} \tag{B.8}
$$

Note again, that this expression generalizes to higher-dimensional arrays $d > 2$. Next, the Hadamard product scales as:

$$
\begin{aligned}
F_2^{MVP} &= s^2(2n_2 - 1)(2n_1 - 1) \\
&= sN_{ext} \\
&\approx s^2 2^d T
\end{aligned} \tag{B.9}
$$

The IFFT of the Hadamard product has the same scaling as the FFT of the unknown vector:

$$
F_3^{MVP} = F_1^{MVP} = s2^d T \log\left(2^d T\right) \tag{B.10}
$$

The total cost $F^{MVP} = F_1^{MVP} + F_2^{MVP} + F_3^{MVP}$ for the matrix vector product for each iteration becomes:

$$
\begin{aligned}
F_{MVP} &= 2s2^d T \log\left(2^d T\right) + s^2 2^d T \\
&= s2^d T \left[2 \log\left(2^d T\right) + s\right]
\end{aligned} \tag{B.11}
$$

Note that the quadratic computational scaling in the MVP stems from the Hadamard product. Note also, that typically $2 \log\left(2^d T\right) \ll s$.

Now, if the number of iterations N_I needed to reach a given residual error is introduced, the total computational complexity F of the algorithm can be written as:

$$
\begin{aligned}
F &= F^{set} + N_I F^{MVP} \\
&= C^{set} s^2 2^d T + s^2 2^d T \log\left(2^d T\right) + N_I s 2^d T \left[2 \log\left(2^d T\right) + s\right] \\
&= C^{set} s^2 2^d T + s^2 2^d T \log\left(2^d T\right) + 2N_I s 2^d T \log\left(2^d T\right) + N_I s^2 2^d T \\
&= 2^d T \log\left(2^d T\right) \left[s^2 + 2N_I s\right] + 2^d s^2 T \left[C^{set} + N_I\right]
\end{aligned} \tag{B.12}
$$

This expression is generally not insightful for the computational complexity of the algorithm. In subsequent paragraphs two different perspectives of the algorithm will be investigated. One perspective is where a user has decided on a particular antenna array element, and wants to simulate larger and larger arrays (s constant). Another perspective is when the user has decided on the total number of array elements (T constant), but wants to investigate the accuracy of the simulation, either by increasing mesh density or by using higher-order basis functions per element.

Large Arrays If larger and larger arrays are simulated, where it is assumed that a constant amount of basis functions are on each element (s constant), the computational complexity can be written asymptotically as:

$$\underbrace{C_1}_{2^d s^2 + 2N_I s} T \log(\underbrace{2^d}_{C_2} T) \rightarrow O(T \log T) \tag{B.13}$$

in which C_1 and C_2 indicate factors which are assumed constant. We note here the computational advantage of using the FFTs, when increasing the total number of array elements.

Example For a planar $d = 2$ antenna array with $T = 10,000$ array elements we get a total cost as a function of s:

$$F = 184,082 \left[s^2 + 2N_I s\right] + 40,000 s^2 \left[C^{set} + N_I\right] \tag{B.14}$$

Many Basis Functions If a constant amount of array elements has been decided, but one wants to either discretize the elements more detailed or increase order of basis functions used, the computational complexity takes on an interesting form:

$$\underbrace{C_1}_{2^d T \log(2^d T)} \left[s^2 + 2N_I f\right] + s^2 \underbrace{C_2}_{2^d T [C^{set} + N_I]} \rightarrow O(s^2) \tag{B.15}$$

which shows that it scales quadratically with the number of basis functions per array element.

Example For a planar $d = 2$ antenna array with $s = 60$ basis functions per element we get a total cost as a function of T:

$$F = 4 \left[T \log(4T) \left[3600 + 120 N_I\right] + 3600 T \left[C^{set} + N_I\right]\right] \tag{B.16}$$

B.3 Memory Complexity

Thus far, only the computational complexity has been discussed. In the following the memory cost M of the algorithm will be examined. Memory formulas are given in

terms of number of complex-valued elements, and thus not directly in bytes since it depends on the chosen precision.
Storing the calculation of unique interactions and extended matrix blocks requires:

$$M^{set} = sN_{ext} \approx s^2 2^d T \tag{B.17}$$

Storage of the unknown vector and the resulting matrix vector product requires:

$$M^{MVP} = 2N_{ext} = s2^{d+1}T \tag{B.18}$$

The total memory requirement, disregarding the memory needed for the iterative solver becomes:

$$\begin{aligned} M &= M^{set} + M^{MVP} \\ &= sN_{ext} + 2N_{ext} \\ &= s^2 2^d T + s2^{d+1}T \rightarrow O(s^2 2^d T) \end{aligned} \tag{B.19}$$

The ratio K_M of the memory required for ordinary MoM to the asymptotic memory required in HO-ADM can be determined as:

$$K_M = \frac{s^2 T^2}{s^2 2^d T} = \frac{T}{2^d} \underbrace{\rightarrow}_{d=2} \frac{T}{4} \tag{B.20}$$

Thus, HO-ADM uses around $\frac{T}{4}$ times less memory than ordinary MoM.

Example For a state-of-the-art 30×30 planar $d = 2$ antenna array with a representative $s = 1000$ basis functions per element we get:

$$M^{\text{MoM}} = s^2 T^2 \underbrace{\rightarrow}_{\text{Complex Single Precision}} 6035 \text{ GB} \tag{B.21}$$

$$M^{\text{HO-ADM}} = 4s^2 T \underbrace{\rightarrow}_{\text{Complex Single Precision}} 26.8 \text{ GB} \tag{B.22}$$

which means that HO-ADM can handle state-of-the-art array antennas on a laptop anno 2023. Note, that (B.22) is always overestimating the required memory in HO-ADM*.

*A better approximation for the memory consumption of HO-ADM is $M = 4s^2[T - \sqrt{T}]$.

APPENDIX C

Implementation Specific Details

The purpose of the present appendix is to provide the reader with important details related to the specific implementation of HO-ADM.

C.1 Determination of Auxiliary Unknowns for Connected Arrays

In order not to introduce too many auxiliary unknowns, i.e. placing half-doublets on every external edge of the element cell of the array, an edge-mask $M \in \mathcal{B}^{N_e \times 1}$ can be used to identify (un)necessary external edges. Here N_e is the number of edges on a single array element. Assuming an already existing processed mesh associating edges and quads, the edges on which to place auxiliary unknowns can be found as outlined in Algorithm 1. We note that this is a simplified algorithm to elucidate the concept,

Algorithm 1 Finding Auxiliary Unknowns

```
1:  procedure GenerateMask
2:      M(1 : N_e) ← False
3:      for i_e = 1:N_e do          ▷ Edges on array element with neighbors all around.
4:          if Edge i_e is associated with 2 quadrilaterals then
5:              if Quads reside on 2 different array elements then
6:                  M(i_e) ← True
7:              end if
8:          end if
9:      end for
10:     return M
11: end procedure
```

as it does not take into account thinned arrays, non-identical elements and closed structures.

Looping over all edges N_e pertaining to a single array element which is completely surrounded by $3^d - 1$ neighbors, whether or not to place an additional half-doublet (auxiliary unknown) is stored at the edge index i_e in M. Remark, that we only need to place auxiliary unknowns on edges which are associated with two (or more) quads, iff these quads reside on two **different** array elements.

Because all basis functions are identically enumerated on all array elements, i_e can be interpreted as the relative index on each array element on which $M(i_e)$ determines whether a DGM half-doublet basis function should be placed. In this way, during subsequent basis function generation, the mask can be used to determine if additional half-doublets (i.e. auxiliary unknowns) should be placed on an external edge or not, simply by indexing $M(i_e)$.

C.2 Preconditioner Storage Reuse for Connected Arrays

In the HO-ADM, generation of the near-field block-diagonal coupling preconditioner $\mathcal{M}_{\mathrm{C}}$ (see Section 3.3) requires access to the interaction matrices for all array element T. Remark, however, that this information is already contained within the Toeplitz circulant tensor format (i.e. the circulant generator $\mathbf{C}(m,n,k,l)$). We provide here the mapping $\mathbf{A}(p,q) \rightarrow \mathbf{C}(m,n,k,l)$ from global MoM matrix row p and column q to circulant generator indices (m,n,k,l) in the case of an (up to two)-dimensional array (i.e. $d = \{1,2\}$)

$$
\begin{aligned}
m &= \mathrm{mod}\,(p-1, s) \\
n &= \mathrm{mod}\,(q-1, s) \\
k &= \begin{cases} P_{\mathrm{mod}} - Q_{\mathrm{mod}} + 1 & \text{for } P_{\mathrm{mod}} < Q_{\mathrm{mod}} \\ P_{\mathrm{mod}} - Q_{\mathrm{mod}} + 2n_1 & \text{for } P_{\mathrm{mod}} \geq Q_{\mathrm{mod}} \end{cases} \\
l &= \begin{cases} \frac{p}{n_1 s} - \frac{q}{n_1 s} + 1 & \text{for } \frac{p}{n_1 s} < \frac{q}{n_1 s} \\ \frac{p}{n_1 s} - \frac{q}{n_1 s} + 2n_2 & \text{for } \frac{p}{n_1 s} \geq \frac{q}{n_1 s} \end{cases},
\end{aligned}
\tag{C.1}
$$

in which $P_{\mathrm{mod}} = \mathrm{mod}\left(\frac{p-1}{s}, n_1\right)$ and $Q_{\mathrm{mod}} = \mathrm{mod}\left(\frac{q-1}{s}, n_1\right)$ and fractions denote integer division, which implies truncation. n_1 and n_2 are the number of array elements in the first and second lattice dimensions, respectively, and s is the number of basis functions per array element. Consequently, this mapping can be used to pick out the correct entries when building the unique set of at most 16 preconditioner groups (see Fig. 4 in J2).

APPENDIX D

Miscellaneous Definitions

The purpose of the present appendix is to provide the reader with definitions to various terms and phrases used throughout the dissertation:

- **Aperiodic array** consists of array elements which are non-uniformly spaced and it is used as an umbrella term for sparse and thinned arrays.

- **Circulant generator** refers to the unique matrix-blocks of the MBT MoM matrix, which are rearranged into a circulant tensor storage $\mathbf{C}(m, n, j, k, l)$, where $j \in \{1, \ldots, 2n_1 - 1\}$, $k \in \{1, \ldots, 2n_2 - 1\}$ and $l \in \{1, \ldots, 2n_3 - 1\}$ enumerate the rearranged blocks at the first ($i = 1$), second ($i = 2$) and third ($i = 3$) block-circulant level, respectively. m and n denote the rows and columns, respectively, at the innermost-level.

- **Computation time** is the wall clock time, including basis function generation, setup-phase of the algorithm as well as the iterative solution process.

- **Computational (or memory) complexity** refers to the asymptotic complexity usually described by *Big-O* notation $\mathcal{O}(f(x))$ which denotes that the true scaling $g(x)$ of an algorithm as $x \to \infty$ satisfies $|g(x)| \leq C|f(x)|$ for a fixed positive $C \in \mathbb{R}$ for all $x > x_0,\ x_0 \in \mathbb{R}$ [20].

- **Discretization (or mesh)** is in this dissertation used to denote spatial discretization, that is, dividing a given virtual representation of a physical structure into a discrete set of cells or elements.

- **Discretization density** refers to the total number of unknowns normalized by the total surface area (in square wavelengths) of the employed mesh.

- **Edge** refers to one of the three (four) boundaries of a given triangular (quadrilateral) mesh cell.

- **Error-controllable** refers to a computational method for which the user can specify *a priori* to a simulation run, the number of significant digits which is desired in the solution vector.
- **Full MoM** refers to the generation and direct solution of the full Method of Moments matrix. In this dissertation it is implicitly understood as the MoM with higher-order basis functions.
- **Fully-populated** refers to a regular, and not necesarily orthogonal, lattice on which array elements are placed at all available positions.
- **Interaction** is in this dissertation used to denote the result of calculating the *Moments* (inner products between basis functions and the Green function) in the MoM-matrix, corresponding to the interaction between two (or more) elements.
- **Laptop** refers to the physical battery powered mobile computer used to produce the results of this dissertation, with specifications given in Appendix E.
- **Memory consumption** refers to the amount of Random Access Memory (RAM) used by all parts of the algorithm, including storing matrices, solution vectors, preconditioners and the Krylov subspace.
- **Mesh cells** refer to the curved quadrilaterals used in this dissertation to discretize a given geometry [87].
- **Regular array** refers to an arrangement of array elements which are placed equidistant along each lattice dimension. Consequently, non-orthogonal and circular lattices are classified as regular arrays.
- **Server** refers to the physical high-performance compute server used to produce the results of this dissertation, with specifications given in Appendix E.
- **Simulation** refers to process of running a specific algorithm with a virtual representation of a given electromagnetic structure, with the aim to replicate the outcomes that would occur in a real-world physical environment.
- **Sparse array** is an array which contains substantially fewer driven radiating elements than a conventional uniformly spaced array with the same beamwidth having identical elements.
- **Thinned array** is a sparse array antenna obtained by terminating or removing a substantial number of elements from a conventional uniformly spaced array.

APPENDIX E

Computational Machines

The purpose of the present appendix is to list the computer architectures which have been used to produce the results of the contemporary dissertation.

Laptop

The laptop used is a Dell Precision 5540 with an Intel® Core™ i7-9850H Processor with 6 physical cores. Each physical core can run 2 threads using Intel's hyperthreading technology.

Processor	Intel® Core™ i7-9850H CPU @ 2.60 GHz
Memory	32 GB 2667 MHz DDR3

Table E.1: Specifications for the laptop used to produce the results of this dissertation.

Server

The computing server is used for large cases for which the laptop resources are insufficient or to compute very accurate reference results with full MoM. It comprises two Intel® Xeon™ E5-2690 with 12 physical cores, for a total of 24 cores and 48 threads in the machine.

Processor	Intel® Xeon™ E5-2690 CPU @ 3.50 GHz
Memory	1536 GB 1600 MHz DDR3

Table E.2: Specifications for computing server used to produce the results of this dissertation.

This page is intentionally not used for content

Bibliography

[1] S. Rao, L. Shafai, and S. K. Sharma, *Handbook of Reflector Antennas and Feed Systems Volume III: Applications of Reflectors*. Artech House, 2013.

[2] H. Fenech, S. Amos, and T. Waterfield, "The role of array antennas in commercial telecommunication satellites," in *2016 10th European Conference on Antennas and Propagation (EuCAP)*, Davos, Switzerland, 2016.

[3] S. Gao, N. F. Chamberlain, and Y. J. Guo, "Guest Editorial: Antennas for satellite communications," *IEEE Transactions on Antennas and Propagation*, vol. 63, no. 4, pp. 1186–1190, 2015.

[4] H. Fenech, L. Roux, A. Hirsch, and V. Soumpholphakdy, "Satellite antennas and digital payloads for future communication satellites: The quest for efficiencies and greater flexibility," *IEEE Antennas and Propagation Magazine*, vol. 61, no. 5, pp. 20–28, 2019.

[5] S. Panthi, D. Breynaert, C. McLain, and J. King, "Beam hopping - a flexible satellite communication system for mobility," in *35th AIAA International Communications Satellite Systems Conference*, Trieste, Italy, 2017, p. 5413.

[6] RSINC, "How many beams does ViaSat-3 have?" https://www.rsinc.com/how-many-beams-does-viasat-3-have.php, 2023, accessed: 2023-11-24.

[7] A. L. Pérez-Neira, M. A. Vazquez, B. Shankar, S. Maleki, and S. Chatzinotas, "Signal processing for high throughput satellite systems: Challenges for new interference limited scenarios," *Signal Processing*, 2019.

[8] G. Thomas, S. Laws, J. Kershaw, S. Amos, P. Jung, A. Montesano, N. Gatti, A. Le Pera, and I. Roberts, "Eutelsat Quantum a fully flexible software defined satellite successfully operating on orbit," in *39th International Communications Satellite Systems Conference*. IET, 2023, pp. 46–57.

[9] R. Correia, T. Varum, J. N. Matos, A. Oliveira, and N. B. Carvalho, "User terminal segments for low-earth orbit satellite constellations: Commercial systems and innovative research ideas," *IEEE Microwave Magazine*, vol. 23, no. 10, pp. 47–58, 2022.

[10] V. Pascale, D. Maiarelli, L. D'Agristina, and N. Gatti, "Design and qualification of Ku-band-radiating chains for receive active array antennas of flexible telecommunication satellites," *International Journal of Microwave and Wireless Technologies*, vol. 12, no. 6, pp. 487–503, 2020.

[11] R. J. Mailloux, *Phased array antenna handbook*. Artech House, 2017.

[12] H. Singh, H. Sneha, R. Jha *et al.*, "Mutual coupling in phased arrays: A review," *International Journal of Antennas and Propagation*, vol. 2013, pp. 1687–5869, 2013.

[13] G. Toso, C. Mangenot, and A. Roederer, "Sparse and thinned arrays for multiple beam satellite applications," in *The Second European Conference on Antennas and Propagation, EuCAP 2007*, Edinburgh, Scotland, 2007.

[14] O. Bucci, T. Isernia, A. Morabito, S. Perna, and D. Pinchera, "Aperiodic arrays for space applications: An effective strategy for the overall design," in *2009 3rd European Conference on Antennas and Propagation*. IEEE, 2009, pp. 2031–2035.

[15] A. Roederer, E. Farr, L. Foged, M. Francis, R. Hansen, R. Haupt, and K. Warnick, "IEEE standard for definitions of terms for antennas," *IEEE Std*, pp. 145–2013, 2014.

[16] TICRA, "TICRA Tools ESTEAM," https://www.ticra.com/software/esteam/, 2019.

[17] E. Jørgensen, "Higher-order integral equation methods in computational electromagnetics," Ph.D. dissertation, Technical University of Denmark, 2003.

[18] N. Morita, N. Kumagai, and J. R. Mautz, *Integral equation methods for electromagnetics*. Artech House, 1990.

[19] R. F. Harrington and J. L. Harrington, *Field computation by moment methods*. Oxford University Press, Inc., 1996.

[20] L. Elden, L. Wittmeyer-Koch, and H. B. Nielsen, *Introduction to Numerical Computation - analysis and MATLAB illustrations*. Studentlitteratur, 2004.

[21] D. F. Kelley, "Embedded element patterns and mutual impedance matrices in the terminated phased array environment," *IEEE Antennas and Propagation Society, AP-S International Symposium (digest)*, vol. 3, pp. 1 552 340, 659–662, 2005.

[22] K. F. Warnick, R. Maaskant, M. V. Ivashina, D. B. Davidson, and B. D. Jeffs, *Phased arrays for radio astronomy, remote sensing, and satellite communications*. Cambridge University Press, 2018.

[23] R. Chiniard, A. Barka, and O. Pascal, "Floquet modes expansion coupled to multidomain technique devoted to large phased array modelling," *35th European Microwave Conference 2005 - Conference Proceedings*, vol. 1, p. 1608860, 2005.

[24] A. S. Conradie, M. Chose, P. I. Cilliers, and M. M. Botha, "Antenna array analysis by iterative DGFM-based local solutions," *IEEE Transactions on Antennas and Propagation*, vol. 71, no. 6, pp. 5199–5211, 2023.

[25] S.-C. Lee, M. N. Vouvakis, and J.-F. Lee, "A non-overlapping domain decomposition method with non-matching grids for modeling large finite antenna arrays," *Journal of Computational Physics*, vol. 203, no. 1, pp. 1–21, 2005.

[26] Z. Peng, X.-C. Wang, and J.-F. Lee, "Integral equation based domain decomposition method for solving electromagnetic wave scattering from non-penetrable objects," *IEEE Transactions on Antennas and Propagation*, vol. 59, no. 9, pp. 3328–3338, 2011.

[27] A. Deraemaeker, I. Babuška, and P. Bouillard, "Dispersion and pollution of the fem solution for the helmholtz equation in one, two and three dimensions," *International journal for numerical methods in engineering*, vol. 46, no. 4, pp. 471–499, 1999.

[28] J. R. Mosig and F. E. Gardiol, "General integral equation formulation for microstrip antennas and scatterers," *IEEE Proceedings H (Microwaves, Antennas and Propagation)*, vol. 132, no. 7, pp. 424–432, 1985.

[29] M. I. Aksun and R. Mittra, "Derivation of closed-form Green's functions for a general microstrip geometry," *IEEE Transactions on Microwave Theory and Techniques*, vol. 40, no. 11, pp. 2055–62, 1992.

[30] M. I. Aksun, "A robust approach for the derivation of closed-form Green's functions," *IEEE Transactions on Microwave Theory and Techniques*, vol. 44, no. 5, pp. 651–658, 1996.

[31] H. Bui-Van, J. Abraham, M. Arts, Q. Gueuning, C. Raucy, D. González-Ovejero, E. de Lera Acedo, and C. Craeye, "Fast and accurate simulation technique for large irregular arrays," *IEEE Transactions on Antennas and Propagation*, vol. 66, no. 4, pp. 1805–1817, 2018.

[32] D. Gonzalez-Ovejero and C. Craeye, "Interpolatory macro basis functions analysis of non-periodic arrays," *IEEE Transactions on Antennas and Propagation*, vol. 59, no. 8, pp. 3117–3122, 2011.

[33] C. Craeye, J. Laviada, R. Maaskant, and R. Mittra, "Macro basis function framework for solving Maxwell's equations in surface integral equation form," *The FERMAT Journal*, vol. 3, pp. 1–16, 2014.

[34] V. Prakash, , and R. Mittra, "Characteristic basis function method: A new technique for efficient solution of method of moments matrix equations," *Microwave and Optical Technology Letters*, vol. 36, no. 2, pp. 95–100, 2003.

[35] E. Lucente, A. Monorchio, and R. Mittra, "An iteration-free MoM approach based on excitation independent characteristic basis functions for solving large multiscale electromagnetic scattering problems," *IEEE Transactions on Antennas and Propagation*, vol. 56, no. 4, pp. 999–1007, 2008.

[36] L. Matekovits, V. A. Laza, and G. Vecchi, "Analysis of large complex structures with the synthetic-functions approach," *IEEE Transactions on Antennas and Propagation*, vol. 55, no. 9, pp. 2509–2521, 2007.

[37] W. Xiang, W. Yang, and W. Lu, "Fast sub-entire-domain basis functions method for analysis of composite finite periodic structures with dielectric-conductor cells," *IEEE Antennas and Wireless Propagation Letters*, 2022.

[38] L. Matekovits, G. Vecchi, M. Bercigli, and M. Bandinelli, "Synthetic-functions analysis of large aperture-coupled antennas," *IEEE Transactions on Antennas and Propagation*, vol. 57, no. 7, pp. 1936–1943, 2009.

[39] R. Maaskant, R. Mittra, and A. Tijhuis, "Fast analysis of large antenna arrays using the characteristic basis function method and the adaptive cross approximation algorithm," *IEEE Transactions on Antennas and Propagation*, vol. 56, no. 11, pp. 3440–3451, 2008.

[40] D. Gonzalez-Ovejero, F. Mesa, and C. Craeye, "Accelerated macro basis functions analysis of finite printed antenna arrays through 2D and 3D multipole expansions," *IEEE Transactions on Antennas and Propagation*, vol. 61, no. 2, pp. 707–717, 2012.

[41] S. Kapur and D. E. Long, "IES3: a fast integral equation solver for efficient 3-dimensional extraction." in *IEEE/ACM International Conference on Computer-aided Design*, vol. 97, 1997, pp. 448–455.

[42] S. M. Seo and J.-F. Lee, "A single-level low rank IE-QR algorithm for PEC scattering problems using EFIE formulation," *IEEE Transactions on Antennas and Propagation*, vol. 52, no. 8, pp. 2141–2146, 2004.

[43] S. Kurz, O. Rain, and S. Rjasanow, "The adaptive cross-approximation technique for the 3D boundary-element method," *IEEE Transactions on Magnetics*, vol. 38, no. 2, pp. 421–424, 2002.

[44] S. M. Seo and J.-F. Lee, "A fast IE-FFT algorithm for solving PEC scattering problems," *IEEE Transactions on Magnetics*, vol. 41, no. 5, pp. 1476–1479, 2005.

[45] Q. Gueuning, E. D. L. Acedo, A. K. Brown, and C. Craeye, "An inhomogeneous plane-wave based single-level fast direct solver for the scattering analysis of extremely large antenna arrays," *IEEE Transactions on Antennas and Propagation*, 2022.

[46] W. Yu, H. Yang, S. Li, and Y. Xu, "An HSS-matrix-based fast direct solver with randomized algorithm," *The Applied Computational Electromagnetics Society Journal*, pp. 814–817, 2018.

[47] J.-G. Wei, Z. Peng, and J.-F. Lee, "A fast direct matrix solver for surface integral equation methods for electromagnetic wave scattering from non-penetrable targets," *Radio science*, vol. 47, no. 5, pp. 1–9, 2012.

[48] M. Ma and D. Jiao, "Accuracy directly controlled fast direct solution of general H2-matrices and its application to solving electrodynamic volume integral equations," *IEEE Transactions on Microwave Theory and Techniques*, vol. 66, no. 1, pp. 35–48, 2017.

[49] R. Coifman, V. Rokhlin, and S. Wandzura, "The fast multipole method for the wave equation: a pedestrian prescription," *IEEE Antennas and Propagation Magazine*, vol. 35, no. 3, pp. 7–12, 1993.

[50] C. Lu and W. Chew, "A multilevel algorithm for solving a boundary integral-equation of wave scattering," *Microwave and Optical Technology Letters*, vol. 7, no. 10, pp. 466–470, 1994.

[51] J. Song, C.-C. Lu, and W. C. Chew, "Multilevel fast multipole algorithm for electromagnetic scattering by large complex objects," *IEEE Transactions on Antennas and Propagation*, vol. 45, no. 10, pp. 1488–1493, 1997.

[52] X. Zhao, Z. Lin, Y. Zhang, S.-W. Ting, and T. K. Sarkar, "Parallel hybrid method of HOMoM–MLFMA for analysis of large antenna arrays on an electrically large platform," *IEEE Transactions on Antennas and Propagation*, vol. 64, no. 12, pp. 5501–5506, 2016.

[53] B. Karaosmanoğlu and Ö. Ergül, "Acceleration of MLFMA simulations using trimmed tree structures," *IEEE Transactions on Antennas and Propagation*, vol. 69, no. 1, pp. 356–365, 2020.

[54] W. B. Lu, T. J. Cui, and H. Zhao, "Acceleration of fast multipole method for large-scale periodic structures with finite sizes using sub-entire-domain basis functions," *IEEE Transactions on Antennas and Propagation*, vol. 55, no. 2, pp. 414–421, 2007.

[55] R. W. Kindt and J. L. Volakis, "Array decomposition-fast multipole method for finite array analysis," *Radio Science*, vol. 39, no. 2, pp. 1–9, 2004.

[56] E. H. Bleszynski, M. K. Bleszynski, and T. Jaroszewicz, "Block-Toeplitz fast integral equation solver for large finite periodic and partially periodic array systems," *IEICE Transactions on Electronics*, vol. 87, no. 9, pp. 1586–1594, 2004.

[57] J. R. Phillips and J. K. White, "A precorrected-FFT method for electrostatic analysis of complicated 3-D structures," *IEEE Transactions on Computer-Aided Design of Integrated Circuits and Systems*, vol. 16, no. 10, pp. 1059–1072, 1997.

[58] J. White, J. Phillips, and T. Korsmeyer, "Comparing precorrected-FFT and fast multipole algorithms for solving three-dimensional potential integral equations,"," in *Proceedings of the Colorado Conference on Iterative Methods*. Citeseer, 1994, pp. 4–10.

[59] J. Phillips, "Error and complexity analysis for a collocation-grid-projection plus precorrected-FFT algorithm for solving potential integral equations with Laplace or Helmholtz kernels," in *NASA Conference Publication*. Citeseer, 1996, pp. 673–688.

[60] E. Bleszynski, M. Bleszynski, and T. Jaroszewicz, "AIM: Adaptive integral method for solving large-scale electromagnetic scattering and radiation problems," *Radio Science*, vol. 31, no. 5, pp. 1225–1251, 1996.

[61] S. Sharma and P. Triverio, "AIMx: an extended adaptive integral method for the fast electromagnetic modeling of complex structures," *IEEE Transactions on Antennas and Propagation*, vol. 69, no. 12, pp. 8603–8617, 2021.

[62] E. Bleszynski, M. Bleszynski, and T. Jaroszewicz, "Fast integral-equation solver for electromagnetic scattering problems," *IEEE Antennas and Propagation Society, AP-S International Symposium (digest)*, vol. 1, pp. 416–419, 1994.

[63] O. S. Kim and P. Meincke, "Adaptive integral method for higher order method of moments," *IEEE Transactions on Antennas and Propagation*, vol. 56, no. 8, pp. 2298–2305, 2008.

[64] F. Ling, C. F. Wang, and J. M. Jin, "Application of adaptive integral method to scattering and radiation analysis of arbitrarily shaped planar structures," *IEEE Antennas and Propagation Society International Symposium, 1998 Digest - Antennas: Gateways To the Global Network - Held in Conjunction With: USNC/URSI National Radio Science Meeting*, vol. 3, p. 690966, 1998.

[65] F. Ling, C. Wang, and J. Jin, "An efficient algorithm for analyzing large-scale microstrip structures using adaptive integral method combined with discrete complex-image method," *IEEE Transactions on Microwave Theory and Techniques*, vol. 48, no. 5, pp. 832–839, 2000.

[66] P. De Vita, F. De Vita, A. Di Maria, and A. Freni, "An efficient technique for the analysis of large multilayered printed arrays," *IEEE Antennas and Wireless Propagation Letters*, vol. 8, pp. 4 738 410, 104–107, 2009.

[67] S. S. Bindiganavale, J. L. Volakis, and H. Anastassiu, "Scattering from planar structures containing small features using the Adaptive Integral Method (AIM)," *IEEE Transactions on Antennas and Propagation*, vol. 46, no. 12, pp. 1867–1878, 1998.

[68] C. F. Wang, F. Ling, J. Song, and J. M. Jin, "Adaptive integral solution of combined field integral equation," *Microwave and Optical Technology Letters*, vol. 19, no. 5, pp. 321–328, 1998.

[69] R. W. Kindt, K. Sertel, E. Topsakal, and J. L. Volakis, "Array decomposition method for the accurate analysis of finite arrays," *IEEE Transactions on Antennas and Propagation*, vol. 51, no. 6, pp. 1364–1372, 2003.

[70] B. E. Barrowes, F. L. Teixeira, and J. A. Kong, "Fast algorithm for matrix–vector multiply of asymmetric multilevel block-Toeplitz matrices in 3-D scattering," *Microwave and Optical Technology Letters*, vol. 31, no. 1, pp. 28–32, 2001.

[71] J. J. Goodman, B. T. Draine, and P. J. Flatau, "Application of fast-Fourier-transform techniques to the discrete-dipole approximation," *Optics Letters*, vol. 16, no. 15, pp. 1198–1200, 1991.

[72] V. Akan, E. Yazgan, and A. Sabban, "Antennas for space applications: A review," *Advanced Radio Frequency Antennas for Modern Communication and Medical Systems*, pp. 139–171, 2020.

[73] S. Huber, M. Younis, G. Krieger, and A. Moreira, "Error analysis for digital beamforming synthetic aperture radars: A comparison of phased array and array-fed reflector systems," *IEEE Transactions on Geoscience and Remote Sensing*, vol. 59, no. 8, pp. 6314–6322, 2020.

[74] J. Johansson and P. Ingvarson, "Array antenna activities at RUAG space: An overview," in *2013 7th European Conference on Antennas and Propagation (EuCAP)*, 2013, pp. 666–669.

[75] S. Richard, Y. Patenaude, P. Markland, J. Dallaire, F. Ménard, and V. Dupessey, "The Inmarsat 4 antenna feed array," in *2002 9th International Symposium on Antenna Technology and Applied Electromagnetics*. IEEE, 2002.

[76] L. Yu, J. Wan, K. Zhang, F. Teng, L. Lei, and Y. Liu, "Spaceborne multibeam phased array antennas for satellite communications," *IEEE Aerospace and Electronic Systems Magazine*, vol. 38, no. 3, pp. 28–47, 2022.

[77] N. Chahat, B. Cook, H. Lim, and P. Estabrook, "All-metal dual-frequency RHCP high-gain antenna for a potential europa lander," *IEEE Transactions on Antennas and Propagation*, vol. 66, no. 12, pp. 6791–6798, 2018.

[78] D. Jang, T. H. Lim, S. Park, and H. Choo, "Broadband all-metal vivaldi array antenna with pyramidal-shaped wings for leo satellite applications," *Journal of Electromagnetic Engineering and Science*, vol. 23, no. 5, pp. 405–411, 2023.

[79] W.-L. Zhou, S.-W. Qu, and M. Xia, "Full-metal dual-polarized phased array antenna with large element spacing," *IEEE Antennas and Wireless Propagation Letters*, pp. 1–5, 2023.

[80] P. Aero, "Hanwha Phasor, OneWeb formalize ESA terminal development efforts," 2023, accessed on: 2023-10-18, https://paxex.aero/hanwha-phasor-terminal-oneweb-development-agreement/.

[81] Eutelsat, "Eutelsat quantum," 2021, accessed: 2023-08-27, https://www.eutelsat.com/en/satellites/eutelsat-48-east.html.

[82] D. C. Russell, "Toeplitz forms and their applications," *Proceedings of the Edinburgh Mathematical Society*, vol. 11, no. 3, pp. 186–187, 1959.

[83] O. Toeplitz, "Zur Theorie der quadratischen und bilinearen Formen von unendlich vielen Veränderlichen: I. Teil: Theorie der L-Formen," *Mathematische Annalen*, vol. 70, pp. 351–376, 1911.

[84] G. H. Golub and C. F. Van Loan, *Matrix computations*. JHU Press, 1996.

[85] D. R. Wilton, P. W. Fink, R. D. Graglia *et al.*, "Higher order modeling in hybrid approaches to the computation of electromagnetic fields," in *European Congress in Computational Methods in Applied Science and Engineering*, 2000.

[86] D. Sun, J. Manges, X. Yuan, and Z. Cendes, "Spurious modes in finite-element methods," *IEEE Antennas and Propagation Magazine*, vol. 37, no. 5, pp. 12–24, 1995.

[87] R. D. Graglia, D. R. Wilton, and A. F. Peterson, "Higher order interpolatory vector bases for computational electromagnetics," *IEEE Transactions on Antennas and Propagation*, vol. 45, no. 3, pp. 329–342, 1997.

[88] E. Jorgensen, J. L. Volakis, P. Meincke, and O. Breinbjerg, "Higher order hierarchical legendre basis functions for electromagnetic modeling," *IEEE Transactions on Antennas and Propagation*, vol. 52, no. 11, pp. 2985–2995, 2004.

[89] S. Rao, D. Wilton, and A. Glisson, "Electromagnetic scattering by surfaces of arbitrary shape," *IEEE Transactions on antennas and propagation*, vol. 30, no. 3, pp. 409–418, 1982.

[90] J.-C. Nédélec, "Mixed finite elements in R3," *Numerische Mathematik*, vol. 35, no. 3, pp. 315–341, 1980.

[91] O. Borries, P. Meincke, E. Jørgensen, and P. C. Hansen, "Multilevel fast multipole method for higher order discretizations," *IEEE Transactions on Antennas and Propagation*, vol. 62, no. 9, pp. 4695–4705, 2014.

[92] A. F. Peterson, S. L. Ray, and R. Mittra, *Computational methods for electromagnetics*. Wiley-IEEE Press, 1997.

[93] "IEEE standard for definitions of terms for antennas," *IEEE Std 145-2013 (Revision of IEEE Std 145-1993)*, pp. 1–50, 2014.

[94] T. D. Vani and K. R. Subhashini, "Optimal synthesis of thinned arrays utilizing fast Fourier transform technique," *Progress In Electromagnetics Research M*, vol. 72, pp. 175–186, 2018.

[95] C.-B. Moon, J.-W. Jeong, K.-H. Nam, Z. Xu, and J.-S. Park, "Design and analysis of a thinned phased array antenna for 5g wireless applications," *International Journal of Antennas and Propagation*, vol. 2021, pp. 1–8, 2021.

[96] W. P. Keizer, "Synthesis of thinned planar circular and square arrays using density tapering," *IEEE Transactions on Antennas and Propagation*, vol. 62, no. 4, pp. 1555–1563, 2013.

[97] P.-F. Li, S.-W. Qu, S. Yang, and J. Hu, "Low-scattering-cross section thinned phased array antenna based on active cancellation technique," *IEEE Transactions on Antennas and Propagation*, vol. 70, no. 7, pp. 5481–5490, 2022.

[98] P. Rocca, G. Oliveri, R. J. Mailloux, and A. Massa, "Unconventional phased array architectures and design methodologies—a review," *Proceedings of the IEEE*, vol. 104, no. 3, pp. 544–560, 2016.

[99] A. Á. Salas-Sánchez, C. López-Álvarez, J. A. Rodríguez-González, M. E. López-Martín, and F. J. Ares-Pena, "An improved pattern synthesis iterative method in planar arrays for obtaining efficient footprints with arbitrary boundaries," *Sensors*, vol. 21, no. 7, p. 2358, 2021.

[100] P. Rocca, N. Anselmi, A. Polo, and A. Massa, "Modular design of hexagonal phased arrays through diamond tiles," *IEEE Transactions on Antennas and Propagation*, vol. 68, no. 5, pp. 3598–3612, 2020.

[101] A. Farina, P. Holbourn, T. Kinghorn, and L. Timmoneri, "AESA radar—pan-domain multi-function capabilities for future systems," in *2013 IEEE International Symposium on Phased Array Systems and Technology*, 2013, pp. 4–11.

[102] N. Razavi-Ghods, E. de Lera Acedo, A. El-Makadema, P. Alexander, and A. Brown, "Analysis of sky contributions to system temperature for low frequency ska aperture array geometries," *Experimental Astronomy*, vol. 33, pp. 141–155, 2012.

[103] Z. Peng, K.-H. Lim, and J.-F. Lee, "A discontinuous Galerkin surface integral equation method for electromagnetic wave scattering from nonpenetrable targets," *IEEE Transactions on Antennas and Propagation*, vol. 61, no. 7, pp. 3617–3628, 2013.

[104] Z. Peng, R. Hiptmair, Y. Shao, and B. MacKie-Mason, "Domain decomposition preconditioning for surface integral equations in solving challenging electromagnetic scattering problems," *IEEE Transactions on Antennas and Propagation*, vol. 64, no. 1, pp. 210–223, 2015.

[105] X.-W. Huang, M.-L. Yang, and X.-Q. Sheng, "A simplified discontinuous Galerkin self-dual integral equation formulation for electromagnetic scattering from extremely large IBC objects," *IEEE Transactions on Antennas and Propagation*, vol. 70, no. 5, pp. 3575–3586, 2021.

[106] V. F. Martin, D. M. Solis, M. G. Araujo, L. Landesa, F. Obelleiro, and J. M. Taboada, "A discontinuous Galerkin integral equation approach for electromagnetic modeling of realistic and complex radiating systems," *IEEE Transactions on Antennas and Propagation*, vol. 71, no. 5, pp. 4606–4611, 2023.

[107] B.-B. Kong and X.-Q. Sheng, "A discontinuous Galerkin surface integral equation method for scattering from multiscale homogeneous objects," *IEEE Transactions on Antennas and Propagation*, vol. 66, no. 4, pp. 1937–1946, 2018.

[108] V. F. Martín, L. Landesa, F. Obelleiro, and J. M. Taboada, "A discontinuous Galerkin combined field integral equation formulation for electromagnetic modeling of piecewise homogeneous objects of arbitrary shape," *IEEE Transactions on Antennas and Propagation*, vol. 70, no. 1, pp. 487–498, 2021.

[109] C. T. Kelley, *Iterative methods for linear and nonlinear equations*. SIAM, 1995.

[110] Y. Saad and M. H. Schultz, "GMRES: A generalized minimal residual algorithm for solving nonsymmetric linear systems," *SIAM Journal on scientific and statistical computing*, vol. 7, no. 3, pp. 856–869, 1986.

[111] O. P. Borries, "Algorithms for electromagnetic scattering analysis of electrically large structures," Ph.D. dissertation, Technical University of Denmark, 2015.

[112] H. A. Van der Vorst, "Bi-CGSTAB: A fast and smoothly converging variant of bi-cg for the solution of nonsymmetric linear systems," *SIAM Journal on Scientific and Statistical Computing*, vol. 13, no. 2, pp. 631–644, 1992.

[113] P. Sonneveld and M. B. Van Gijzen, "IDR(s): A family of simple and fast algorithms for solving large nonsymmetric systems of linear equations," *SIAM Journal on Scientific Computing*, vol. 31, no. 2, pp. 1035–1062, 2009.

[114] J. Zhang and H. Dai, "A new iterative method for solving complex symmetric linear systems," *Applied Mathematics and Computation*, vol. 302, pp. 9–20, 2017.

[115] Y. Saad, *Iterative methods for sparse linear systems*. SIAM, 2003.

[116] K. T. Pham, A. Clemente, E. Fourn, F. Diaby, L. Dussopt, and R. Sauleau, "Low-cost metal-only transmitarray antennas at Ka-band," *IEEE Antennas and Wireless Propagation Letters*, vol. 18, no. 6, pp. 1243–1247, 2019.

[117] S. H. R. Tuloti, Z. Mousavirazi, A. Kesavan, and T. A. Denidni, "A low profile dual-polarized transmitarray antenna at Ka-band," *AEU-International Journal of Electronics and Communications*, vol. 143, p. 154016, 2022.

[118] S. Varghese, T. Nguyen, M. Babu, and N. Kunju, "Generation of orbital angular momentum (OAM) by metasurface lens antenna at 140 GHz for 6G applications," in *2023 XXXVth General Assembly and Scientific Symposium of the International Union of Radio Science (URSI GASS)*. IEEE, 2023.

[119] B. Rahmati and H. Hassani, "High-efficient wideband slot transmitarray antenna," *IEEE Transactions on Antennas and Propagation*, vol. 63, no. 11, pp. 5149–5155, 2015.

[120] H. Yu, Z. Zhang, J. Su, M. Qu, Z. Li, S. Xu, and F. Yang, "Quad-polarization reconfigurable reflectarray with independent beam scanning and polarization switching capabilities," *IEEE Transactions on Antennas and Propagation*, 2023.

[121] H. Luyen, J. H. Booske, and N. Behdad, "2-bit phase quantization using mixed polarization-rotation/non-polarization-rotation reflection modes for beam-steerable reflectarrays," *IEEE Transactions on Antennas and Propagation*, vol. 68, no. 12, pp. 7937–7946, 2020.

[122] X. Kong, Q. Wang, S. Jiang, L. Kong, J. Yuan, X. Yan, X. Wang, and X. Zhao, "A metasurface composed of 3-bit coding linear polarization conversion elements and its application to rcs reduction of patch antenna," *Scientific Reports*, vol. 10, no. 1, p. 17843, 2020.

[123] C. P. Gallagher, J. K. Hamilton, I. R. Hooper, J. R. Sambles, A. P. Hibbins, C. R. Lawrence, and J. Bows, "Multi-resonant tessellated anchor-based metasurfaces," *Scientific Reports*, vol. 13, no. 1, p. 3641, 2023.

[124] E. Mutluer, B. Döken, and M. Kartal, "A dual-band frequency selective surface design for satellite applications," in *2018 18th Mediterranean Microwave Symposium (MMS)*, 2018, pp. 43–46.

[125] B. Singh, N. Sarwade, and K. P. Ray, "Non-identical rectangular microstrip antenna arrays for amplitude tapering," *IETE Journal of Research*, vol. 64, no. 3, pp. 366–374, 2018.

[126] ——, "Compact planar antenna array with tapering in both planes for desired first sidelobe reduction," *IEEE Antennas and Wireless Propagation Letters*, vol. 18, no. 3, pp. 531–535, 2019.

[127] M. A. El-Hassan, K. Hussein, and K. Awadalla, "Circularly polarized planar antenna array using linear polarized microstrip antenna with beamforming for sar applications," in *Journal of Physics: Conference Series*, vol. 1447, no. 1. IOP Publishing, 2020, p. 012008.

[128] J. Liu and J.-L. Li, "A low-cost, wideband, dual-circularly polarized traveling wave antenna array," *International Journal of RF and Microwave Computer-Aided Engineering*, vol. 31, no. 3, p. e22532, 2021.

[129] T. Teshirogi, M. Tanaka, and W. Chujo, "Wideband circularly polarized array antenna with sequential rotations and phase shift of elements," *Microstrip antennas: the analysis and design of microstrip antennas and arrays*, p. 136, 1995.

[130] P. Hall, J. Dahele, and J. James, "Design principles of sequentially fed, wide bandwidth, circularly polarised microstrip antennas," in *IEE Proceedings H (Microwaves, Antennas and Propagation)*, vol. 136, no. 5. IET, 1989, pp. 381–389.

[131] F. P. Andriulli, K. Cools, I. Bogaert, and E. Michielssen, "On a well-conditioned electric field integral operator for multiply connected geometries," *IEEE Transactions on Antennas and Propagation*, vol. 61, no. 4, pp. 2077–2087, 2012.

[132] G. Pisharody and D. Weile, "Electromagnetic scattering from a homogeneous material body using time domain integral equations and bandlimited extrapolation," in *IEEE Antennas and Propagation Society International Symposium. Digest. Held in conjunction with: USNC/CNC/URSI North American Radio Sci. Meeting (Cat. No. 03CH37450)*, vol. 3. IEEE, 2003, pp. 567–570.

[133] T.-K. Wu and L. L. Tsai, "Scattering from arbitrarily-shaped lossy dielectric bodies of revolution," *Radio Science*, vol. 12, no. 5, pp. 709–718, 1977.

[134] B. M. Kolundzija, "Electromagnetic modeling of composite metallic and dielectric structures," *IEEE Transactions on Microwave Theory and Techniques*, vol. 47, no. 7, pp. 1021–1032, 1999.

[135] J. G. Proakis, *Digital signal processing: principles, algorithms, and applications, 4/E*. Pearson Education India, 2007.

[136] G. Wetzstein, D. R. Lanman, M. W. Hirsch, and R. Raskar, "Tensor displays: compressive light field synthesis using multilayer displays with directional backlighting," *ACM Transactions on Graphics*, vol. 31, no. 4, pp. 1–11, 2012.

{2.7182818284}ϑφερτυθιοπσδφγηξκλ